Title	High-Pressure Synthesis, Crystal Structures and Physical Properties of Perovskite-Related 5d Transition Metal Oxides
Author(s)	KANG, Xun
Degree Grantor	北海道大学
Degree Name	博士(理学)
Dissertation Number	甲第15680号
Issue Date	2023-12-25
DOI	https://doi.org/10.14943/doctoral.k15680
Doc URL	https://hdl.handle.net/2115/91206
Type	doctoral thesis
File Information	KANG_XUN.pdf

High-Pressure Synthesis, Crystal Structures and Physical Properties of Perovskite-Related 5d transition metal Oxides

A Thesis

Submitted by

Xun KANG

In fulfillment for the award of the degree of

Doctor of Science

Graduate School of Chemical Sciences and Engineering,

Hokkaido University

2023

Abstract

Perovskite-related materials have gained significant popularity in recent years due to their unconventional and outstanding physical and chemical properties, including ferroelectricity, multiferroicity, magnetoresistance, and exchange bias effects. Notably, materials related to perovskites that incorporate 5d elements have emerged as a leading and potentially applicable research area in inorganic and solid-state chemistry. This is attributed to the competition between local and itinerant d electrons, which can yield a range of beneficial characteristics, including frustrated magnetism, metal-insulator transitions, high-T_c superconductivity, and more. In this study, I successfully synthesized several 5d perovskite-related compounds using the high-pressure high-temperature method and subsequently investigated their crystal structures, as well as their magnetic and electrical transport properties.

Chapter 1 provides an overview of the research background, encompassing the fundamental crystal structure, mechanisms related to magnetism, material conductivity models referenced in this work, and the historical significance of high-pressure technology in materials science.

Chapter 2 predominantly outlines the experimental details and characteristic techniques employed in this study.

Chapter 3 presents the investigation of two double perovskite oxides, Cd_2FeOsO_6 and Cd_2FeReO_6, obtained under high-temperature and high-pressure conditions, with a space group of $P2_1/n$. Structure and composition determinations were confirmed by synchrotron powder X-ray diffraction and electron probe microanalysis. Magnetic and electronic property measurements revealed that Cd_2FeReO_6 exhibits ferrimagnetic order well above room temperature at ~460 K, with a soft ferrimagnetic feature. Additionally, a tunneling-type magnetoresistance as large as 37% was discovered in Cd_2FeOsO_6, while first-principles calculations indicated its half-metallic state. In Cd_2FeOsO_6, significant exchange bias (EB) effects were detected under remarkably small cooling fields, revealing a unique mechanism and providing valuable guidance for the advancement of materials exhibiting significant EB effects. Both materials behave as semiconductors, in accordance with a three-dimensional variable-range hopping transport model. These results not only provide a new platform for enhancing advanced EB-effect materials but also demonstrate that A-site Cd-occupied double perovskites constitute a promising class of oxides for exploring new materials with practical significance, particularly in the realm of soft and hard magnets or in the field of spintronics.

Chapter 4 primarily focuses on the $KSbO_3$-type Fe-doped $Bi_3Re_3O_{11}$ and $Bi_3Os_3O_{11}$ compounds, synthesized under high-pressure and high-temperature conditions. Doping with Fe up to 29 atomic% was achieved under these conditions. The crystal structures and chemical compositions of $Bi_3Os_{2.45}Fe_{0.55}O_{11}$ and $Bi_3Re_{2.13}Fe_{0.87}O_{11}$ were determined through synchrotron powder X-ray diffraction and electron probe microanalysis. Both crystal structures were elucidated using a $KSbO_3$-type model with the space group *Pn*-3. Measurements of magnetic and electronic transport properties revealed that $Bi_3Os_{2.45}Fe_{0.55}O_{11}$ exhibited a ferrimagnetic transition at the highest magnetic ordering temperature of 490 K in the $KSbO_3$-type structure, while $Bi_3Re_{2.13}Fe_{0.87}O_{11}$ displayed a spin-glass behavior below 22 K. The magnetoresistance at 5 K and 90 kOe was nearly zero for $Bi_3Os_{2.45}Fe_{0.55}O_{11}$, but -10% for $Bi_3Re_{2.13}Fe_{0.87}O_{11}$. These findings suggest that $KSbO_3$-type 5d oxides, which have thus far exhibited only weak temperature-dependent paramagnetism, represent a class of compounds that can be transformed into spintronic materials through doping with 3d elements, thereby paving the way for the development of new $KSbO_3$-type materials with both theoretical and practical significance.

Chapter 5 introduces ABO_3-type perovskite oxides $MnV_{0.5}Nb_{0.5}O_3$ and $MnV_{0.5}Ta_{0.5}O_3$, prepared under high-pressure and high-temperature conditions. Structure analysis using synchrotron XRD patterns revealed that both of them crystallize in $GdFeO_3$-type structure with the space group *Pnma*. Magnetic measurements confirmed that $MnV_{0.5}Nb_{0.5}O_3$ and $MnV_{0.5}Ta_{0.5}O_3$ order ferrimagnetically at 17 and 18K, respectively. Both phases are semiconductors, with activation energies of 0.13 eV and 0.31 eV.

Chapter 6 presents the overall conclusions and future prospects based on this body of work.

Keywords: High-pressure synthesis, Crystal structure, Physical Properties, Perovskite-Related Oxides, 5*d* transition metal Oxides

List of Abbreviations

MPMS	Magnetic property measurement system
PPMS	Physical property measurement system
XRD	X-ray powder diffraction
SXRD	Synchrotron X-ray diffraction
FC	Field cooling
ZFC	Zero field cooling
T_C	Curie temperature
T_N	Neel temperature
AFM	Antiferromagnetic
FM	Ferromagnetic
t	Tolerance factor
θ	Weiss temperature
C	Curie constant
μ_{eff}	Effective magnetic moment
BVS	Bond valance sum
C_p	Heat capacity
NIMS	National Institute for Materials Science
χ	Magnetic susceptibility
ρ	Electrical resistivity

High-Pressure Synthesis, Crystal Structures and Physical Properties of Perovskite-Related 5d transition metal Oxides

Contents

Chapter 1. Introduction

1.1. Crystal structure

Crystal structure is defined as the ordered repetitive arrangement of atoms, ions or molecules in a solid material. Investigation of crystal structures has been a significant subject beneficial for materials science study and search of new useful materials due to the strong entanglement between the structure and properties of materials. In solid-state chemistry research region, ABO_3-type oxides occupy a prominent position since plenty of attractive oxide compounds could be categorized in it, including Lithium niobite ($LiNbO_3$) structure, perovskite structure, corundum structure, ilmenite structure, $KSbO_3$-type structure and so on. The study on crystal structure is the basis of the present study, and I will therefore begin with a brief introduction and description of the crystal structures involved in this paper, mainly the $KSbO_3$-type structure and perovskite structures.

1.1.1 $KSbO_3$-type structure

ABO_3-type oxides crystallize in varies structure types, including perovskites, corundum, ilmenite, pyroxenes, bixbyite, $AlFeO_3$, $KSbO_3$, $PbReO_3$, $CaIrO_3$ and others, determined by the differences of size and natural properties of A and B cations. Among the mentioned structures, the $KSbO_3$-type family is worthy for attention since some attractive properties were reported in them such as ionic conductivity and electrocatalysis in $Bi_3Ru_3O_{11}$,[1,2] notable non-Fermi-liquid behavior in structurally related $La_4Ru_6O_{19}$,[3] and the highest T_c record of 307 K among insulating and semiconducting ferromagnets in $Bi_3Mn_3O_{11.6}$ [4]. In particular, from a structural point of view, this type of structure consists of the corner and edge shared octahedra, resulting a complex tunnel-like three-dimensional framework with channels in which different units could be filled in it, which is quite interesting because with the change of the filling units, the oxygen content may change from ABO_3 to $ABO_{3.667}$. **Figure 1.1** shows the skeleton of the $KSbO_3$-type framework, the Sb_2O_{10} dimer is composed of edge-sharing octahedral pairs, with adjacent dimers located in a vertical plane to form corner sharing, thereby linking them into a geometrically frustrated 3D network.

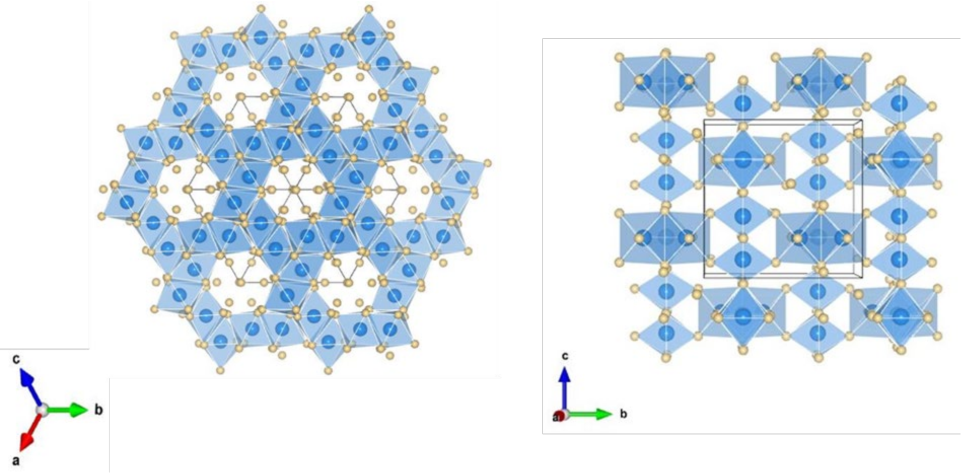

Figure 1.1. The skeleton of the $KSbO_3$-type framework viewed in different directions, the Sb_2O_{10} dimer is composed of edge-sharing octahedral pairs, with adjacent dimers located in a vertical plane to form corner sharing.

1.1.2. Perovskite and double perovskite structures

Perovskite materials were discovered in 1839 by Gustav Rose and then named after a Russian mineralogist Perovski. Its general chemical can be described as ABX_3, where A and B are cations with a larger A cation and a smaller B cation and X is the anion usually oxygen or halogens. In general, the ideal perovskite should be cubic, B cations may locate in the center of the octahedra to form the BO_6 octahedra and they may link with each other by the corners then the larger A cations are filled in the structural cavities, surrounding by 12 anions. However, most perovskites may show displacements of atoms and distortions of the octahedra due to the mismatch size of the cations and as a consequence, the symmetry may reduce by the distortions [5]. The perfect and distorted perovskites are sketched in **Figure 1.2.**

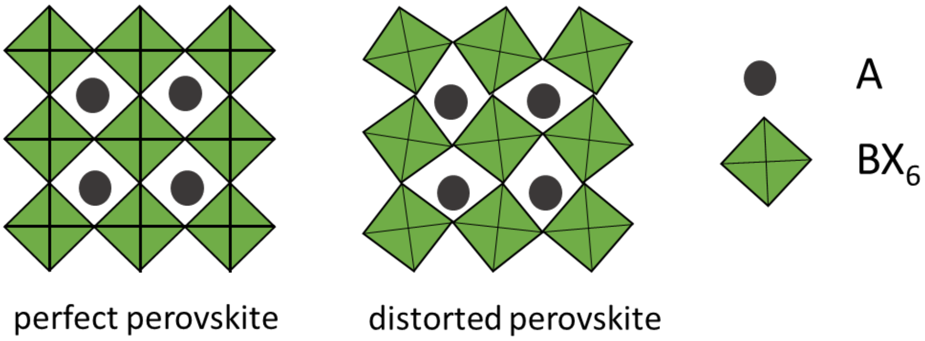

Figure 1.2. Perfect and distorted ABX_3 perovskites

Usually, most elements in the Periodic Table can be selected as both A and B occupants in perovskites, creating vast possibilities for the generation of perovskites. The stability and distortion in perovskites could be estimated by the Goldschmidt's tolerance factor, *t*:

$$t = \frac{r_A + r_O}{\sqrt{2}\,(r_B + r_O)}$$

Where r_A is the radius of the A cation, r_B is the radius of the B cation and r_O is the radius of the anion (usually oxygen). Normally, the value of *t* can be utilized to approximate the distortion degree and predict the crystal structure. For example, if $t > 1$, the perovskite structure usually be hexagonal or tetragonal; if *t* locates between 0.9 to 1, the perovskites usually belong to cubic; if *t* falls between 0.71 to 0.9, the structure should be orthorhombic or rhombohedral; if *t* is smaller than 0.71, the structure will be other different structures.

Based on the conventional perovskites, double perovskites came into being in 1950s. Compared with perovskites, partial cation substitution is involved in double perovskites and the substitution can take place either at the A or the B site, in varying degrees. Recent years, the half substitution in B-site cations has been particular interest since the B-site cations typically govern the most interesting properties of perovskites and the referring of two different B-site cations allows the combinations for the novel and unusual properties driven by different elements, ranging from 3d, 4d and 5d transition metals and some main group elements. The two different cations B and B' could remain disordered on the B-site or the difference between the oxidation states of B and B' may introduce an ordered arrangement, forming a so-called B-site ordered double perovskite, which could be presented by the general formula $A_2BB'O_6$ (A is divalent or trivalent metal element, B and B' are 3d, 4d or 5d transition metal elements). Commonly, there are three types of B-site ordering $A_2BB'O_6$ double perovskites, as shown in **Figure 1.3** below [6]:

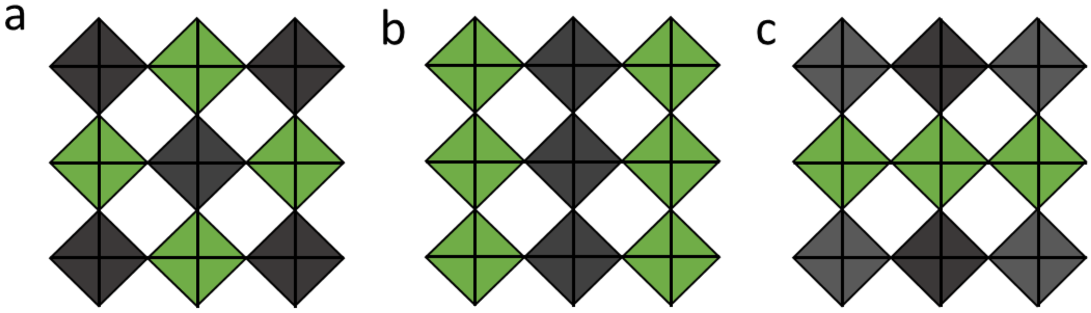

Figure 1.3 B-site ordering schemes in double perovskites $A_2BB'O_6$, (a) rock-salt, (b) columnar orderings and (c) layered orderings. The BO_6 and $B'O_6$ octahedra are drawn in different colors [6].

Among them the rock-salt-type arrangement is the most common case, which is also known as the elpasolite structure after the discovery of K_2NaAlF_6. Sometimes the layered order may occur occasionally, in this situation, the B and B' cations alternate only in one dimension. The columnar order is rare to take place, in which the two different B cations alternate in two directions.

So far, there is an explosion of research into double perovskites, as the BB' position allows for the combination of a large number of different elements, such as: Ba_2MgReO_6 [7], Sr_2BOsO_6 (B=Y, In, Sc) [8], Sr_2CrReO_6 [9,10], Sr_2CrOsO_6 [11], Sr_2FeReO_6 [12], Sr_2FeOsO_6 [13], Sc_2NiMnO_6 [14], A_2FeReO_6 (A = Ca, Ba) [15,16], Y_2NiMnO_6 [17], Y_2MnCrO_6 [18], Y_2CoMnO_6 [19], Pb_2FeOsO_6 [20], Pb_2FeReO_6 [21], Pb_2BReO_6 [22] (B = Co, Cr), Ca_2BOsO_6 (B = Ni, Co) [23], Mn_2CoReO_6 [24], Mn_2NiReO_6 [25], Mn_2LiReO_6 [26], Sr_2FeMoO_6 [27,28], Ca_2MnOsO_6 [29]. As the combination of elements changes, the performances could also vary from metals to insulators, distributing from antiferromagnet, ferrimagnet, ferromagnet as well as spin glass and so on.

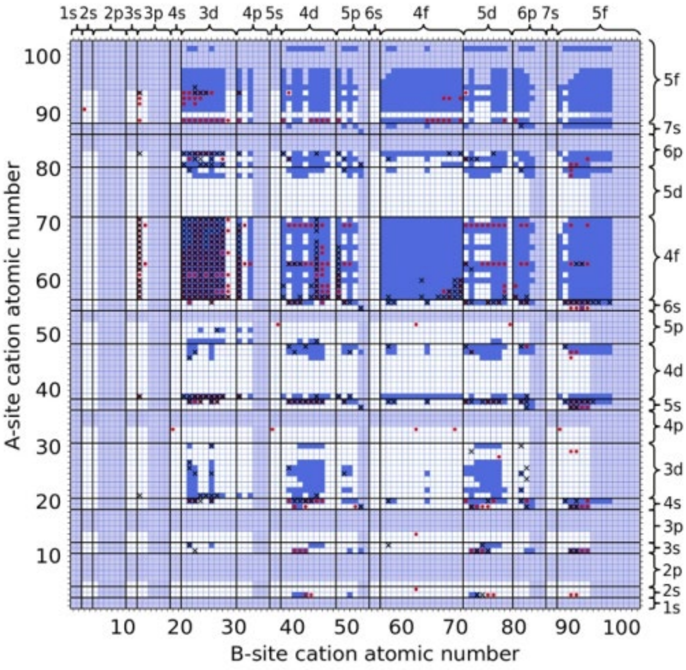

Figure 1.4. ABO_3 ternary compounds classified as perovskites by geometric model (blue squares), ab initio calculations (red circles) reported by Emery et al., and experimental data (black crosses). [30] (Copyright © 2023 National Academy of Science. All rights reserved.)

Although the substitution on A-site could happen, it will expand the number of perovskites considerably, as can be seen in **Figure 1.4** [30], even just for the simplest ABO_3 single perovskites, there are still more than 100,000 new perovskites waiting to be discovered, so I do just limit the investigation in B-site ordered and disordered compounds with a single A-site cation. Details will be elaborated in subsequent chapters 4 and 5.

1.2. 5*d* transition metal oxides

In chemical terms, the transition metal means the chemical element which obtains a partially filled *d*-subshell that can be engaged in chemical bonding. The transition metals usually locate in the *d*-block of the periodic table, as sketched in **Figure 1.5.** [31] According to the extended degree of orbitals, the transition-metal system can be divided into 3*d*, 4*d* and 5*d* series. Compared with the 3*d* and 4*d* counterparts, 5*d* elements have the most extended orbitals, thus the extended 5*d* orbitals may overlap more with the nearest neighbor ions and result in a broader bandwidth.

Figure 1.5. Periodic table. Enlarged area shows transition elements of *d*-block, which consists of 3*d*, 4*d* and 5*d* series [31]

Complex oxides with 5*d* transition-metal ions have been attracting lots of attention recent years due to the 5*d* electrons on the spatially extended *d* orbitals and notable spin-orbit coupling (SOC). The former may cause a smaller Coulomb repulsion (U) for 5*d* electrons while the later can be compared with or even larger than some other relevant parameters such as Hund's coupling J_H and the electron hopping amplitude *t*. Simultaneously, 5*d* cations prefer a low-spin configurations rather than a high-spin configuration due to the large crystal-field. The non-trivial competing between SOC, U and noncubic crystal field enables the exploration of various intriguing properties, such as Mott insulator [32], high T_c superconductivity [33], quantum spin liquids [34], multipolar ordering [7], topological insulating behavior [35] and so on. **Figure 1.6** [36] gives a simple phase diagram to present several novel physical ground states determined by the relative strength of the electron correlation (*U/t*) and the SOC (*λ/t*). It is clear from the diagram that through the investigation and control of the electron correlation and SOC will be very helpful for the design and exploration of new materials with exotic states.

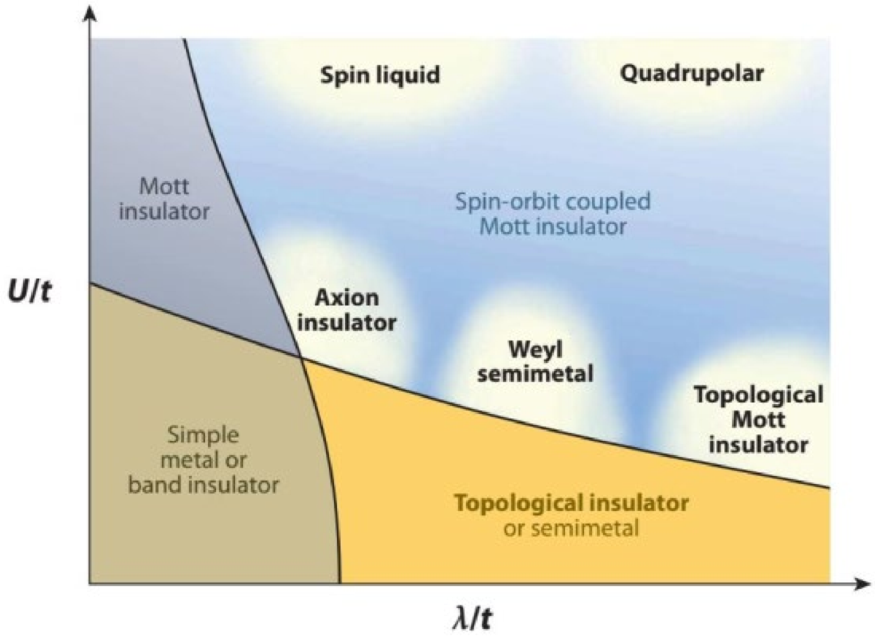

Figure 1.6. A simple phase diagram to present several novel physical ground states determined by the relative strength of the electron correlation and the SOC. [36] (Copyright © 2010, Annual Review of Condensed Matter Physics)

To date, there is still very limited research on 5*d* metal oxides and therefore my research focused on this region with the aim of exploring new exotic properties for 5*d* transition metal oxides.

1.3. Magnetism

1.3.1. Classification of magnetic behaviors

Many different types of magnetic orders are simply sketched in **Figure 1.7**. From top to bottom, paramagnetic, ferromagnetic, antiferromagnetic as well as ferrimagnetic.

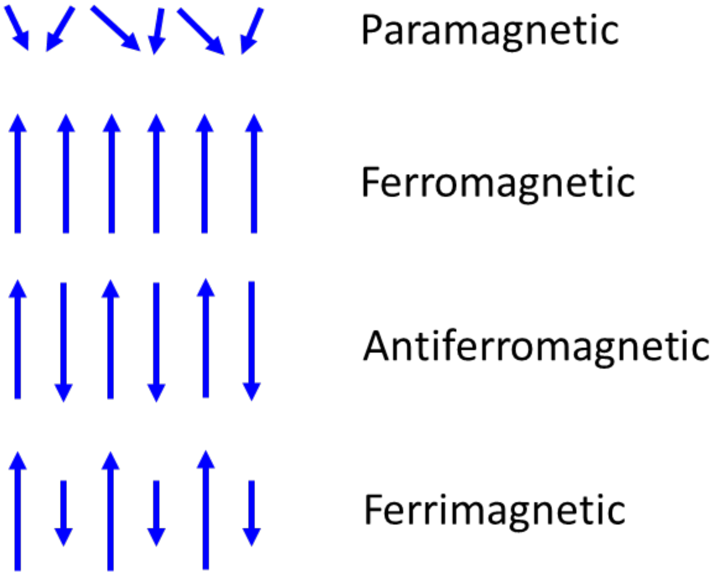

Figure 1.7. Schematic illustration of paramagnetic, ferromagnetic, simple antiferromagnetic and ferrimagnetic spin arrangements.

Generally, the magnetic species are distinguished mainly on the basis of the arrangements of unpaired electrons in the material. In paramagnets, the unpaired electron spins may orient randomly inside the material, in ferromagnets, all of the unpaired electron spins are arranged in parallel, in antiferromagnets, the spins are aligned antiparallel while ferrimagnetic order is a special case of antiferromagnetic order in which the spins are aligned oppositely as well but the moments corresponding to different directions are unequal therefore net moments may remain in ferrimagnets [37].

In particular, through the investigation of the three-dimensional magnetic structures of manganite perovskites, it was found that among them the antiferromagnetic order could be subdivided into three structure types [38], as shown in **Figure 1.8**, A-Type, C-Type and G-Type.

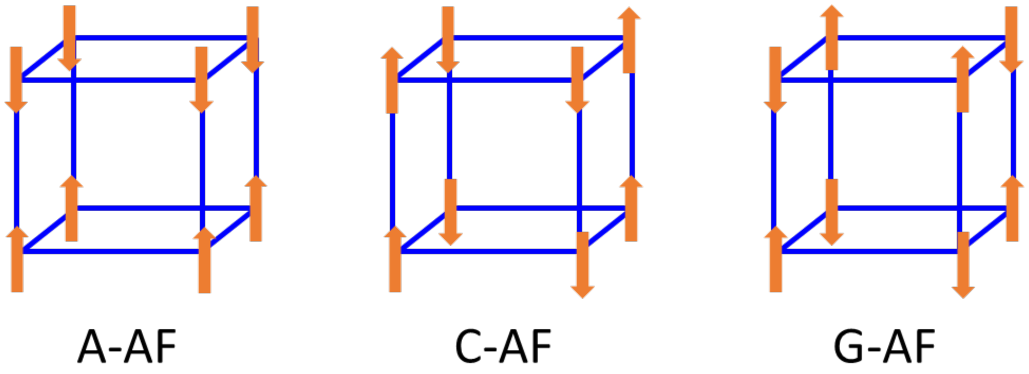

Figure 1.8. A-AF, C-AF and G-AF antiferromagnetic structures.

The magnetic situation in a material is usually determined by the competition between atomic magnetic interactions and thermal motion of atoms. At high temperatures, the thermal motion of the atoms plays a dominant role and the material becomes paramagnetic. When the temperature decreases, the magnetic interactions between the atoms begin to function and long-range magnetic ordering is established. As the temperature drops further and the magnetic interactions between the atoms become dominant, the ferromagnetic, ferrimagnetic, antiferromagnetic states may occur. This transition temperature is referred to as the Curie temperature (corresponding to ferromagnetic and ferrimagnetic order) or the Neel temperature (corresponding to antiferromagnetic order).

1.3.2. Magnetic exchange

1.3.2.1. Heisenberg direct exchange interaction

In order to explain the ferromagnetism of materials, in 1928, Heisenberg proposed the direct exchange interaction through the chemical bonding between adjacent magnetic atoms is responsible for the spontaneous magnetization of the material, and established the Heisenberg model to reveal the nature of spontaneous magnetization of ferromagnetic materials. He extended the exchange interaction model for hydrogen to multi-atom systems, giving the following Heisenberg model:

$$E_{ex} = -A \sum_{i<j} S_i \cdot S_j$$

Where A is the exchange integral and the latter item is the exchange energy.

1.3.2.2. Superexchange

In some oxides, the magnetic ions are far apart and separated by non-magnetic anions such as oxygen, at this point it is difficult to realize significant overlap between the electron clouds of magnetic cations, making it difficult for the Heisenberg direct exchange mechanism to be effective. In 1934, Kramers [39] first suggested that exchange interaction in ionic crystals could be achieved indirectly through the anion, known as superexchange later [40]. As shown in **Figure 1.9**, in NiO, the p orbitals of the O^{2-} ion contain two electrons each, which are coupled antiparallel, and these two electrons on the same anion could couple two close cations antiparallel, respectively as well.

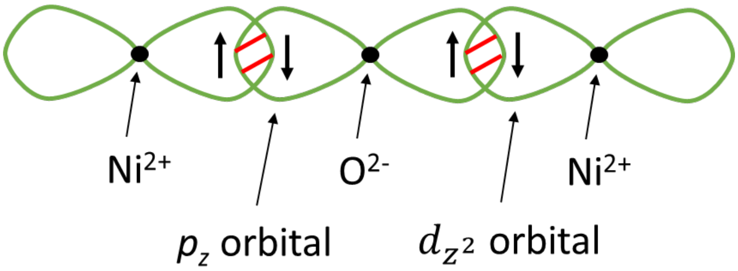

Figure 1.9. Schematic representation of the superexchange of NiO.

In general, the superexchange interaction is strongest when the cation-anion-cation bond was aligned on 180º, and if there is a 90º angle between the two cations and the anion, the superexchange interaction is weakest.

In conclusion, the theory of superexchange interaction explains well some cases of antiferromagnetic ordering, such as NiO, MnO and so on. Later, P. W. Anderson [41] systematized this theory in 1950 and Goodenough [42] refined it in 1955 again, which has been successful in explaining some magnetic structures that can not be illustrate by ionic bonding theory, typical examples being their application in revealing the magnetic structures of $LaMnO_3$ and $CaMnO_3$.

1.3.2.3. Double exchange

In 1950, Jonker and Van Santen found that there is a strong correlation between the magnetic transition and electrical conductivity in a series of doped $La_{1-x}Ca_xMnO_3$ [43]. Later, in 1951, Zener [44,45] proposed the double exchange interaction and successfully explained the ferromagnetism in the mixed-valences manganite perovskite oxides. His view is that, electrons could move simultaneously inside the mixed-valences manganite, the route can be explained as: $\mathbf{Mn^{3+}_{1\uparrow}O_{2\uparrow,3\downarrow}Mn^{4+} \rightarrow Mn^{4+}O_{1\uparrow,3\downarrow}Mn^{3+}_{2\uparrow}}$, which means that electron 2 may move from oxygen to Mn^{4+} and electron 1 may move to oxygen from Mn^{3+} [46].This process could be illustrated graphically by **Figure 1.10**.

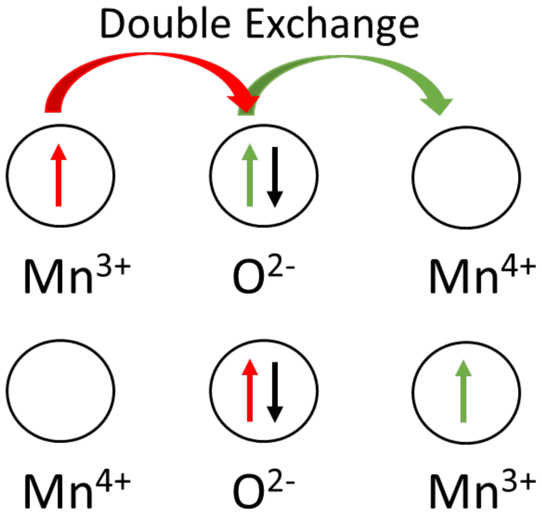

Figure 1.10. Scheme of the double exchange mechanism

1.4. Magnetic-related physical mechanisms

1.4.1. Geometric frustration magnets

‘Frustration’ implies the system is unstable and it is hard to find a unique ground state, which is common to occur in disordered solids. Whereas, it could be also discovered in ordered solids, deriving from geometric considerations, and it is gradually being seen to control many physical phenomena through the atomic collective behaviors. Since the properties of solids are determined not only by the positions of atoms, but also affected by their intrinsic local interactions, such as magnetic order, rotational degree of freedom. When the crystal symmetry is not compatible with the mutual interaction between moments, what will happen? A representative example is the antiferromagnetism, in which the magnetic moments of adjacent atoms tend to align reversely. As shown in **Figure 1.11** [47], in a triangular lattice, no matter how the residual moment is arranged all three spins cannot be antiparallel simultaneously, this unsatisfied bond is said to be frustrated.

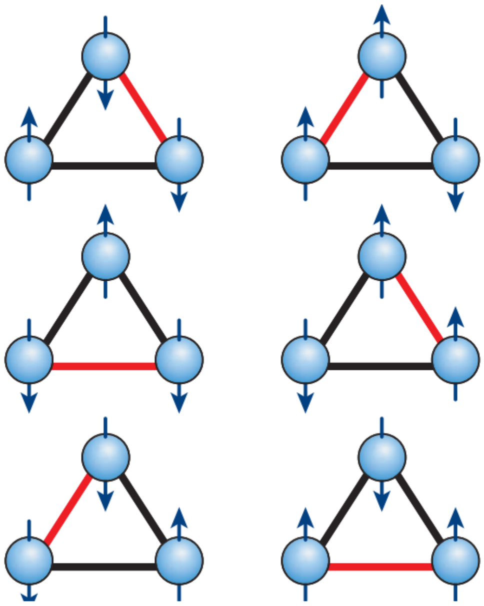

Figure 1.11 A simple diagram of frustrated situation in the triangular lattice system. [47] (Copyright © 2010, Springer Nature Limited)

Extending this situation to systems containing more such triangles, things will become much more complex, as displayed in **Figure 1.12**, [47] the orientations of the spins will depend more on the circumstances and the intrinsic order will be less obvious.

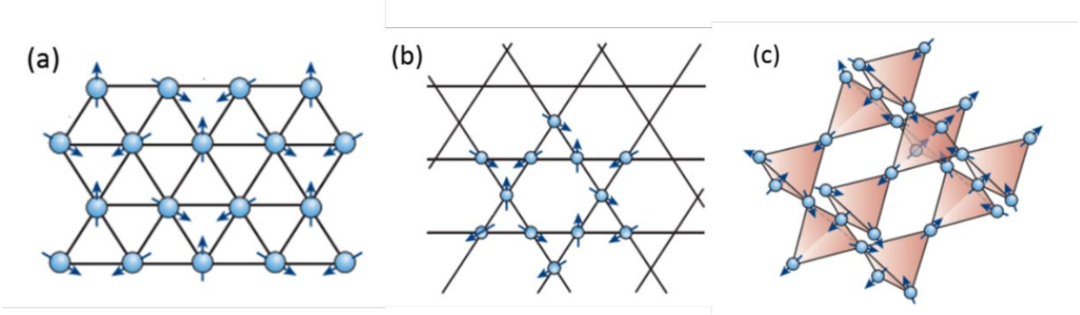

Figure 1.12. Frustrated magnetism on 2D and 3D lattice. (a) a triangular lattice. (b) a Kagome lattice. (3) the 3D pyrochlore lattice. [47] (Copyright © 2010, Springer Nature Limited)

In summary, geometric frustration is an important phenomenon in magnetic materials and the competing interactions inside the frustrated systems may give rise to huge degeneracy of the ground state of the material [47] and compared with regular systems, it may possess more configurational options which make these frustrated systems possible to obtain practical utilizations in areas such as microelectronics, drug delivery and so on. [48]

1.4.2. Magetoresistance

Magnetoresistance (MR) is the change in the resistance of materials in response to an external applied magnetic field. [49] Typically, it can be divided into five sub-categories: ordinary magnetoresistance (OMR), anisotropic magnetoresistance (AMR), giant magnetoresistance (GMR), tunneling magnetoresistance (TMR) and colossal magnetoresistance (CMR).

Ordinary Magnetoresistance usually occur in non-magnetic metals and the change in resistivity $\Delta\rho$ is positive. The reason is that, for all non-magnetic metals, due to the Lorentz force caused by the magnetic field, conduction electrons will be deflected in their path, making the path follow a curve, which will increase the length of the path of electrons and enhance the chance of collisions of electrons, therefore, the resistance of the material may increase. In general, OMR effects are very small at low fields, but with the increase of magnetic fields, the effect can become quite large.

Anisotropic magnetoresistance means that the variation of magnetoresisitance in some materials is related to the angle between the magnetic field and the current. The physical roots for AMR lie in the coupling of spin orbitals. As the magnetization direction rotates, the electron cloud around each nucleus is distorted slightly, and this distortion changes the amount of scattering conducting electrons. A plausible explanation is that, if the magnetic field is oriented perpendicular to the current, the electron orbitals are in the plane of the current, which may decrease the cross-section for scattering, producting a low resistance state. In contrast, for a field parallel to the current, the electron orbitals are perpendicular to the current and the cross-section of the scattering increases, resulting a high resistance state.

Giant magnetoresistance effect exists in ferromagnetic/non-ferromagnetic multilayer systems (as shown in **Figure 1.13**), where the non-magnetic layers may change the behavior of the conduction electrons in the magnetic layers, resulting in varying degrees of magnetic scattering of the electrons, causing a much larger resistance (up to ~50%) [50,51] than the normal magnetoresistance, thereby it was named ‘giant magnetoresistance’.

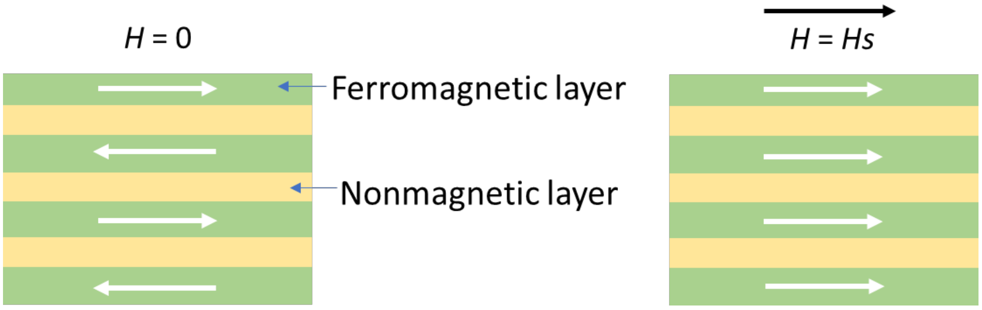

Figure 1.13. A typical GMR structure.

Typically, Tunnel magnetoresistance effect is a phenomenon that occurs in a magnetic tunnel junction, which has been demonstrated for a trilayer component consisting of two ferromagnetic layers intervened by a nonmagnetic-insulating layer [52], as sketched in **Figure 1.14**. If the insulating layer is very thin, the electrons could jump from one ferromagnet to the other. The two magnetization directions of the ferromagnets can be controlled individually by the external magnetic fields. Hence when the magnetization directions of the two ferromagnets are parallel, electrons are more likely to tunnel through the insulating film, as opposed to anti-parallel. As a consequence, such junctions can switch between a low resistance and a very high resistance. Recently, TMR was observed in some perovskite-type transition-metal oxides as well, and field control of the spin dependent scattering of carriers at the grain boundary seems to be the reason for the TMR appearance in polycrystalline samples. [53]

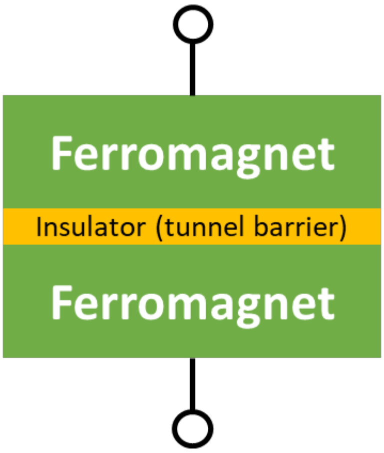

Figure 1.14. A Schematic magnetic tunnel junction (MTJ).

Colossal magnetoresistance mainly be discovered in manganese-based perovskites. The generation mechanism is totally different from and often much larger than GMR (more than three orders of magnitude larger than the typical GMR [54]). In CMR, the addition of a magnetic field most likely enhances the alignment of the spins thus decreases the resistivity. Alternative mechanism is that the distances between the magnetic ions are particularly important and the external magnetic field will affect the indirect exchange interactions which are contribute to conductivity as well. In practice, a fully quantitative understanding of the CMR still remains elusive and the development of CMR technologies still remains as a question.

1.4.3. Exchange bias (EB) effects

The design and control of special magnetic properties are pivotal in the manufacture and application of new materials. The EB effect is an important feature that can be utilized to control one of the most significant parameters – coercivity in ferromagnets. As sketched in **Figure 1.15**, the EB effect may result in a shift of the hysteresis loop along the magnetic field axis. Here H_E is the exchange bias field, H_{c1} and H_{c2} are the left and right coercive fields.

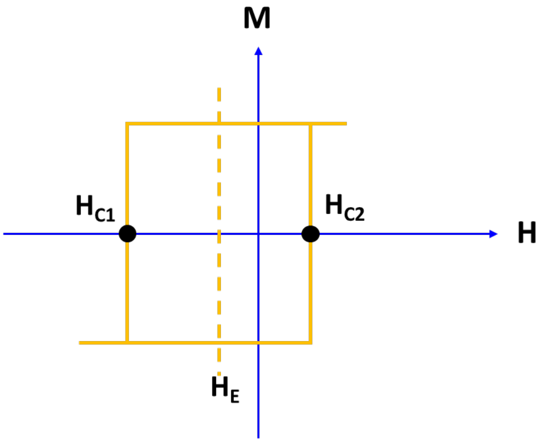

Figure 1.15. Shifted hysteresis loop in an EB ferromagnet.

One of the major effects of EB effect is to make it more difficult to reverse the magnetization. We can see that when the hysteresis loop is shifted, to reverse the magnetization direction, a magnetic field larger than H_{c1} needs to be applied. As I mentioned in the previous section on GMR [50] and MTJ [52], the fix of the magnetization direction of a particular ferromagnetic layer is required in the practical application of GMR or MTJ, therefore, a significant Exchange Bias effect will be very helpful in increasing the storage density and reducing the size of the electronic devices, which is expected to dramatically improve the performance of spintronic devices and magnetic tunnel junctions.

The phenomena of exchange bias usually occur at the FM/AFM interface where the ferromagnetic and antiferromagnetic interaction can compete with each other [55]. And the way to obtain the shifted hysteresis is: First, an applied magnetic field is added above the ordering temperature T_N of the antiferromagnet to align the magnetic moment in the field direction, second, cooling the sample below T_N while maintaining the applied field. Then a shift of the hysteresis loop along the magnetic field axis may appear if the magnetization measurements are performed subsequently.

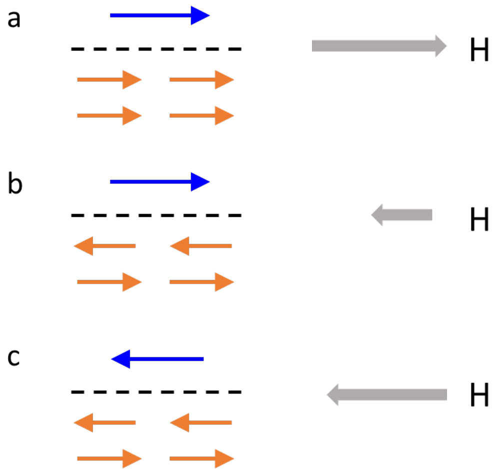

Figure 1.16. A schematic diagram for the basic mechanism for EB effect. (a) Beyond T_N, an additional magnetic field is applied in order to align the ferromagnet spins. (b) After cooling process under an applied field, an anti-parallel coupling between the FM and AFM layer is forming. (c) A larger applied field is required to reverse the magnetization direction of the ferromagnet.

A schematic diagram of the basic mechanism for the formation of EB effect is shown in **Figure 1.16.** In panel (a), the magnetic field is applied at a temperature above T_N, which may align the ferromagnetic spins and during cooling the magnetic field maintains thus the magnetization remains pinned along the original direction when small negative fields was added, as in panel (b). Since the spin orientation of antiferromagnets is only weakly affected by an applied magnetic field, interfacial spins of a soft ferromagnetic layer may be pinned by the strongly exchange-coupled antiferromagnet, therefore, an additional energetic consumption is necessary in reversal of the ferromagnet's spins as well as the propulsion of a Neel domain wall within the antiferromagnetic layer. Only if the applied field is large enough to overcome the interlayer exchange between the FM and AFM interface, the reverses of the ferromagnet could be realized. This is why larger magnetic field is required for the reverse of magnetization.

In the current era of the information age, research on data access is driving global technological innovation. Magnetic recording devices heavily rely on the exchange bias (EB) effect to precisely fix the state of the readout head in hard disk drives. Traditional EB effects primarily occur in layered materials and necessitate large cooling fields (typically tens of kOe) to achieve significant EB effects, leading to challenges in manufacturing and energy consumption. Consequently, there has been a concerted effort to develop new materials and technologies that enable substantial EB effects with small cooling fields in a single phase. Recent years, EB effects have been found successfully in some structurally homogeneous systems in which various magnetic phases co-exist. The atomic disorder seems to be the contributing factor, a typical example is the ferrimagnetic Heusler alloy $Mn_{3-x}Pt_xGa$ which contains giant EB effects [56], the origin of the considerable EB effects could be traced to the ferrimagnetic clusters in the compensated host, which are generated as a consequence of antisite disorder. In a similar vein, DPs may also supply different lattice positions for magnetic ion as well as the antisite disorder is frequently prone to [57]. Therefore, the relative study on such DPs may provide promising platform for obtaining an enhanced EB effect which can be triggered by a small cooling filed in a single phase at room temperature.

1.5. Material conductivity models

Electrical resistivity ρ is a physical quantity that describes the electrical conductivity of a material. Resistivity is numerically equal to the resistance of a substance per unit length, per unit cross-section, which could be calculated by the formula $\rho = RS/L$, where R is the electrical resistance of a uniform specimen of the material, S is the cross-section area and L is the length of the material. Whereas, it should be noted that resistivity is independent of factors such as the length and cross-sectional area of a conductor, it is an electrical property of the conductor material itself, determined by the material of the conductor and is temperature dependent.

According to the band theory, the intrinsic resistivity of a material is determined by the number of electrons contained in the 'conduction band' and materials can be classified as conductors, semiconductors and insulators depending on their band structure [58]. **Figure 1.17** shows the simplified diagram of the electronic band structure of insulator, semiconductor and metal. Commonly, insulator have a large energy gap (usually greater than 9 eV), making it very difficult for electrons to jump from the valence band to the conduction band and therefore unable to conduct electricity. In contrast, the conduction band and valence band have an overlap region in metallic conductors, thus electrons could move freely and conduct electricity. In the middle case, semiconductor materials in general have an energy gap of about 1~3 eV, in this situation, a suitable energy excitation could help electrons overcome the energy barrier. When electrons gain energy and jump from the 'valence band' to the 'conduction band', electrons could move freely between the bands and conduct electricity.

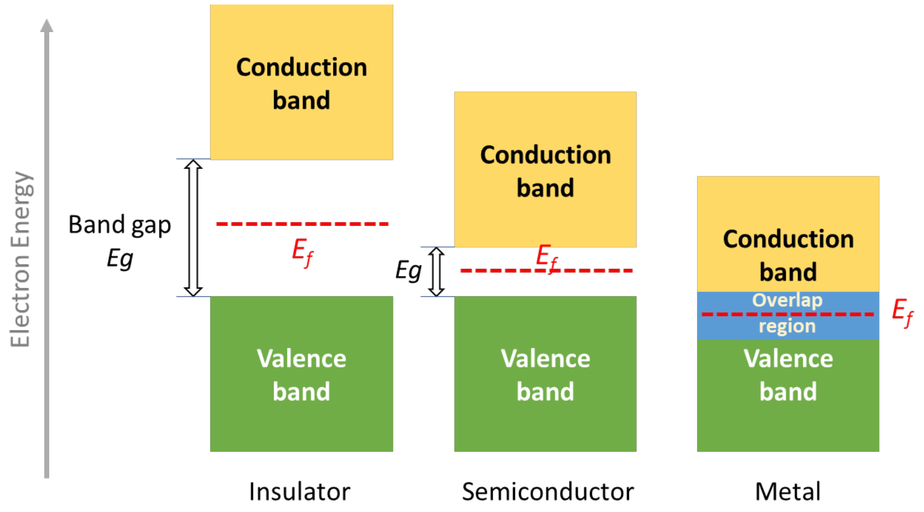

Figure 1.12. Simplified diagram of the electronic band structure of insulator, semiconductor and metal.

In most materials, resistivity varies with temperature, but different mechanisms of material conductivity can result in different relationships. Below I briefly introduce a few models on resistivity temperature dependence.

1.5.1. Conduction in metals

The high electrical conductivity of metals has long been discovered and exploited, and the conductivity-temperature relationship has a significant impact on the application of the material. Thus, a large number of experimental studies have been carried out, yielding a number of regular results. The following formula is a general and typical result:

$$\rho = \rho_0 + \rho_l(T)$$

From the formula we can see the resistivity of a metal can be clearly divided into two separate parts, the first part is independent of temperature and is called residual resistance, it is related to defects and impurities in the metal, the second part is temperature dependent and is called intrinsic resistance. It decreases as the temperature decreases, $T \to 0\text{K}$, $\rho_l \to 0$, it is tentatively determined to be caused by lattice vibrations. Experiments have shown that most metal resistivities at room temperature are mainly governed by phonon collisions, and by impurities and defects scattering under 4K.

1.5.2. Thermal activation conduction model

For classical semiconductors, the electrons need to overcome the bandgap energy E_{gap} to move freely and contribute to the conduction. When the energy to overcome E_{gap} comes from the thermal energy, then the resistivity-temperature dependence can be given by the following formula [59]:

$$\rho \propto \exp\left(\frac{E_a}{k_B T}\right)$$

Here E_a is the activation energy, k_B is Boltzmann's constant and T is the temperature. This Arrhenius-type transport could be used to estimate the activation energy and since for classical non-doped semiconductors E_a is usually equal to $E_{\text{gap}}/2$, the band gap could be roughly calculated as well.

1.5.3. Variable range hopping model

In the low temperature region, different conduction mechanisms appear. In this situation, the hopping conduction process is discovered, the resistivity is logarithmically related to temperature and the temperature-dependent relationship could be described by the VRH model:

$$\ln\rho(T) \propto (T_0/T)^{-1/n}$$

where n is related to the shape of the DOS at the Fermi level [60]. In the low temperature region there are four possible n values ($n = 1, 2, 3, 4$) have been examined, corresponding to different conduction mechanisms for carrier conductive behavior of semiconductors: i) $n = 1$, the 'hard gap' conductivity mode, it is often observed in systems which contain many-electron excitation effect, usually there will be a hard gap in the DOS near Fermi level. [61] ii) $n = 2$, the Efros and Shklovskii VRH mode, long-range electron-electron Coulomb interaction exists in the system and the DOS vanishes quadratically at the Fermi level. [62] iii) $n = 3$, usually for 2D systems [63]. iv) $n = 4$, the Mott VRH model, for disordered systems without Coulomb interaction, in this case the DOS is presumed to be a constant near the Fermi energy. [64]

1.6. High-pressure science

Pressure is a significant thermodynamic variable which could be used to determine the basic state of matters. Under high pressure, the atomic arrangement, crystal structure or electronic structure in a substance may show suddenly changes in the physical properties of the substance, such as the transformation of an insulator into a metal, significant changes in resistance, electrical or magnetic properties and volume. Also, materials could transport from one state to another, for example, graphite could turn into beautiful diamond. Thereby, the investigation of high-pressure science could not only help us better understand the natural substances in the world around us, but can also help men create entirely new matters.

1.6.1. History of high-pressure science

Although high pressure has been routinely utilized by nature for billions of years in the creation and maintenance of the Earth's mantle, it was only at the end of the last century that mankind began to systematically study the phenomenon of high pressure. The father of modern high-pressure technology, American physicist Percy Willams Bridgman played a pivotal role in the history of high-pressure development. He developed techniques to reach pressures up to 10 GPa in the early 20th century, then exploited this technique to achieve a wealth of research results in the areas of compressibility, thermal conductivity, electrical resistance, viscosity and polymorphic transitions of matters, which greatly advanced the development of solid-state physics. He was also awarded the Nobel Prize for Physics in 1946 for his enormous contribution to the development of high-pressure science.

Based on his contribution, after the 1950s, different high-pressure devices such as the Belt-type high pressure device, the hexahedral high-pressure device, the octahedral high-pressure device, etc. have been improved continuously, the pressure limitation was also raised from an initial 6 GPa to over 50 GPa as well. In 1959, Lawson et al. at the Chicago University had successfully assembled the world's hardest known diamond on the anvils and firstly achieved the high-pressure limit of 100 GPa. In 1986, Xu and Mao et al. of the Geophysical Laboratory of the Carnegie Institute, USA, produced the highest static high-pressure limit to date, 550 GPa. [65]

1.6.2. High-pressure in material science

High-pressure synthesis has a number of advantages in the field of material synthesis.

Firstly, the compression of the interatomic distances inside substances under high pressure may lead to a series of changes in structural and physical properties, even making it possible to obtain meta stable substances which are difficult to gain at atmospheric pressure. For example, the material $HgBa_2Ca_2Cu_3O_{8+\delta}$ [66], which almost unnaturally presents in nature, possesses a high value of the superconducting transition temperature of around 164K; the oxide $LiOsO_3$ [67], which undergoes a ferroelectric-like transition in metallic state, could be synthesis only under high pressure as well.

Secondly, samples in the high-pressure synthesis system are well isolated from the outside and can be approximated as an adiabatic system in which ions of anomalous oxidation valence can be obtained by creating a high or low oxygen pressure environment, for example, the pentavalent manganese ion is found in high-pressure synthetic oxide $Bi_3Mn_3O_{11}$ [68], which is very rare in oxides.

Thirdly, materials available on an industrial scale can be obtained by means of high-pressure synthesis. Very typical is the application of high-pressure synthesis in the obtain of diamonds and cubic boron nitride (c-BN), which are the super abrasives of choice when cutting and shaping hard metals and ceramics. [69]

Fourthly, the reaction rate is greatly increased under high pressure since the contact between the raw powders is so tight that the atoms could diffuse very quickly. Solid state reactions that normally take days or even weeks at atmospheric pressure can be completed in a few minutes under high-pressure.

In summary, high-pressure synthesis plays an important and irreplaceable role in exploring the synthesis of new materials and in understanding and modifying the properties of existing materials.

1.7. Targets and structure of this thesis

The main motivation for the work in this thesis is the synthesis of new 5*d* transition metal related oxides and the exploration of their possible exotic new properties. The whole thesis is divided into six parts, the first part gives a brief overview of the crystal structures and some physical properties relevant to my work, in the second part the instrumentations and experimental methods used are described, the third to fifth chapters present new 5*d* transition metal containing oxides synthesized under high-pressure and high-temperature conditions and their crystal structures and physical properties. Of these, there are three main topics included as below:

(i) Double Perovskites Cd_2FeOsO_6 with Large Exchange Bias and Cd_2FeReO_6 with High-Temperature Ferrimagnetic Ordering as well as Tunneling Magnetoresistance

Double perovskite oxides (DPs) combing 3*d* and 4*d*/5*d* transition metal elements are the frontier hot spot for materials research over the past few decades due to variety outstanding properties had been reported for spintronics applications [70–72]. Normally, DPs have a general formula $A_2BB'O_6$, where A is alkaline or rare earth ion meanwhile B/B' are transition metal ions, however, in 2015, Li et al. found small transition metal cation could be used as A-site occupant in DPs and excellent properties were discovered [73]. Inspired by this discovery, I tried to induce another transition metal element as the A-site occupant. I noticed the Cd^{2+} ions are slightly smaller in size than the widely used Ca^{2+} ions ($r_{Cd}{}^{2+}$ = 1.31 Å; $r_{Ca}{}^{2+}$ = 1.34 Å), whereas, Cd^{2+} ions obtain larger Pauling electronegativities ($\chi_{Cd} = 1.69$; $\chi_{Ca} = 1.00$), which is possible to lead many exotic phenomena [74], such as a covalency-driven structural evolution in the polar Cd-Nb-O pyrochlore system [75] and ferroelectric phase transition in perovskite-type oxides $CdTiO_3$ [76]. Consequently, Cd^{2+} was selected as the candidate and two new DPs Cd_2FeOsO_6 and Cd_2FeReO_6 were obtained under high pressure high temperature synthesis and their crystal structure, electronic and magnetic properties will be presented in **Chapter 3.**

(ii) High-pressure synthesis and magnetic and electrical properties of Fe-doped $Bi_3Re_3O_{11}$ and $Bi_3Os_3O_{11}$

$KSbO_3$-type structure is a forgotten family among the ABO_3 compounds due to the lack of interesting physical properties. Most of them just show no long-range magnetic ordering down to low temperatures and in particular, 5*d* oxides do not show any special 5*d* features, just exist weak temperature-dependent paramagnetism. In order to investigate the possibility of enhancing the material properties, doping with 3*d* element-iron on two 5*d* oxides were tried under high temperatures and pressures. $Bi_3Re_{2.13}Fe_{0.87}O_{11}$ and $Bi_3Os_{2.45}Fe_{0.55}O_{11}$, two Fe-doped 5d oxides were synthesized and their crystal structures, physical properties will be discussed in detail in **Chapter 4**.

(iii) High-Pressure Synthesis and Ferrimagnetism of Perovskites $MnV_{0.5}M_{0.5}O_3$ (M=Nb,Ta)

ABO_3-type perovskite oxides exhibit a rich variety of interesting phenomena, usually, the non-magnetic alkaline or rare earth ion will be used to occupy *A*-sites but it was found that filling of the *A*-sites with magnetic transition metal cations is possible under high-pressure conditions. Recent studies on unusual "*A*-site manganite'' opened great opportunities for stabilizing unusual physical properties such as multiferroism in $CaMnTi_2O_6$ [77] and high-T_C ferrimagnetism in Mn_2FeReO_6 [78]. Meanwhile, based on Hill's assumption [79], the d^0 configuration may contribute to the induction of ferroelectricity, such as the well-known $BaTiO_3$ [80]. Taking the above into account, the introduction of d^0 configuration into the *A*-site manganite is very promising for the exploration of multiferroic formation. Thus, I attempted to insert d^0 ions Nb^{5+} and Ta^{5+} into the original *A*-site manganite $MnVO_3$ and two new perovskites $MnV_{0.5}Nb_{0.5}O_3$ and $MnV_{0.5}Ta_{0.5}O_3$ have been synthesized at high-pressure and high-temperature conditions. In **Chapter 5,** their synthesis, crystal structure, magnetic and electronic behaviors will be illustrated.

Finally, in **Chapter 6**, I will offer a summary of the present work and the prospects for subsequent research.

References in Chapter 1

(1) G. R. Facer, M. M. Elcombe, B. J. Kennedy. Bismuth Ruthenium Oxides. Neutron Diffraction and Photoelectron Spectroscopic Study of $Bi_2Ru_2O_7$ and $Bi_3Ru_3O_{11}$. *Aust. J. Chem.* **1993**, *46* (12), 1897–1907.

(2) T. Fujita, K. Tsuchida, Y. Yasui, Y. Kobayashi, M. Sato. Transport, Thermal and Magnetic Properties of $Bi_3Os_3O_{11}$ and $Bi_3Ru_3O_{11}$. *Physica B: Condensed Matter* **2003**, *329–333*, 743–744.

(3) P. Khalifah, K. D. Nelson, R. Jin, Z. Q. Mao, Y. Liu, Q. Huang, X. P. A. Gao, A. P. Ramirez, R. J. Cava. Non-Fermi-Liquid Behaviour in $La_4Ru_6O_{19}$. *Nature* **2001**, *411* (6838), 669–671.

(4) A. A. Belik, E. Takayama.M. Effects of Oxygen Content on $Bi_3Mn_3O_{11+\delta}$: From 45 K Antiferromagnetism to Room-Temperature True Ferromagnetism. *J. Am. Chem. Soc.* **2010**, *132* (35), 12426–12432.

(5) Ming-Gang Ju, Jun Dai, Liang Ma, Xiao Cheng Zeng. Perovskite Chalcogenides with Optimal Bandgap and Desired Optical Absorption for Photovoltaic Devices. *Advanced Energy Materials* **2017**, *7* (18), 1700216.

(6) Neda Rahmani, Mohammad Ebrahim Ghazi, Morteza Izadifard, Alireza Shabani, Jost Adam. Designing New Ferromagnetic Double Perovskites: The Coexistence of Polar Distortion and Half-Metallicity. *Physical Chemistry Chemical Physics* **2021**, *23* (35), 19571–19578.

(7) D. Hirai, H. Sagayama, Shang Gao, H. Ohsumi, Gang Chen, T. Arima, Z. Hiroi. Detection of Multipolar Orders in the Spin-Orbit-Coupled 5d Mott Insulator Ba_2MgReO_6. *arXiv: Strongly Correlated Electrons* **2020**.

(8) Sudipta Kanungo, Binghai Yan, Claudia Felser, Martin Jansen. Active Role of the Nonmagnetic Cations in Magnetic Interactions for the Double-Perovskite Sr_2BOsO_6 (B=Y, In, Sc). *Phys. Rev. B* **2016**, *93* (16), 161116.

(9) O. El Rhazouani, A. Benyoussef, Z. Zarhri, A. El Kenz. Antisite Disorder Study by Monte Carlo Simulation of the Double Perovskite Sr_2CrReO_6. *Journal of Magnetism and Magnetic Materials* **2016**, *401*, 897–901.

(10) H. Kato, T. Okuda, Y. Okimoto, Y. Tomioka, Y. Takenoya, A. Ohkubo, M. Kawasaki, Y. Tokura. Metallic Ordered Double-Perovskite Sr_2CrReO_6 with Maximal Curie Temperature of 635 K. *Appl. Phys. Lett.* **2002**, *81* (2), 328–330.

(11) Y. Krockenberger, K. Mogare, M. Reehuis, M. Tovar, M. Jansen, G. Vaitheeswaran, V. Kanchana, F. Bultmark, A. Delin, F. Wilhelm, A. Rogalev, A. Winkler, L. Alff. Sr_2CrOsO_6: End Point of a Spin-Polarized Metal-Insulator Transition by 5d Band Filling. *Phys. Rev. B* **2007**, *75* (2), 020404.

(12) Li Yang, Shuai Fu, Kai Leng, Qingkai Tang, Zhiwei Wu, Kang Yi, Xinhua Zhu. Crystal Structure and Magnetic Properties of Double Perovskite Sr_2FeReO_6 Ceramics Synthesized by a Combined Molten-Salt Synthesis and Solid-State Reaction Method. *Open Ceramics* **2022**, *9*, 100238.

(13) Avijit Kumar Paul, Manfred Reehuis, Vadim Ksenofontov, Binghai Yan, Andreas Hoser, Daniel M. Többens, Paula M. Abdala, Peter Adler, Martin Jansen, Claudia Felser. Lattice Instability and Competing Spin Structures in the Double Perovskite Insulator Sr_2FeOsO_6. *Phys Rev Lett* **2013**, *111* (16), 167205.

(14) W. Yi, A. J. Princep, Y. Guo, R. D. Johnson, D. Khalyavin, P. Manuel, A. Senyshyn, I. A. Presniakov, A. V. Sobolev, Y. Matsushita, M. Tanaka, A. A. Belik, A. T. Boothroyd. Sc_2NiMnO_6: A Double-Perovskite with a Magnetodielectric Response Driven by Multiple Magnetic Orders. *Inorg. Chem.* **2015**, *54* (16), 8012–8021.

(15) E. Granado, J. C. Cezar, C. Azimonte, J. Gopalakrishnan, K. Ramesha. Electronic Structure of Fe and Magnetism in the 3d/5d Double Perovskites Ca_2FeReO_6 and Ba_2FeReO_2. *Phys. Rev. B* **2019**, *99* (19), 195118.

(16) W. Prellier, V. Smolyaninova, Amlan Biswas, C. Galley, R. L. Greene, K. Ramesha, J. Gopalakrishnan. Properties of the Ferrimagnetic Double Perovskites A_2FeReO_6 (A = Ba and Ca). *J. Phys.: Condens. Matter* **2000**, *12* (6), 965.

(17) Hariharan Nhalil, Harikrishnan S. Nair, C. M. N. Kumar, André M. Strydom, Suja Elizabeth. Ferromagnetism and the Effect of Free Charge Carriers on Electric Polarization in the Double Perovskite Y_2NiMnO_6. *Phys. Rev. B* **2015**, *92* (21), 214426.

(18) L. Hao, L. Yang, M. H. Lee, T. Lin, Z. Zhang, X. Xie, H. Zhu. Layered B-Site Cation Ordering: A Key Factor in Ferrimagnetism of Y_2MnCrO_6. *Journal of Alloys and Compounds* **2014**, *601*, 14–18.

(19) J. Blasco, J. García, G. Subías, J. Stankiewicz, J. A. Rodríguez-Velamazán, C. Ritter, J. L. García-Muñoz, F. Fauth. Magnetoelectric and Structural Properties of Y_2CoMnO_6: The Role of Antisite Defects. *Phys. Rev. B* **2016**, *93* (21), 214401.

(20) Q Zhao, Min Liu, J Dai, H Deng, Y Yin, L Zhou, J Yang, Z Hu, S Agrestini, K Chen, E Pellegrin, M Valvidares, L Nataf, F Baudelet, L. H. Tjeng, Y Yang, C Jin, Y Long. High-Pressure Synthesis and Ferrimagnetic Ordering of the B-Site-Ordered Cubic Perovskite Pb_2FeOsO_6. *Inorg. Chem.* **2016**, *55* (19), 9816–9821.

(21) K. Ramesha, L. Sebastian, B. Eichhorn, J. Gopalakrishnan. Pb_2FeReO_6: New Defect Pyrochlore Oxide with a Geometrically Frustrated Fe/Re Sublattice. *J. Mater. Chem.* **2003**, *13* (8), 2011–2014.

(22) M. Retuerto, M. Li, P. W. Stephens, J. Sánchez-Benítez, X. Deng, Gabriel Kotliar, Mark C. Croft, Alexander Ignatov, David Walker, Martha Greenblatt. Half-Metallicity in Pb_2CoReO_6 Double Perovskite and High Magnetic Ordering Temperature in Pb_2CrReO_6 Perovskite. *Chem. Mater.* **2015**, *27* (12), 4450–4458.

(23) R. Morrow, K. Samanta, T. Saha D., J. Xiong, J. W. Freeland, D. Haskel, P. M. Woodward. Magnetism in Ca_2CoOsO_6 and Ca_2NiOsO_6: Unraveling the Mystery of Superexchange Interactions between 3d and 5d Ions. *Chem. Mater.* **2016**, *28* (11), 3666–3675.

(24) C. E. Frank, E. E. McCabe, F. Orlandi, P. Manuel, X. Tan, Z. Deng, M. Croft, V. Cascos, T. Emge, H. Feng, S. Lapidus, C. Jin, M. Wu, M. Li, S. Ehrlich, S. Khalid, N. Quackenbush, S. Yu, D. Walker, M. Greenblatt. Mn_2CoReO_6: A Robust Multisublattice Antiferromagnetic Perovskite with Small A-Site Cations. *Chem. Commun.* **2019**, *55* (23), 3331–3334.

(25) E. Solana.M., K. N. Alharbi, M. Herz, P. Manuel, J. P. Attfield. Unconventional Magnetism in the High Pressure 'All Transition Metal' Double Perovskite Mn_2NiReO_6. *Chem. Commun.* **2020**, *56* (83), 12574–12577.

(26) E. Solana-Madruga, C. Ritter, O. Mentré, J. P. Attfield, Á. M. Arévalo-López. Giant Coercivity and Spin Clusters in High Pressure Polymorphs of Mn_2LiReO_6. *J. Mater. Chem. C* **2022**, *10* (11), 4336–4341.

(27) Abhijit S. Ogale, S. B. Ogale, R. Ramesh, T. Venkatesan. Octahedral Cation Site Disorder Effects on Magnetization in Double-Perovskite Sr_2FeMoO_6: Monte Carlo Simulation Study. *Appl. Phys. Lett.* **1999**, *75* (4), 537–539.

(28) D. Sánchez, J. A. Alonso, M. García-Hernández, M. J. Martínez-Lope, J. L. Martínez, Anders Mellergård. Origin of Neutron Magnetic Scattering in Antisite-Disordered Sr_2FeMoO_6 Double Perovskites. *Phys. Rev. B* **2002**, *65* (10), 104426.

(29) Hai L. Feng, Madhav Prasad Ghimire, Zhiwei Hu, Sheng-Chieh Liao, Stefano Agrestini, Jie Chen, Yahua Yuan, Yoshitaka Matsushita, Yoshihiro Tsujimoto, Yoshio Katsuya, Masahiko Tanaka, Hong-Ji Lin, Chien-Te Chen, Shih-Chang Weng, Manuel Valvidares, Kai Chen, Francois Baudelet, Arata Tanaka, Martha Greenblatt, Liu Hao Tjeng, Kazunari Yamaura. Room-Temperature Ferrimagnetism of Anti-Site-Disordered Ca_2MnOsO_6. *Phys. Rev. Materials* **2019**, *3* (12), 124404.

(30) Marina R. Filip, Feliciano Giustino. The Geometric Blueprint of Perovskites. *Proceedings of the National Academy of Sciences* **2018**, *115* (21), 5397–5402.

(31) Learning Chemistry Transition Metals - Elements, Definition, List, Properties. *Learning Chemistry*, 2021.

(32) B. Zwartsenberg, R. P. Day, E. Razzoli, M. Michiardi, N. Xu, M. Shi, J. D. Denlinger, G. Cao, S. Calder, K. Ueda, J. Bertinshaw, H. Takagi, B. J. Kim, I. S. Elfimov, A. Damascelli. Spin-Orbit-Controlled Metal–Insulator Transition in Sr_2IrO_4. *Nature Physics* **2020**, *16* (3), 290–294.

(33) Shuntaro Sumita, Takuya Nomoto, Youichi Yanase. Multipole Superconductivity in Nonsymmorphic Sr_2IrO_4. *Phys. Rev. Lett.* **2017**, *119* (2), 027001.

(34) Atsuo Shitade, Hosho Katsura, Jan Kunes, Xiao-Liang Qi, Shou-Cheng Zhang, Naoto Nagaosa. Quantum Spin Hall Effect in a Transition Metal Oxide Na_2IrO_3. *Phys. Rev. Lett.* **2009**, *102* (25), 256403.

(35) Xiangang Wan, Ari M. Turner, Ashvin Vishwanath, Sergey Y. Savrasov. Topological Semimetal and Fermi-Arc Surface States in the Electronic Structure of Pyrochlore Iridates. *Phys. Rev. B* **2011**, *83* (20), 205101.

(36) William Witczak-Krempa, Gang Chen, Yong Baek Kim, Leon Balents. Correlated Quantum Phenomena in the Strong Spin-Orbit Regime. *Annual Review of Condensed Matter Physics* **2014**, *5* (1), 57–82.

(37) Yunlong Geng. Microstructure and Magnetic Behavior Studies of Processing-Controlled and Composition-Modified Fe-Ni and Mn-Al Alloys. **2014**.

(38) Wu Hai-Ping, Deng Kai-Ming, Tan Wei-Shi, Xiao Chuan-Yun, Hu Feng-Lan, Li Qun-Xiang. The Structural, Electronic, and Magnetic Properties of SrFeOn (n = 2 and 2.5): A GGA+U Study. *Chinese Phys. B* **2009**, *18* (11), 5008.

(39) H. A Kramers L'interaction Entre les Atomes Magnétogènes dans un Cristal. Paramagnétique. *Physica* **1934**, *1* (1), 182–192.

(40) Anthony R. West. *Solid State Chemistry and Its Applications*; John Wiley & Sons, 2014.

(41) P. W. Anderson Antiferromagnetism. Theory of Superexchange Interaction. *Phys. Rev.* **1950**, *79* (2), 350–356.

(42) John B. Goodenough. Theory of the Role of Covalence in the Perovskite-Type Manganites [La, M(II)]MnO_3. *Phys. Rev.* **1955**, *100* (2), 564–573.

(43) G. H. Jonker, J. H. Van Santen. Ferromagnetic Compounds of Manganese with Perovskite Structure. *Physica* **1950**, *16* (3), 337–349.

(44) Clarence Zener. Interaction between the D-Shells in the Transition Metals. II. Ferromagnetic Compounds of Manganese with Perovskite Structure. *Phys. Rev.* **1951**, *82* (3), 403–405.

(45) C. Zener. Interaction Between the d Shells in the Transition Metals. *Phys. Rev.* **1951**, *81* (3), 440–444.

(46) Elbio Dagotto, Takashi Hotta, Adriana Moreo. Colossal Magnetoresistant Materials: The Key Role of Phase Separation. *Physics Reports* **2001**, *344* (1), 1–153.

(47) Leon Balents. Spin Liquids in Frustrated Magnets. *Nature* **2010**, *464* (7286), 199–208.

(48) A. P. Ramirez. Geometric Frustration: Magic Moments. *Nature* **2003**, *421* (6922), 483–483.

(49) Bin Hu, Yue Wu. Tuning Magnetoresistance between Positive and Negative Values in Organic Semiconductors. *Nature Materials* **2007**, *6* (12), 985–991.

(50) Ioanna Giouroudi, Franz Keplinger Microfluidic. Biosensing Systems Using Magnetic Nanoparticles. *Int J Mol Sci* **2013**, *14* (9), 18535–18556.

(51) M. N. Baibich, J. M. Broto, A. Fert, F. Nguyen Van Dau, F. Petroff, P. Etienne, G. Creuzet, A. Friederich, J. Chazelas. Giant Magnetoresistance of (001)Fe/(001)Cr Magnetic Superlattices. *Phys. Rev. Lett.* **1988**, *61* (21), 2472–2475.

(52) Elby Titus, Rahul Krishna, José Grácio, Manoj Singh, Antonio Luis Ferreira, Ricardo G. Dias, *Carbon Nanotube Based Magnetic Tunnel Junctions (MTJs) for Spintronics Application*; IntechOpen, 2011.

(53) K.-I. Kobayashi, T. Kimura, Y. Tomioka, H. Sawada, K. Terakura, Y. Tokura. Intergrain Tunneling Magnetoresistance in Polycrystals of the Ordered Double Perovskite Sr_2FeReO_6. *Phys. Rev. B* **1999**, *59* (17), 11159–11162.

(54) S. Jin, T. H. Tiefel, M. McCormack, R. A. Fastnacht, R. Ramesh, L. H. Chen. Thousandfold Change in Resistivity in Magnetoresistive La-Ca-Mn-O Films. *Science* **1994**.

(55) R. L. Stamps. Mechanisms for Exchange Bias. *J. Phys. D: Appl. Phys.* **2000**, *33* (23), R247.

(56) Ajaya K. Nayak, Michael Nicklas, Stanislav Chadov, Panchanana Khuntia, Chandra Shekhar, Adel Kalache, Michael Baenitz, Yurii Skourski, Veerendra K. Guduru, Alessandro Puri, Uli Zeitler, J. M. D. Coey, Claudia Felser. Design of Compensated Ferrimagnetic Heusler Alloys for Giant Tunable Exchange Bias. *Nature Mater* **2015**, *14* (7), 679–684.

(57) H. Feng, P. Adler, M. Reehuis, W. Schnelle, P. Pattison, Andreas Hoser, Claudia Felser, Martin Jansen. High-Temperature Ferrimagnetism with Large Coercivity and Exchange Bias in the Partially Ordered 3d/5d Hexagonal Perovskite $Ba_2Fe_{1.12}Os_{0.88}O_6$. *Chem. Mater.* **2017**, *29* (2), 886–895.

(58) Amrozia Shaheen. *Band Structure and Electrical Conductivity in Semiconductors*; 2010.

(59) L. J. Huijbregts Charge. Transport and Morphology in Nanofillers and Polymer Nanocomposites. **2008**.

(60) N. F. Mott. Conduction in Glasses Containing Transition Metal Ions. *Journal of Non-Crystalline Solids* **1968**, *1* (1), 1–17.

(61) Ju-Jin Kim, Hu Jong Lee. Observation of a Nonmagnetic Hard Gap in Amorphous In/InO_x Films in the Hopping Regime Films in the Hopping Regime. *Phys. Rev. Lett.* **1993**, *70* (18), 2798–2801.

(62) A. L. Efros, B. I. Shklovskii. Coulomb Gap and Low Temperature Conductivity of Disordered Systems. *J. Phys. C: Solid State Phys.* **1975**, *8* (4), L49.

(63) H Scher, M Lax Continuous Time Random Walk. Model of Hopping Transport: Application to Impurity Conduction. *Journal of Non-Crystalline Solids* **1972**, *8–10*, 497–504.

(64) T. T. Lin, S. L. Young, C. Y. Kung, H. Z. Chen, M. C. Kao, M. C. Chang, C. R. Ou. Variable-Range Hopping and Thermal Activation Conduction of Y-Doped ZnO Nanocrystalline Films. *IEEE Transactions on Nanotechnology* **2014**, *13* (3), 425–430.

(65) A. Katrusiak. Lab in a DAC – High-Pressure Crystal Chemistry in a Diamond-Anvil Cell. *Acta Cryst B* **2019**, *75* (6), 918–926.

(66) James S. Schilling. The Use of High Pressure in Basic and Materials Science. *Journal of Physics and Chemistry of Solids* **1998**, *59* (4), 553–568.

(67) Y. Shi, Y. Guo, X. Wang, A. J. Princep, D. Khalyavin, P. Manuel, Y. Michiue, A. Sato, K. Tsuda, S. Yu, M. Arai, Y. Shirako, M. Akaogi, N. Wang, K. Yamaura, A. T. Boothroyd. A Ferroelectric-like Structural Transition in a Metal. *Nature Materials* **2013**, *12* (11), 1024–1027.

(68) A. A. Belik, Eiji Takayama-Muromachi. $Bi_3Mn_3O_{11}$: A New $KSbO_3$-Type Random Ferrimagnet with High T_c. *J. Am. Chem. Soc.* **2009**, *131* (27), 9504–9505.

(69) Paul F. McMillan. New Materials from High-Pressure Experiments. *Nature Materials* **2002**, *1* (1), 19–25.

(70) K.-I. Kobayashi, T. Kimura, H. Sawada, K. Terakura, Y. Tokura. Room-Temperature Magnetoresistance in an Oxide Material with an Ordered Double-Perovskite Structure. *Nature* **1998**, *395* (6703), 677–680.

(71) D. Serrate, J. M. De Teresa, M. R. Ibarra. Double Perovskites with Ferromagnetism above Room Temperature. *J. Phys.: Condens. Matter* **2006**, *19* (2), 023201.

(72) Mark T. Anderson, Kevin B. Greenwood, Gregg A. Taylor, Kenneth R. Poeppelmeier. B-Cation Arrangements in Double Perovskites. *Progress in Solid State Chemistry* **1993**, *22* (3), 197–233.

(73) M. Li, M. Retuerto, Z. Deng, P. W. Stephens, M. Croft, Q. Huang, H. Wu, X. Deng, G. Kotliar, J. Sánchez-Benítez, J. Hadermann, D. Walker, M. Greenblatt. Giant Magnetoresistance in the Half-Metallic Double-Perovskite Ferrimagnet Mn_2FeReO_6. *Angewandte Chemie International Edition* **2015**, *54* (41), 12069–12073.

(74) Ikuya Yamada, Akihiko Takamatsu, Naoaki Hayashi, Hidekazu Ikeno. Covalency Competition in the Quadruple Perovskite $CdCu_3Fe_4O_{12}$. *Inorg. Chem.* **2017**, *56* (15), 9303–9310.

(75) Geneva Laurita, Daniel Hickox-Young, Samra Husremovic, Jun Li, Arthur W. Sleight, Robin Macaluso, James M. Rondinelli, Mas A. Subramanian. Covalency-Driven

Structural Evolution in the Polar Pyrochlore Series $Cd_2Nb_2O_{7-x}$. *Chem. Mater.* **2019**, *31* (18), 7626–7637.

(76) Brendan J. Kennedy, Qingdi Zhou, Maxim Avdeev. The Ferroelectric Phase of $CdTiO_3$: A Powder Neutron Diffraction Study. *Journal of Solid State Chemistry* **2011**, *184* (11), 2987–2993.

(77) Akihisa Aimi, Daisuke Mori, Ko-ichi Hiraki, Toshihiro Takahashi, Yue Jin Shan, Yuichi Shirako, Jianshi Zhou, Yoshiyuki Inaguma. High-Pressure Synthesis of *A* -Site Ordered Double Perovskite $CaMnTi_2O_6$ and Ferroelectricity Driven by Coupling of *A* -Site Ordering and the Second-Order Jahn–Teller Effect. *Chem. Mater.* **2014**, *26* (8), 2601–2608.

(78) Man-Rong Li, Maria Retuerto, Zheng Deng, Peter W. Stephens, Mark Croft, Qingzhen Huang, Hui Wu, Xiaoyu Deng, Gabriel Kotliar, Javier Sánchez-Benítez, Joke Hadermann, David Walker, Martha Greenblatt. Giant Magnetoresistance in the Half-Metallic Double-Perovskite Ferrimagnet Mn2FeReO6. *Angewandte Chemie International Edition* **2015**, *54* (41), 12069–12073.

(79) Nicola A. Hill. Why Are There so Few Magnetic Ferroelectrics? *J. Phys. Chem. B* **2000**, *104* (29), 6694–6709.

(80) Qingsong Zhang, Tahir Cagin, William A. Goddard. The Ferroelectric and Cubic Phases in $BaTiO_3$ Ferroelectrics Are Also Antiferroelectric. *Proceedings of the National Academy of Sciences* **2006**, *103* (40), 14695–14700.

Chapter 2. Experimental methods

As mentioned in last chapter, pressure is an essential variable in materials science and the high-pressure method allows for the efficient synthesis of materials and facilitates the formation of ordered crystal structures. Hence, high-pressure synthesis methods and two different high-pressure apparatus: Belt-type and Multi-Anvil-type high-pressure machines were used in this thesis. Crystal structures, magnetic and electrical transport properties as well as some other physical properties were investigated using some basic physical property measurement devices such as X-ray diffraction (XRD), magnetic property measurement system (MPMS 3), and physical property measurement system (PPMS).

2.1. Sample preparation

In this thesis, all samples were prepared according to the following steps: i) Dry the chemicals used as raw materials in the experiments at 120 °C for few hours, ii) stoichiometric amounts of powder were weighted and mixed using a mortar in an Ar-filled glove box, iii) fill the Pt or Au capsule with the mixed powders, compact the powders and finally seal the capsule. After completing the above processes, the samples will be inserted to the pyrophyllite cell to produce a quasihydrostatic condition under the pressure caused by the high-pressure apparatus. Different high-pressure machines correspond to different sample assemble methods, which I will describe in detail in the following section.

2.2. High-pressure synthesis apparatus

In my work, two different types of instruments were used, involving the Belt-type machine and Multi-Anvil-type high-pressure machine. I will then describe them in detail.

2.2.1. Belt-type high pressure apparatus (Kobe Steel, Ltd.)

The Belt-type high-pressure machine could reach static pressures up to 6 GPa, an electrical heating system is concluded in the machine and the max temperature it can reach is around 2000°C. Simultaneous high temperature heating processes at constant pressure can be achieved in this equipment. **Figure 2.1** shows the photograph, operating schematic and sample assembly diagram of the Belt-type high-pressure apparatus [1]. As shown on the left, the temperature control section and the pressure control section are independent from each other and can work in synergy to achieve simultaneous high temperature and high-pressure conditions. In the middle is the diagram of its working mechanism, the main part of the apparatus consists of a fixed cylinder and two anvils that could be moved up and down freely. During the experiment, the upper and lower anvils are compressed against each other together to obtain the target pressure. On the right is an illustration of the sample assembly, a pyrophyllite cell is used as the pressure transmitting medium and electrical as well as thermal insulation. The above-mentioned samples which are sealed in the Au/Pt capsules are placed in this cell, wrapped with the mixture of NaCl and ZrO_2. During the experiments, the target temperature was achieved by heating the flake graphite with an electric current.

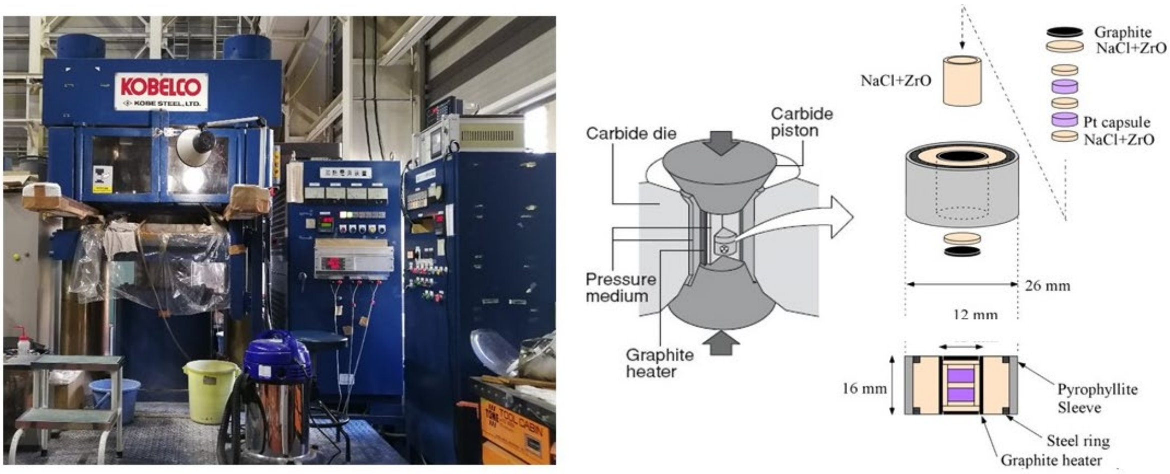

Figure 2.1 The photograph, operating schematic and sample assembly diagram of the Belt-type high-pressure apparatus at National Institute for Materials Science (NIMS) [1]

2.2.2. Multi-Anvil-type high-pressure apparatus (CTF-MA1500P, C&T Factory Co., Ltd, Japan)

Besides the Belt-type high-pressure machine, another Multi-Anvil-type apparatus is also utilized in my work to obtain part of samples. This machine could offer a high pressure up to 6 GPa and high temperatures up to 1800 °C. Unlike the above-mentioned Belt-type apparatus, the Multi-Anvil machine contains six anvils and establishes a cubic compression space. Therefore, the pyrophyllite cell used corresponding to this machine is cubic. **Figure 2.2** gives a schematic of the assembly of the sample and a photograph of the Multi-Anvil-type high-pressure machine. Another significant difference between them is that, in Multi-Anvil-type machine, a thermal couple could be inserted in the cell thus the temperature could be controlled accurately in this situation. Except the shape of the pyrophyllite cell and the anvils as well as the addition of the thermal couple, the basic procedure and mechanism of the Multi-Anvil-type high-pressure machine are almost the same as the Belt-type apparatus.

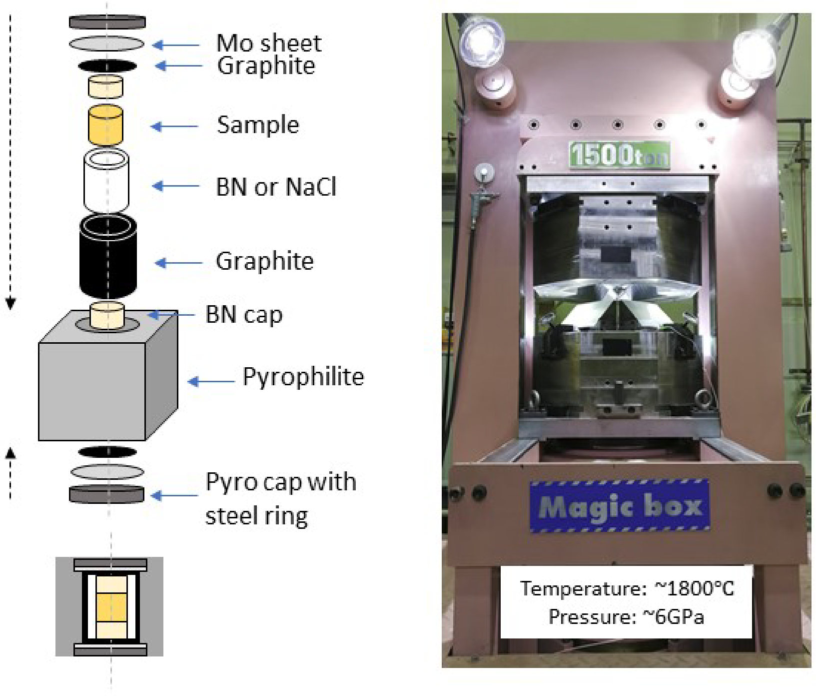

Cubic anvil cell set

Multi-Anvil high-pressure apparatus

Figure 2.2 A schematic of the assembly of the sample and a photograph of the Multi-Anvil-type high-pressure machine in NIMS.

2.3. Structural characterization methods

The structure of a substance largely determines and influences the properties of the substance, the structural study is therefore particularly important. The X-ray diffraction (XRD) measurement is a very effective method for studying structural information of materials [2]. In this thesis, two main XRD methods were applied and the details will be illustrated in the following sections.

2.3.1. Laboratory powder X-ray diffraction

The laboratory powder X-ray diffraction (XRD) is convenient to be utilized to preliminarily identify the phase and structure of unknown materials. In this work, room temperature XRD data collection was performed using a Desktop X-ray Diffractometer MiniFlex (Rigaku) (**Figure 2.4**), which equipped with a graphite monochromator and Cu K_α radiation (λ = 1.5418 Å). In the measurements, the increment is 0.2° and the scanning range is $5° < 2\theta < 120°$ with a scanning rate of 1°/min.

Figure 2.4 The photo of the X-ray Diffractometer MiniFlex (Rigaku)

2.3.2. Synchrotron X-ray diffraction

In general, conventional laboratory X-rays are produced by electrons which are accelerated by high voltage, these accelerated high-energy electrons then bombard metal targets (such as Cu, Mo, etc.) and generate characteristic radiation which could be used for structural characterization. It is formed by the jump of electrons from the high energy level outer shell to the low energy level inner shell within the atom and therefore the characterization energy is definite and fixed. For example, by bombarding a copper target with high energy X-rays, multiple characteristic X-ray wavelengths will be produced, and the main X-rays I use are $K_{\alpha 1}$ 1.54056 Å and $K_{\alpha 2}$ 1.54439 Å produced by electrons jumping from *L* layer to *K* layer.

Different from the traditional laboratory X-ray generation mechanism, the principle of synchrotron radiation is that, when electrons moving curved with a rate close to the speed of light in a magnetic field, electromagnetic waves will be radiated in the tangential direction.

This phenomenon was first discovered by Pollack et al [3] in the General Electric 70-Mev synchrotron in 1947 and then it was named “synchrotron radiation”.

Since the 1960s, the synchrotron radiation had undergone three technical update iterations: from the 1970s, the synchrotron radiation was generated from the synchrotron, known as the first-generation synchrotron radiation source; from the 1980s, people began to develop accelerators which could help electrons make more curved motions in the magnetic field by setting some inserts on the path of electron acceleration, therefore the stronger electromagnetic waves could be generated, this is the second-generation synchrotron radiation source. After the 1990s, more inserts were added into the electron motion path, dramatically increased (nearly 1000 times) the intensity of the synchrotron radiation, known as the third generation of synchrotron radiation, represented by Spring 8, Japan. The fourth-generation synchrotron radiation will be developed toward the following directions: new laser source with ultra-high brightness and phase coherence; energy recover linear accelerator; synchrotron storage ring, the targets are to achieve stronger light intensity and the coherence of the light source.

In a word, compared with the laboratory powder X-ray diffraction, synchrotron X-ray could provide higher resolution since the synchrotron X-ray is emitted when charged particles such as electrons are accelerated and circulated in ultra-high vacuum tubes or storage rings, as briefly sketched in **Figure 2.5** [2]. Thereby, the synchrotron X-ray beams are extremely parallel and the obtained intensity is extraordinarily high.

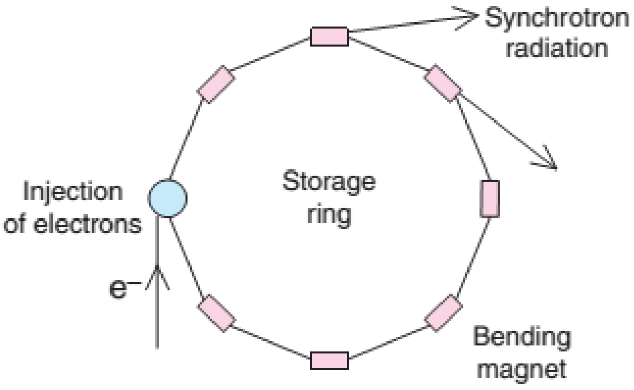

Figure 2.5 A briefly diagram of a synchrotron storage ring. [2]

In my work, high-resolution synchrotron XRD data were obtained at room temperature using monochromatized beams at beamline BL02B2 (**Figure 2.6**) at SPring-8, Japan. [4,5] Prior to the measurements, a benchmark test was performed using a standard (CeO_2)

to confirm the wavelength. The powders were placed in Lindenmann glass capillaries (0.1 mm inner diameter) and rotated during measurements. The RIETAN-VENUS program was used to analyze the synchrotron XRD patterns. [6,7]

Figure 2.6 A picture of the BL02B2 beamline in Spring-8.

2.3.3. Rietveld method

In the structural analysis of materials, a big challenge is the difficulty of obtaining single crystals with large size. In fact, it is more common for researchers to obtain polycrystalline materials. However, in polycrystalline samples a lot of information may be missed due to the random orientation of grains and the overlap between individual diffraction peaks. In order to solve this problem, in 1967, the Dutch scientist Hugo. M. Rietveld first proposed a method to refine the crystal structure by fitting the entire neutron powder diffraction pattern, such as the peak position, intensity, line shape and so on, which became known as the "Rietveld method" after that [8]. In 1977, Malmros and Thomas first extended this method in the region of powder X-ray diffraction refinement [9]. The basic idea of the Rietveld method is to calculate a theoretical polycrystalline diffraction spectrum from an initial crystal structure model using a series of crystal structure parameters, then compare this theoretical fitted spectrum with the experimentally measured diffraction spectrum point by point through a computer program as well as adjust various parameters (including 1: crystal structure parameters: lattice constants, atomic occupancy ratios, thermal factors; 2: diffraction peak shape parameters: shape function, peak asymmetry parameters, peak half-height width, etc; 3: experimental conditions: X-ray wavelength, zero point, background and so on; 4: other parameters: grain size, orientation, microscopic stress and so on) using the least squares method continuously to optimize the model and finally obtain a calculated peak shape which could match the experimental results well.

The determination of the crystal structure from the powder polycrystalline X-ray diffraction spectra is usually carried out as following steps: first, to obtain a high quality powder polycrystalline X-ray diffraction spectrum; second, to index the main peak positions and then confirm the space group and lattice constants; third, to choose a known model which is similar to the undetermined compound as the prototype and then use the Rietveld-method to optimize the calculated spectrum and obtain the exact crystal structure parameters. The optimization process is roughly in the following order: first, the zero-point shift should be adjusted, then the background, later the cell parameters and the scale factor are corrected. Second, optimize the peak shape function, Gaussian peak shape function and half-height width parameters U, V, W as well as the peak shape asymmetry parameters. Finally, modify the atomic positions, occupancy factors, thermal factors and so on.

2.3.4. Rietveld program: RIETAN

With the enhanced improvements in XRD refinement technology, various types of advanced XRD refinement software have been developed, such as GSAS, FULLPROF, TOPAS, EXPO, RIETAN and so on. In this work, I use the RIETAN program to realize the crystal structure refinement.

Compared with the traditional Rietveld refinement method, RIETAN has achieved a significant breakthrough, that is, RIETAN offers a state-of-the-art structure refinement technique: the Maximum entropy method-based Pattern Fitting (MPF) to replace the classical Rietveld method. The advantage is that the whole pattern fitting and Maximum entropy method analysis were repeated alternately in an iterative process called REMEDY cycles. In this process, the structural model could always cause a minimal deviation from the final electron/nucleus density.

Usually, four confidence factors can be defined to evaluate the credibility of the refinement results: the diffraction pattern *R* factor *R*p, the diffraction weight pattern *R* factor

Rwp, the Bragg factor R_B and goodness-of-fit indicator χ^2. In general, the agreement between the fitted and experimental spectra is reflected in Rp and Rwp, the agreement between the calculated and measured diffraction peaks is reflected in R_B. The smaller the R values, the better the fit and the greater probability that the resolved crystal structure is correct. It is generally accepted that both Rp and Rwp are lower than 10% and χ^2 exceeds 90%. In RIETAN program, such reliable indices were also defined to judge the agreement between experimental results and theoretical calculated intensities. The definitions of these R values are illustrated in detail by Izumi and Momma [6,7].

2.4. Magnetic property measurement

The temperature dependence of the direct current (DC) and alternating current (AC) magnetic susceptibilities could be measured using a magnetometer (MPMS3, Quantum Design Inc, San Diego, California, as shown in **Figure 2.7**) at temperatures between 2 K and 600 K under zero-field cooling (ZFC) and magnetic field cooling (FC) conditions. Isothermal magnetization curves could be measured between the -70 to 70 kOe field range.

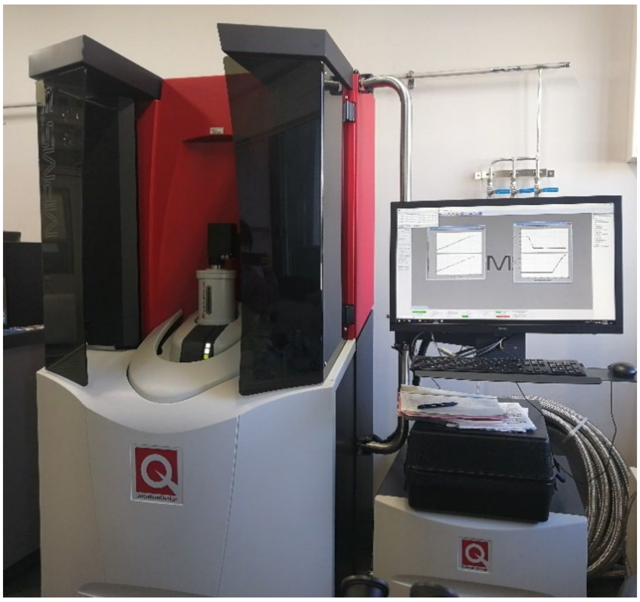

Figure 2.7 Photo of MPMS3 in NIMS Namiki-site.

2.5. Electrical property measurement

Electrical-transport properties could be recorded using a four-probe method between 2 K and 400 K in magnetic fields up to 90 kOe using a physical property measurement system (PPMS, Quantum Design), as shown in **Figure 2.8**. During the measurements, silver paste and gold wires (30μm in diameter) were used to connect the pellets and the device terminals. The magnetoresistance (MR) which can be defined as $\mathrm{MR}(H) = 100\times[R(H)–R(0)]/R(0)$ could be also measured in PPMS by adding an applied magnetic field with a range of -90 kOe to 90 kOe as well.

Figure 2.8 Photo of the PPMS-9T in NIMS Namiki-site.

2.6. Thermal property measurement

The specific heat (C_p), which can provide some information such as phase transition point, could be measured by the relaxation method between 2 and 400 K in magnetic fields up to 90 kOe, using PPMS as well. During the measurements, a dense pellet of the sample needs to be assembled on an aluminum plate using grease (N Apiezon) to ensure a good thermal contact.

2.7. Other technologies used in this work

2.7.1. Electron probe microanalysis (EPMA)

The electron probe microanalysis is an analytical tool which is very useful for the non-destructive determination of the chemical composition of small quantities of solid materials. Its working principle is very similar with the scanning electron microscopy, that is, the sample is bombarded with an electron beam then characteristic X-rays of the undetermined elements will be emitted. Then the elements contained in the sample could be defined by analysis of these characteristic X-rays. Another advantage is that, this technique requires only a very small amount of sample (typically 10~30 cubic microns or less) to determine the abundance elements present in the sample.

To determine the exact metal composition of the high-pressure products, electron probe microanalysis (EPMA) was performed using a JEOL JXA-8500F instrument, as shown in **Figure 2.9** [10]**.** The sintered surfaces were precisely polished with a 0.3μm alumina-coated film.

Figure 2.9. EPMA, JEOL JXA-8500F instrument in NIMS. [10]

2.7.2. Mössbauer spectroscopy

Mössbauer spectroscopy is a technique widely used in fields of physics, metallurgy, mineralogy, biology, material science and so on to examine the valence state of iron, such as Fe^0, Fe^{2+} and Fe^{3+}, and the type of coordination polyhedron occupied by iron atoms, such as trigonal, tetrahedral and so on.

Essentially, Mössbauer spectroscopy is based on the recoilless emission and the resonant absorption of gamma radiation by atomic nuclei. Two nuclei are needed to observe the Mössbauer effect. The source nucleus is used to emit γ photon and the absorber is used to absorb γ photon. During this process, since the nuclei are usually surrounded by the atomic electron clouds, the Coulomb interactions between the electron clouds and the proton charge distribution within the nucleus may result a shift or split of the nuclear levels, by analyzing these shifts and splits, the determination of the electronic states is possible to realize. [11]

References in Chapter 2

(1) Dudu Nkomo, Alain Mwamba. Beneficiation Opportunities for Osmium: A Review. *IOP Conference Series: Materials Science and Engineering* **2020**, *839*, 012014.

(2) Anthony R. West *Solid State Chemistry and Its Applications*; John Wiley & Sons, 2014.

(3) F. R. Elder, A. M. Gurewitsch, R. V. Langmuir, H. C. Pollock. Radiation from Electrons in a Synchrotron. *Phys. Rev.* **1947**, *71* (11), 829–830.

(4) M. Tanaka, Y. Katsuya, A. Yamamoto. A New Large Radius Imaging Plate Camera for High-Resolution and High-Throughput Synchrotron X-Ray Powder Diffraction by Multiexposure Method. *Review of Scientific Instruments* **2008**, *79* (7), 075106.

(5) M. Tanaka, Y. Katsuya, Y. Matsushita, O. Sakata. Development of a Synchrotron Powder Diffractometer with a One-Dimensional X-Ray Detector for Analysis of Advanced Materials. *Journal of the Ceramic Society of Japan* **2013**, *121* (1411), 287–290.

(6) F. Izumi, K. Momma. Three-Dimensional Visualization in Powder Diffraction. *Solid State Phenomena* **2007**, *130*, 15–20.

(7) K. Momma, F. Izumi. VESTA: A Three-Dimensional Visualization System for Electronic and Structural Analysis. *J Appl Cryst* **2008**, *41* (3), 653–658.

(8) H. M. Rietveld. A Profile Refinement Method for Nuclear and Magnetic Structures. *J Appl Cryst* **1969**, *2* (2), 65–71.

(9) G. Malmros, J. O. Thomas. Least-Squares Structure Refinement Based on Profile Analysis of Powder Film Intensity Data Measured on an Automatic Microdensitometer. *Journal of Applied Crystallography* **1977**, *10* (1), 7–11.

(10) ENGLISH | ARIM Japan 公式ホームページ_マテリアル先端リサーチインフラ https://nanonet.mext.go.jp/page/dir000011.html (accessed Jan 23, 2023).

(11) Saburo Nasu General. Introduction to Mössbauer Spectroscopy. In *Mössbauer Spectroscopy: Tutorial Book*; Yoshida, Y., Langouche, G., Eds.; Springer: Berlin, Heidelberg, 2013; pp 1–22.

Chapter 3 High-pressure synthesis and magnetic and electrical properties of Double Perovskite Oxides Cd_2FeOsO_6 and Cd_2FeReO_6

3.1. Achieving large exchange bias effect in Cd_2FeOsO_6 with small cooling fields

3.1.1. Introduction

With the advent of the information age, research on data access is driving global technological innovation. In magnetic recording devices, the EB effect plays a crucial role in accurately determining the state of the readout head in hard disk drives. The EB effect typically occurs at the interface between two or more layers of a magnetic material after cooling in a high cooling field (H_{cool}) (typically tens of kOe [1–3]) [4]. However, achieving high-quality interfaces with optimal performance poses technical challenges [5,6], and further advancements are hindered by the requirement for high cooling fields (H_{cool}). Therefore, there is a pressing need for the development of new material systems that exhibit huge EB effects with smaller H_{cool} values.

Recently, the giant EB effect has been observed in the Mn-Pt-Ga system [7]. This effect arises from the presence of ferromagnetic (FM) clusters embedded in a nearly compensated ferrimagnetic (FIM) host. The Mn-Pt-Ga system exhibits a remarkable giant EB effect of 30 kOe when cooled in a magnetic field of 100 kOe. However, the high H_{cool} required for this effect makes it unsuitable for practical applications. Consequently, there has been a search for new materials that can exhibit large EB effects with small H_{cool} values.

Subsequently, the EB effect was confirmed in quasi-2D perovskites and spin glass-related systems [1]. However, in most of these materials, only small EB fields of a few kOe were observed at low temperatures, following a large field cooling process. In 2019, a significant advancement was made with the discovery of a giant EB effect of 12 kOe in $Mn_{3.5}Co_{0.5}N$, a material with a canted triangular magnetic structure [8]. This effect was achieved with a small H_{cool} of only 500 Oe and remained present up to temperatures of approximately 250 K. This property represented the best performance at that time and served as a motivation for further exploration of new bulk materials exhibiting large EB effects with small H_{cool} values at higher temperatures [8].

Inspired by these, I have investigated double perovskite (DP) materials with different magnetic sublattices as promising candidates for achieving improved properties. In this study, I synthesized a new DP compound, Cd_2FeOsO_6, with the objective of obtaining excellent EB effects. My investigation revealed that this material exhibits FIM ordering and displays hard magnetism below 285 K. Most notably, I discovered a significant EB effect intertwined with a vertical magnetization shift (VMS), which has not been extensively explored previously. Remarkably, a small cooling field of only 80 Oe induced a substantial bias field of 10 kOe. Furthermore, I found that this phenomenon persists down to 260 K, approaching room temperature. The underlying mechanism is likely related to magnetic interactions occurring within the partially ordered host, which may be influenced by the strong spin-orbit coupling (SOC) of Os. The observation of such a pronounced EB effect in Cd_2FeOsO_6 opens up new possibilities for the development of advanced EB-effect materials with enhanced properties.

3.1.2. Experimental

Polycrystalline Cd_2FeOsO_6 was synthesized under high-pressure and high-temperature conditions. To prepare Cd_2FeOsO_6, powders of CdO (99.99%, Togawa Chemical), Fe_2O_3 (99.998%, Alfa Aesar), OsO_2 (laboratory-made from Os, 99.95%, Nanjing Dongrui Platinum Co. Ltd.), and $KClO_4$ (99.5%, Kishida Chem) in a stoichiometric ratio were mixed and sealed in a Pt capsule in an Ar-filled glove box. The capsule was then placed in a belt-type high-pressure apparatus and heated to 1500 °C for 1 hour under a pressure of 6 GPa. After heating, the capsule was rapidly cooled to room temperature, and the pressure was gradually released over a period of 40 minutes. To remove KCl, the sample was repeatedly washed with distilled water.

Synchrotron XRD data were collected at a wide temperature range (100-800 K) using a large Debye-Scherrer camera at beamline BL02B2 at SPring-8 [9,10]. Before the measurement, benchmark tests were performed using a standard material (CeO_2) to determine the actual wavelength. The sample was put into a Lindemann glass capillary (inner diameter: 0.1mm) and rotated during the measurement. The RIETAN-VENUS program [11,12] was used for the analysis of the synchrotron XRD patterns.

The temperature dependence of the DC magnetization in the range of 2-390 K under an applied magnetic field of 10 kOe and conditions of zero-field cooling (ZFC) and field cooling (FC) were measured using a magnetic property measurement system (MPMS3, Quantum Design Inc, San Diego, California). Isothermal magnetization curves were collected in the magnetic field range of -70 to 70 kOe. The magnetic transport properties were recorded by a four-probe method between 2 K and 400 K under magnetic fields up to 90 kOe using a physical property measurement system (PPMS, Quantum Design). The specific heat capacity (C_p) measurements were obtained by a relaxation method using the commercial calorimeter option of the PPMS.

The zero-field ^{57}Fe Mössbauer spectrum was measured at room temperature (287 K) using a Wissel MVT-1000 Mössbauer spectrometer, with a ^{57}Co/Rh source in transmission mode. The sample was uniformly dispersed with α-Al_2O_3 and enclosed in a small acrylic container to form a thin layer. The Mössbauer spectrum was calibrated at room temperature using α-Fe and analyzed using the MossA software package [13].

To determine the precise metal composition of the DP oxide, electron probe microanalysis (EPMA) was performed using a JEOL JXA-8500F instrument. The surface was polished with a 0.3 μm alumina-coated film.

3.1.3. Results and discussion

The crystal structure of Cd_2FeOsO_6 was investigated using synchrotron XRD techniques. The analysis revealed that the structure can be described by the space group $P2_1/n$, which is consistent with previous reports on B-site-ordered DP oxides. While a small amount of Os metal impurity (approximately 2.4 wt%) was detected instead of the expected Cd-Fe-O impurity identified by EPMA (see Supporting Information), the majority of the sample was confirmed to be a pure DP oxide.

The refined XRD pattern, presented in **Figure 3.1.**, provided detailed insights into the crystal structure of Cd_2FeOsO_6. In addition, in-situ synchrotron XRD measurements were performed in the temperature range of 100 K to 800 K to investigate potential structural transitions. The obtained results, shown in **Figure 3.2.**, revealed the absence of significant transitions within the measured temperature range. These findings highlight the structural stability of Cd_2FeOsO_6 over a wide temperature range, which further supports its potential for diverse applications in various fields.

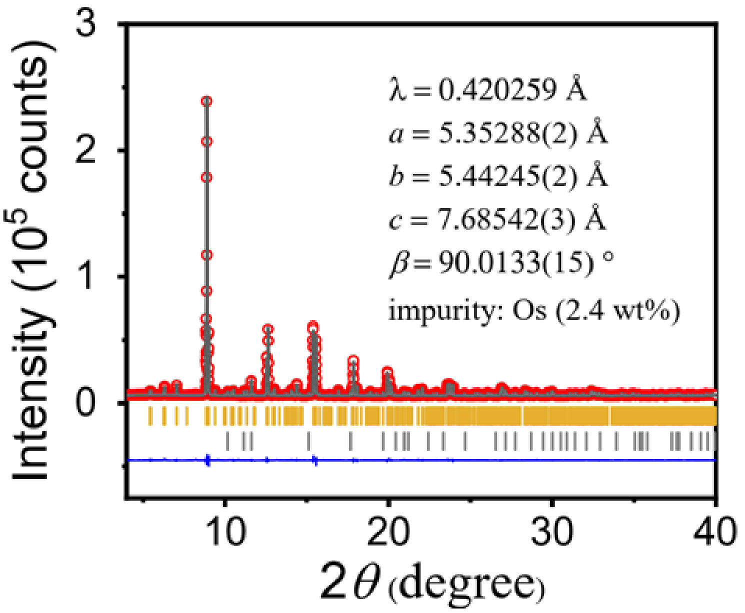

Figure 3.1: Refined synchrotron XRD pattern of Cd_2FeOsO_6 with Os at room temperature (296-300 K). The panel presents the observed pattern (circles) and calculated pattern (solid lines), along with the difference profile at the bottom. The first array of short vertical bars represents the calculated positions of diffraction peaks based on the DP structural model. The second row shows the calculated positions of diffraction peaks based on impurities.

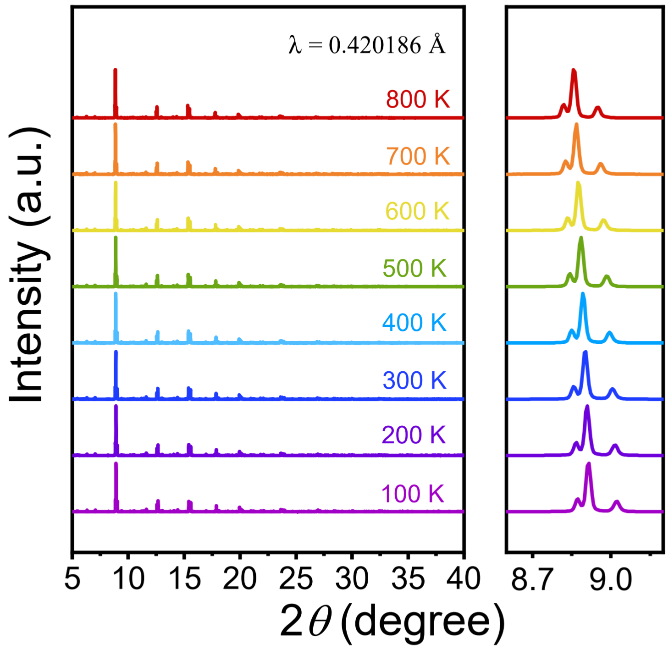

Figure 3.2. Synchrotron XRD patterns of Cd_2FeOsO_6 at different temperatures from 100 K to 800 K.

Through preliminary Rietveld refinements, it was found that Cd atoms fully occupy the 4*e*(*x*, *y*, *z*) Wyckoff position. In the space group $P2_1/n$, there exist two independent Fe and Os sites. The degree of B-site ordering can range from 0% (completely disordered) to 100% (ordered rock salt type) depending on the synthesis conditions. Therefore, assuming random mixing of Fe and Os at each position, a constraint was imposed that occupancy(Fe) + occupancy(Os) = 1 at separate sites for the Fe and Os atoms. Based on EPMA measurements as shown in **Figure 3.3** and **Table 3.1, and 3.2**, the Fe to Os ratio was found to be close to 1:1. Therefore, in further refinement, additional constraints were added such that occupancy(Fe1) + occupancy(Fe2) = 1 and occupancy(Os1) + occupancy(Os2) = 1. The final result showed that Fe and Os atoms were partially ordered, with approximately 30% ordering in the oxide. Meanwhile, the oxygen atoms O1, O2, and O3 are located at independent 4*e*(*x*, *y*, *z*) sites, and their atomic displacement parameters were constrained to be equal. **Table 3.3** summarizes the crystallographic parameters obtained from this analysis.

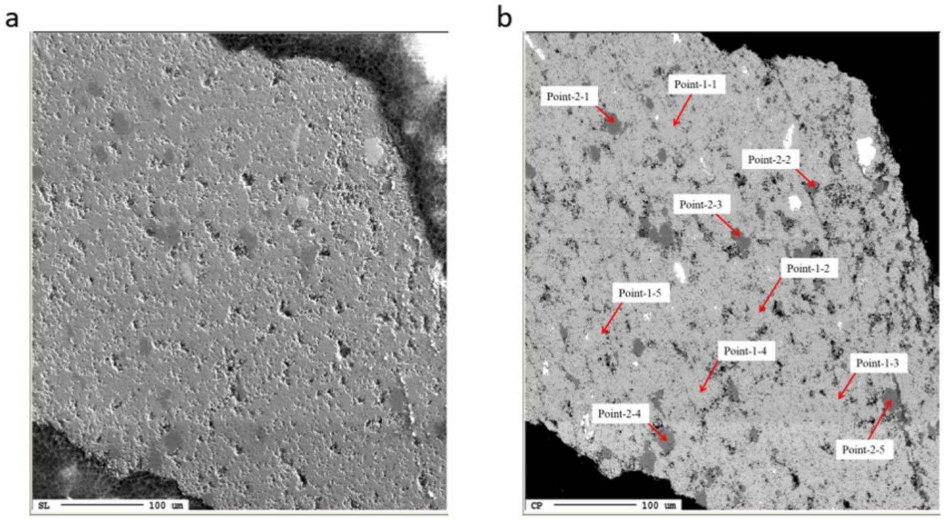

Figure 3.3. a) Scanning electron microscopy image at room temperature. b) Points selected for EPMA analysis: 1-1, 1-2, 1-3, 1-4, and 1-5 are located in the light grey region, while 2-1, 2-2, 2-3, 2-4, and 2-5 are located in the dark grey region.

Table 3.1 EPMA analysis results for selected points in the light grey region.

Points	Cd [at.%]	Fe [at.%]	Os [at.%]	O [at.%]
1-1	10.8	4.6	4.9	79.7
1-2	10.8	4.5	4.9	79.8
1-3	10.7	4.6	4.9	79.8
1-4	10.5	4.6	4.6	80.3
1-5	10.4	4.6	4.7	80.3
Average	10.6	4.6	4.8	80.0

Table 3.2 EPMA analysis results for selected points in the dark grey region.

Points	Cd [at.%]	Fe [at.%]	Os [at.%]	O [at.%]
2-1	8.6	15.1	0.1	76.1
2-2	8.6	15.3	0.1	76.1
2-3	8.6	15.3	0.1	76.0
2-4	8.6	15.2	0.1	76.1
2-5	8.4	15.1	0.1	76.5
Average	8.6	15.2	0.1	76.2

Table 3.3 Lattice Parameters of Cd_2FeOsO_6 at Room Temperature Obtained Using Synchrotron XRD.

Atom	Wyckoff	g	x	y	z	B (Å^2)
Cd	4e	1	0.9914(4)	0.0420(1)	0.2488(4)	0.884(23)
Fe1/Os1	2d	0.648/0.352(4)	0.5	0	0.0	0.146(27)
Os2/Fe2	2c	0.648/0.352	0.5	0	0.5	0.146(40)
O1	4e	1	0.0936(11)	0.4656(13)	0.247(3)	0.18(10)
O2	4e	1	0.688(3)	0.301(3)	0.047(4)	0.18
O3	4e	1	0.204(3)	0.202(3)	0.946(4)	0.18

Note. The space group was $P2_1/n$ (no. 14) at origin choice 2, $Z = 2$, and g was the occupation factor. In the oxide, $a = 5.35288(2)$ Å, $b = 5.44245(2)$ Å, $c = 7.68542(3)$ Å, $\beta = 90.0133(15)$ ° and $V = 223.898(1)$ Å^3. R Indices were $R_{wp} = 2.476\%$, $R_p = 1.746\%$, $R_B = 3.497\%$, $R_F = 3.062\%$ and $\chi^2 = 4$.

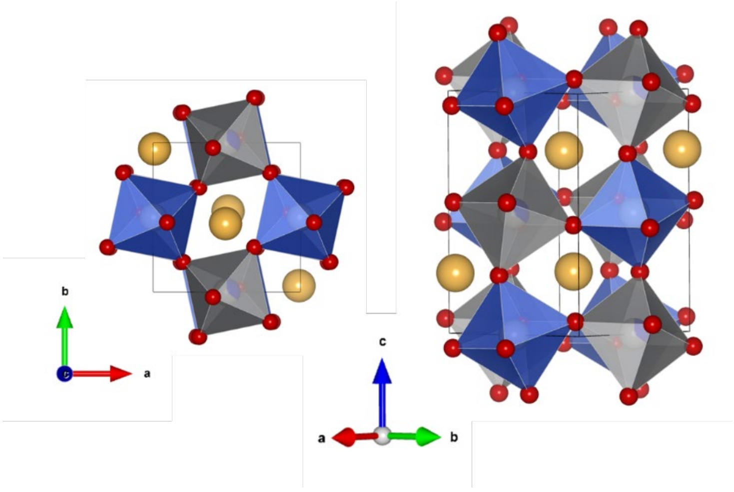

Figure 3.4 Crystal structure of Cd_2FeOsO_6, depicting OsO_6 and FeO_6 octahedra as blue and gray structures, respectively, while Cd and O atoms are represented by orange and red solid spheres.

Figure 3.4 shows the crystal model of Cd_2FeOsO_6, where the Fe and Os ions alternate in a manner similar to an intertwined backgammon board, exhibiting the same characteristics as the rock salt-ordered type DP oxide. The Fe1/Os1-centered octahedra are predominantly occupied by Fe, whereas for the Os2/Fe2-centered position, Os is more prevalent. **Table 3.4** displays the mean interatomic distances, bond valence sums (BVS), and selected bond angles at room temperature. The corresponding Fe-BVS for Cd_2FeOsO_6 is approximately 3.16, suggesting that the Fe is in a trivalent state. The average Fe-O bond length for Cd_2FeOsO_6 is approximately 1.997 Å, which is nearly equivalent to Ca_2FeOsO_6 (2.005 Å) [14]. Therefore, it is reasonable to assume that the Fe^{3+} in Cd_2FeOsO_6 is in a high-spin state, similar to Fe^{3+} in Ca_2FeOsO_6. The average Os-O bond length is approximately 1.983 Å, which is similar to the Os^{5+}-O bond lengths observed in other DP oxides, such as Sr_2FeOsO_6 (1.961 Å) [15] and Sr_2InOsO_6 (1.968 Å) [16]. However, the calculated BVS of Os was also considerably lower than the expected value of 5.00, with a value of 4.40. The underestimation seems to be common in perovskite-based Os oxides stabilized by high-pressure methods [14,17]. Moreover, the Fe-O-Os bond angles are 148.9°, 147.1°, and 147.9°. These angles deviate significantly from 180°, indicating a strong distortion in the octahedral bonding, as evident from the structural depiction in **Figure 3.4**.

Table 3.4 Selected Bond Lengths, Angles, and Bond Valence Sums (BVS) of Cd_2FeOsO_6 at Room Temperature.

Cd_2FeOsO_6	Bond Lengths (Å) or Angles (°) or BVS
Fe1–O1 (×2)	1.97(3)
Fe1–O2 (×2)	2.023(15)
Fe1–O3 (×2)	1.997(15)
BVS (Fe1)	3.16
Os2–O1 (×2)	2.02(3)
Os2–O2 (×2)	1.956(15)
Os2–O3 (×2)	1.974(15)
BVS (Os)	4.40
Fe1–O1–Os2	148.9(4)
Fe1–O2–Os2	147.1(12)
Fe1–O3–Os2	147.9(13)

[a] BVS = $\sum_{i=1}^{N} v_i$, v_i = exp[(R_0–l_i)/B], where N is the coordination number, B = 0.37. The values of R_0 are as follows: $R_0(\mathrm{F_e}^{3+})$ = 1.759 [18], $R_0(\mathrm{Os}^{5+})$ = 1.868 [17].

Figure 3.5 presents the ^{57}Fe Mössbauer spectra of Cd_2FeOsO_6 measured at 287 K. The ^{57}Fe Mössbauer spectrum of Cd_2FeOsO_6 exhibits a typical quadrupole doublet and the isomer shift (*IS*) value is 0.416 mm/s, which is within the expected range for Fe^{3+} ($t_{2g}^3e_g^2$ configuration) [19,20]. Therefore, the valence state of Fe is confirmed to be 3+, which is consistent with the results of the BVS analysis. The fitting parameters for Mössbauer spectroscopy are *IS* = 0.416(5) mm/s, QS = 0.553(8) mm/s, and FWHM = 0.57 (1) mm/s, where *IS*, QS, and FWHM represent the isomer shift, quadrupole splitting parameter and line width, respectively.

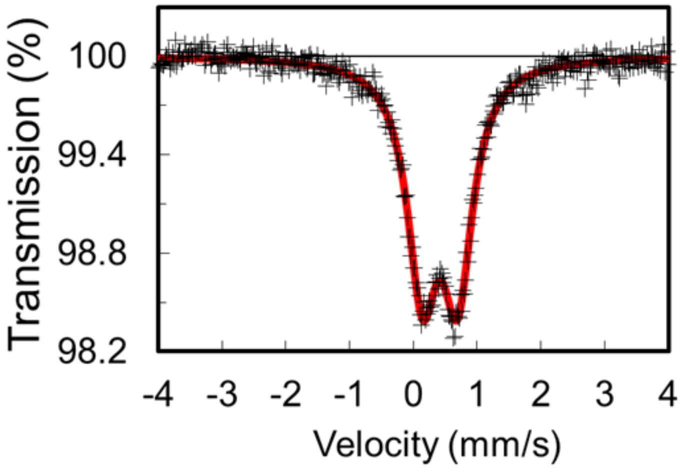

Figure 3.5. Mössbauer spectra measured at 287 K. The solid-colored curves represent the fitting results, while the small markers indicate the transmission profile.

Magnetic properties: Figure 3.6a demonstrates the thermal dependence of the magnetization of Cd_2FeOsO_6 under a magnetic field of 10 kOe. The plot clearly shows a significant increase in magnetization around 300 K, indicating the onset of long-range magnetic order. To further investigate this transition, isothermal magnetization curves were measured from 5 to 350 K after zero-field cooling, as depicted in **Figure 3.6b**. At 350 K, the *M*(*H*) curve appears nearly linear with no hysteresis, indicating a paramagnetic state for Cd_2FeOsO_6. Below 300 K, the magnetization exhibits FM-like behaviour with some hysteresis. However, even at 5 K and 70 kOe, the magnetization does not saturate, and the observed magnetic moment of approximately 0.16 μ_B/f.u. is significantly lower than the expected value of 8 μ_B/f.u. for fully ferromagnetically aligned Fe^{3+} and Os^{5+} ions. This discrepancy suggests the presence of FIM order, which yields a more reasonable saturated magnetic moment of 2 μ_B/f.u. Nevertheless, the observed value (<0.3 μ_B/f.u.) is still lower than the theoretical prediction (2 μ_B/f.u.). This difference can be attributed to the strong SOC of Os and the hybridization of O-2*p* and Os-5*d* orbitals, which leads to a reduction in the local magnetic moment to some extent [14]. Additionally, disorder at the B site is believed to decrease the net magnetization by inducing numerous AFM interactions between Fe^{3+} ions, as observed in Fe-based DP oxides [21].

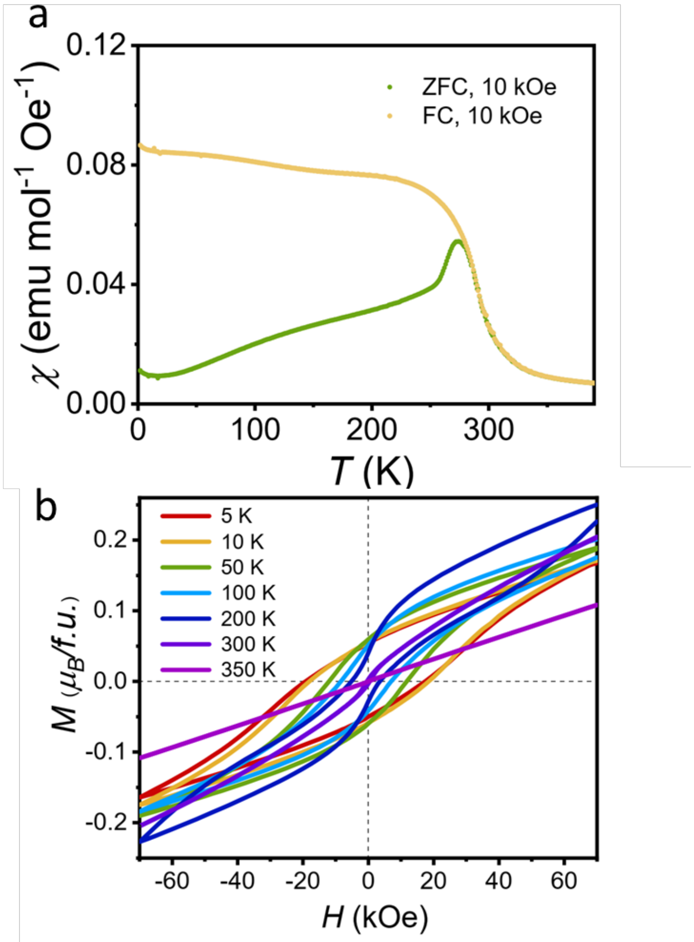

Figure 3.6: Magnetic properties of Cd_2FeOsO_6. (a) Temperature dependence of the magnetic susceptibility (χ) measured at a magnetic field of 10 kOe. (b) Isothermal magnetization curves measured at temperatures ranging from 5 K to 350 K.

At $T = 5$ K, large coercive forces of up to 20 kOe were observed, with the most notable feature being the shift of the magnetization versus magnetic field (*M-H*) curve along the magnetic field axis after cooling the sample in a H_{cool}. This suggests the possible presence of an EB effect in Cd_2FeOsO_6, similar to some FIM materials [7,19]. To confirm the presence of EB behaviour, a series of *M-H* curves were obtained at various H_{cool} values and different temperatures. **Figure 3.7** represents a typical curve, illustrating a significant EB effect and a VMS. Cooling the sample under a magnetic field of 70 kOe at 5 K resulted in a shift of the *M-H* curve towards the negative field direction, accompanied by an upward deflection of the hysteresis loop. Conversely, cooling at -70 kOe caused a shift in the positive field direction and distortion of the curve shape. Notably, even cooling fields as low as 150 Oe resulted in a significant shift of the hysteresis loop, as observed in the graph. The coercive field (H_C) and EB field (H_{EB}) were estimated from the *M-H* curve using the equations $H_C = |H_1 - H_2|/2$ and $H_{EB} = |H_1 + H_2|/2$, respectively, where H_1 and H_2 correspond to the lower and upper fields of the magnetization zero point [19,22]. The vertical magnetization shift (M_{shift}) was calculated as $M_{\text{shift}} = |M_+ + M_-|/2$, where M_+ and M_- are magnetizations at $H = 0$ [8].

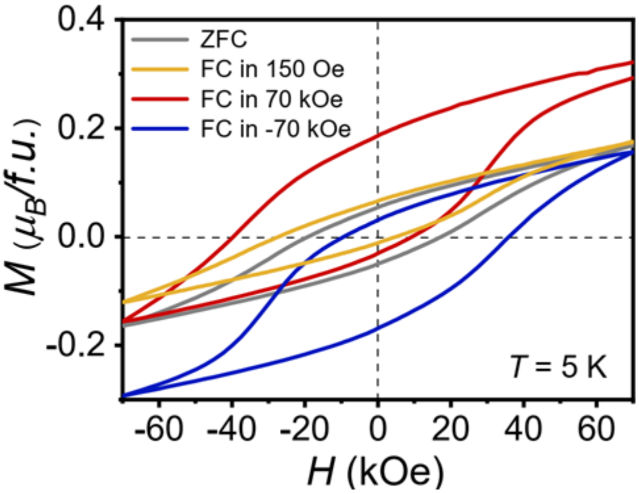

Figure 3.7. Selected magnetization versus magnetic field (*M-H*) loops obtained using the zero-field cooling (ZFC) and field cooling (FC) modes.

The influence of the applied cooling field on the EB and VMS effects was investigated. **Figure 3.8a** shown the full magnetization loops under different applied cooling fields at 5K, it is obviously both EB and VMS effects may enlarge as the applied cooling field increases. **Figure 3.8b** summarises the detailed values of the distortions to facilitate further in-depth analysis, it is clearly that an increase in M_{shift} was consistently accompanied by an improvement in H_{EB}. Notably, a weak applied field of only 80 Oe was sufficient to induce large EB effects up to 10 kOe, while a cooling field of 150 Oe resulted in significant EB effects exceeding 11 kOe. The temperature dependence of these effects under different cooling fields (both 70 kOe and 150 Oe) are shown in **Figure 3.9.** Panel a and b are the full set of cooling-field-dependent hysteresis under 70 kOe and 150 Oe, while the details are depicted in **Figure 3.9c.** Both H_C and H_{EB} decreased with increasing temperature, but the EB effects persisted up to approximately 260 K.

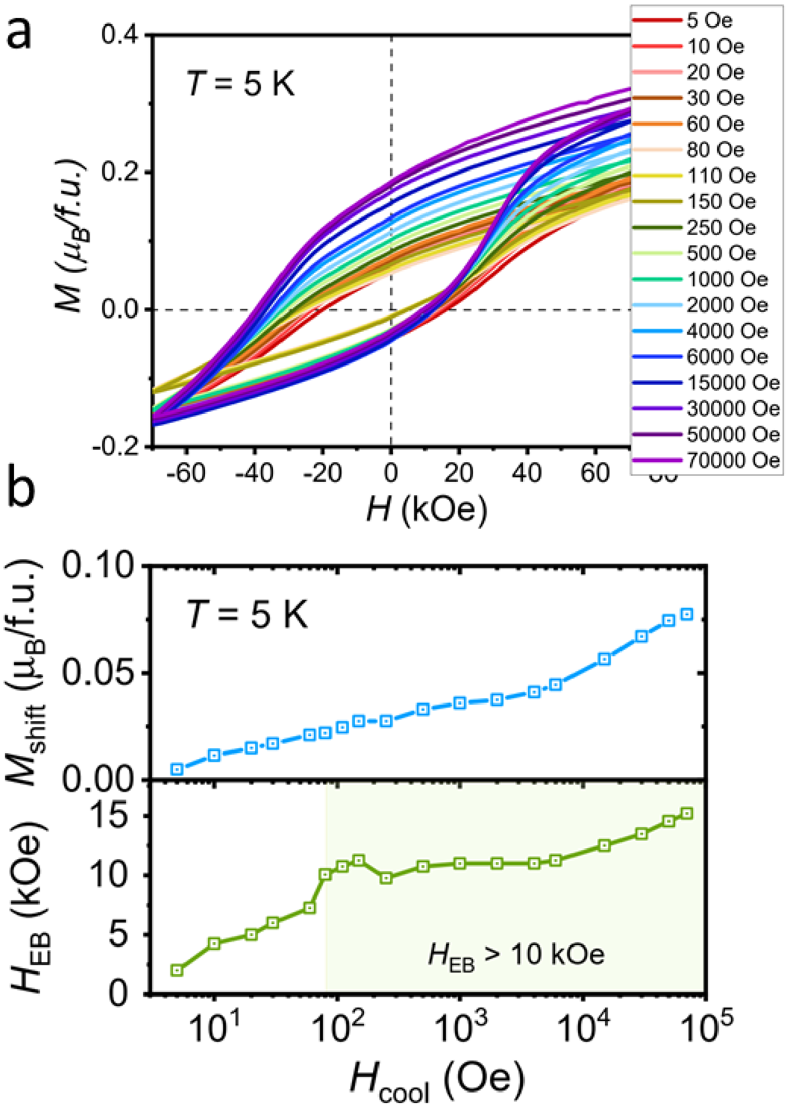

Figure 3.8: (a) Hysteresis loops under H_{cool} = 5, 10, 20, 30, 60, 80, 110, 150, 250, 500, 1k, 2k, 4k, 6k, 15k, 30k, 50k, and 70k Oe at 5 K. (b) shows the isothermal dependence of M_{shift} (top) and H_{EB} (bottom) on the cooling field.

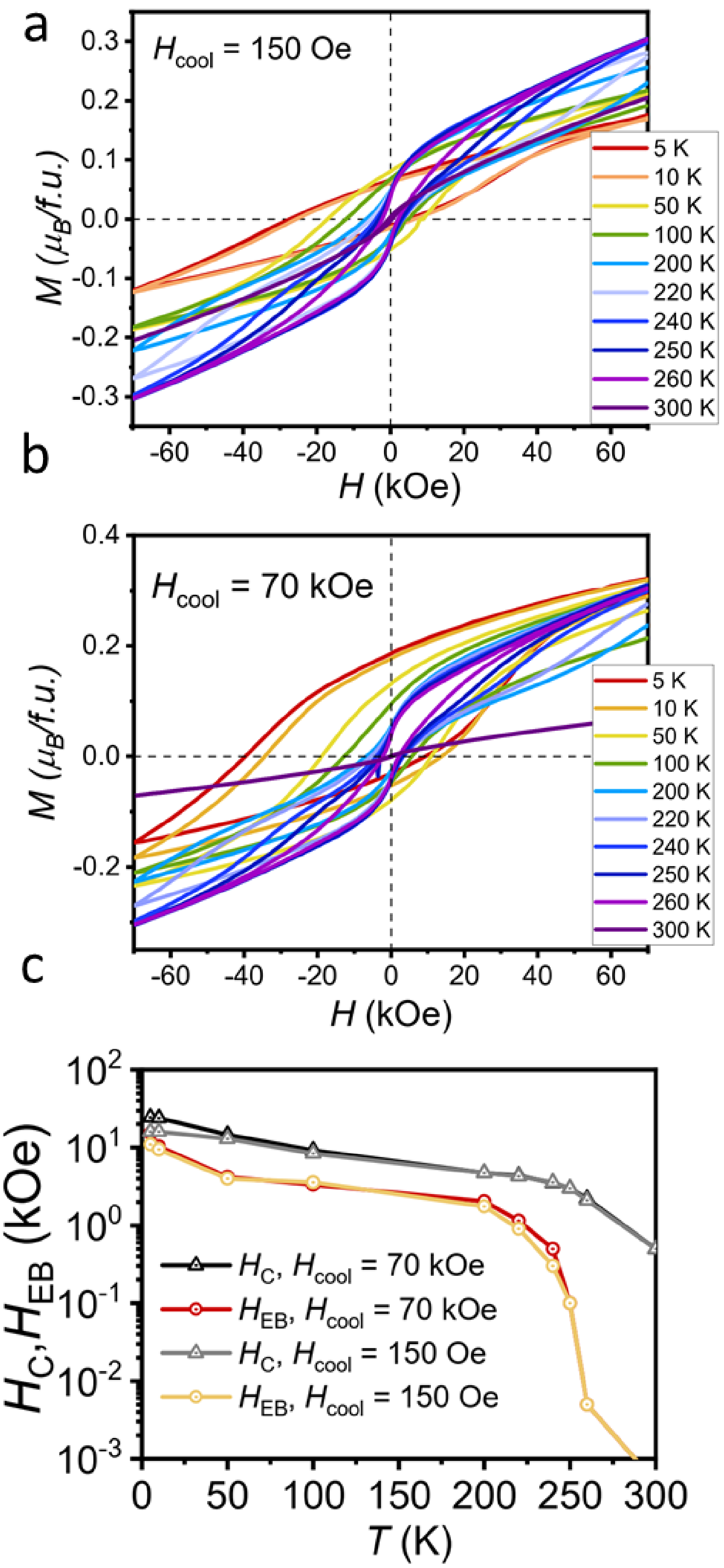

Figure 3.9 Temperature dependence magnetic loops under a cooling field of (a) 150 Oe and (b) 70 kOe at 5, 10, 50, 100, 200, 220, 240, 250, 260 and 300 K, respectively. (c) illustrates the temperature dependence of the H_{EB} of Cd_2FeOsO_6 after cooling with H = 70 kOe and H = 150 Oe.

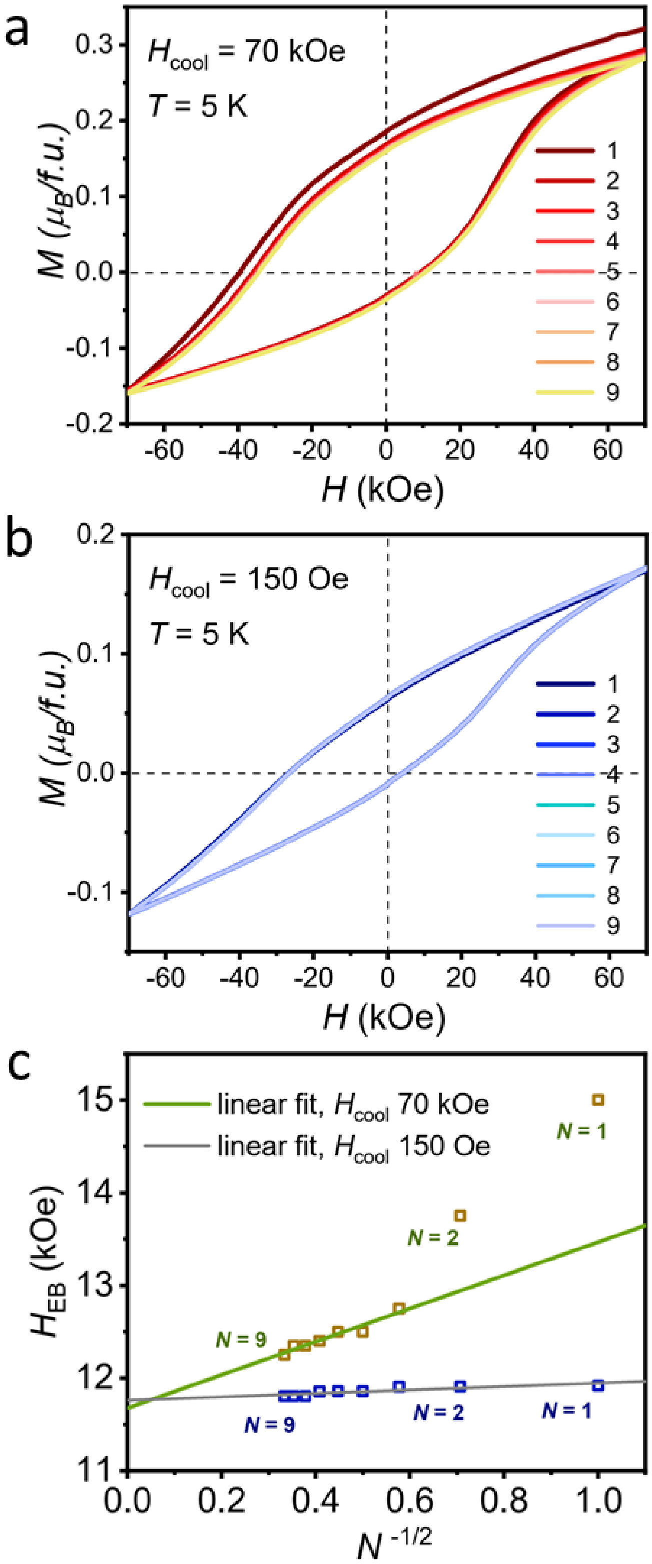

Figure 3.10. Training Effect of Cd_2FeOsO_6. Isothermal curves of ten consecutive repeated measurements performed at 5 K after a cooling field of (a) 70 kOe and (b) 150 Oe. (c) The H_{EB} values and the cycling index number N are fitted using the empirical power law.

An important phenomenon to consider when studying materials with EB effects is the training effect, where the H_{EB} tends to decrease with an increasing number of recycling cycles (N) [8]. **Figure 3.10a** and **Figure 3.10b** display the recycling hysteresis loops for $N = 1$ to 9 at 5 K under cooling fields of 70 kOe and 150 Oe. It is evident that there is a clear decrease in H_{EB} between the first and second loops. However, from cycle 2 to cycle 9, the decreasing trend gradually slows down. **Figure 3.10c** illustrates the decreasing trend of H_{EB} as a function of N, following the empirical power law: $H_{EB} - H_{EB}^{\infty} \propto 1/\sqrt{N}$ (where H_{EB}^{∞} represents the limit for an infinite loop). Linear fitting extrapolates H_{EB}^{∞} to ~11.7 kOe for a H_{cool} of 70 kOe and ~11.8 kOe for a H_{cool} of 150 Oe.

Conventional explanations of the EB effect in multilayer magnetic materials suggest that the orientation of AFM spins is minimally influenced by an external magnetic field. The interfacial spins of the FM layer are typically pinned by the strongly coupled AFM layer, requiring additional energy to reverse the magnetization of the FM layer and shift the Néel domain wall of the AFM layer [4]. In the case of Cd_2FeOsO_6, approximately 30% of the magnetic sublattice exhibits AFM ordering. This ordered AFM framework serves as a fixed attachment site for the FM spins within the layered material, while the remaining 70% of disordered distribution creates a heterogeneous environment generating localized FM clusters. Consequently, below the Curie temperature, the ordered AFM framework can spontaneously influence the arrangement of FM clusters. Additionally, subject to the strong SOC of Os, the rotation of magnetic moments is repressed, similar with the case of Ir in Y_2NiIrO_6 [23], while a new research suggested the strong SOC is believed to enhance the magnetic anisotropy at the coupling interface [24]. This scenario elucidates why a small applied magnetic field is sufficient to induce a significant EB effect.

Just before submitting this paper, I became aware of a related study on Y_2NiIrO_6 [23], which also investigated the enhancement of the EB effect in DP materials. The study proposed that SOC plays a significant role in the EB effect. However, there is a crucial distinction between the material, Cd_2FeOsO_6, and Y_2NiIrO_6. Cd_2FeOsO_6 exhibits a degree of ordering of 30%, while Y_2NiIrO_6 is near fully ordered. Additionally, I compared the findings to those of Ca_2FeOsO_6 [14], which shares the same crystal structure as Y_2NiIrO_6 and has a similar degree of ordering. Interestingly, no EB effect was reported in Ca_2FeOsO_6. These observations suggest that the mechanism responsible for the EB effect in Y_2NiIrO_6 cannot be universally applied to all DP materials. Therefore, I propose an alternative scenario to explain the EB properties of Cd_2FeOsO_6. The observations indicate that SOC-mediated magnetic interactions between the substrate and the disordered localized region are likely involved in generating the EB effect in Cd_2FeOsO_6.

It is worth highlighting that the EB effect in Cd_2FeOsO_6 exhibits a notable distinction from Y_2NiIrO_6. While the EB effect in Y_2NiIrO_6 is only observed below 170 K, in Cd_2FeOsO_6 it persists up to 260 K, which is close to room temperature. This extended temperature range is significant and holds great importance for practical applications. The ability to maintain the EB effect at higher temperatures in Cd_2FeOsO_6 opens up new avenues for manipulating and controlling magnetic properties. It also shows promise for the design of data storage and sensing devices that can operate effectively at or near room temperature, a highly desirable characteristic. Consequently, Cd_2FeOsO_6 provides valuable insights for advancing the field and facilitating the development of novel technologies in these domains.

I conducted C_p measurements for Cd_2FeOsO_6 from 2 K up to 390 K while cooling. As shown in **Figure 3.11a**, the curve was similarly smooth, but the characteristic peak, thought to be due to a phase transition near room temperature, was unclear due to the noise. Therefore, I applied a magnetic field in the high-temperature range and conducted a remeasurement. As shown in the right inset, the peak broadened under the magnetic field, confirming that it was a peak due to a magnetic transition, not noise. The magnetic transition temperature obtained from the transition peak was around 285 K.

The low-temperature specific heat divided by temperature (C_p/T) versus T^2 data was analysed using the approximate Debye model $C_\mathrm{p}/T = \beta T^2+\gamma$, where γ is the electronic specific heat coefficient, and β is a constant that relates to the Debye temperature θ_D (proportional to $\beta^{-1/3}$). As illustrated in the left inset, the linear fitting gives $\gamma = 2.42(10)\times10^{-3}$ J mol^{-1} K^{-2} and $\beta = 6.94(2)\times10^{-4}$ J mol^{-1} K^{-4}. This small γ value corresponds to the semiconducting behaviour of Cd_2FeOsO_6, which will be further discussed below. The estimated θ_D based on β is determined to be 303.6(3) K.

In addition, I investigated the electrical resistivity (ρ) of Cd_2FeOsO_6 using crystalline pellets shaped into rods. The transport characteristics were examined under various magnetic fields. **Figure 3.11b** depicts the thermal evolution of $\rho(T)$, which shows minimal influence from the external magnetic field. The inset clearly indicates that the material exhibits electrical semiconducting properties following Mott‘s variable range hopping behaviour, which is similar to other osmium double-perovskite oxides, such as Ca_2CoOsO_6 [25].

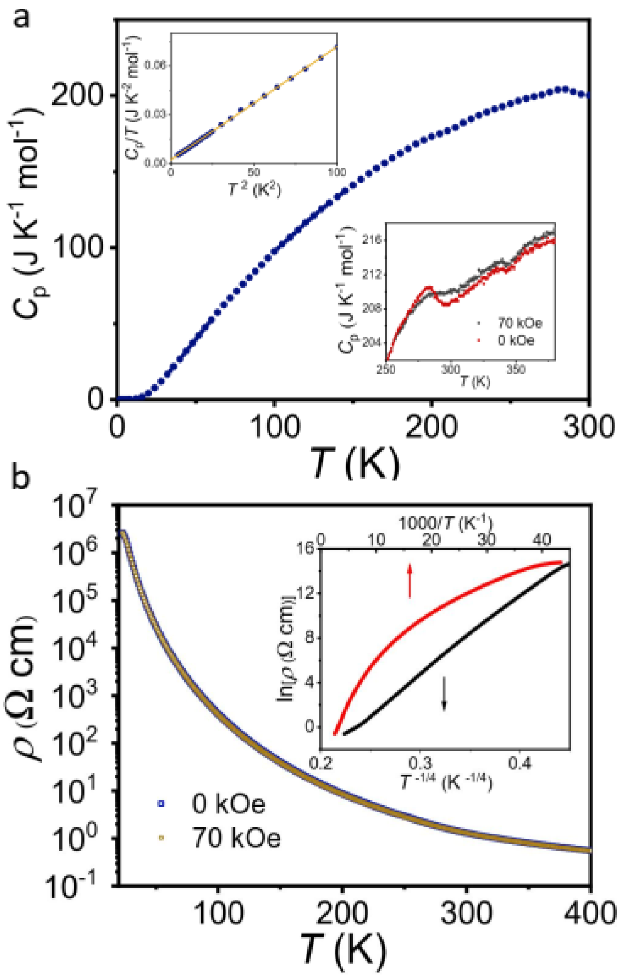

Figure. 3.11: (a) Temperature dependence of C_p for Cd_2FeOsO_6 below 300 K. The left inset shows a linear fit to the low-temperature part of C_p/T vs. T^2 and the right inset shows the temperature dependence of C_p at high temperatures under zero magnetic field and a field of 70 kOe, (b) Temperature dependence of the $\rho(T)$ of Cd_2FeOsO_6 under different magnetic fields. The inset shows the corresponding ln(ρ) vs T^{-1} and ln(ρ) vs $T^{-1/4}$ curves of Cd_2FeOsO_6.

Cd^{2+} ions are marginally smaller than Ca^{2+} ions ($r_{Cd}{}^{2+}$ = 1.31 Å; $r_{Ca}{}^{2+}$ = 1.34 Å), but they have significantly higher electronegativity (χ_{Cd} = 1.69; χ_{Ca} = 1.00). This difference in electronegativity between Cd^{2+} and Ca^{2+} ions, along with the strong covalent Cd-O bonding, can lead to interesting phenomena in perovskite oxides containing Cd at the A site. For example, $CdTiO_3$, a perovskite oxide with Cd [26], exhibits a ferroelectric phase transition, unlike its counterpart $CaTiO_3$. Additionally, polar structures have been observed in Cd-Nb-O pyrochlore-type oxides due to the covalent Cd-O bonds [27]. Therefore, the combination of Cd at the A site and unpaired spins at the *B*/*B*' sites hold the potential for pioneering multiferroic properties.

In this study, a new double perovskite oxide, Cd_2FeOsO_6, was successfully synthesized. However, the compound crystallizes in the $P2_1/n$ space group with centrosymmetric symmetry, and no ferroelectric structural features were observed throughout the measured temperature range (100 K - 800 K). In future studies, it is suggested to replace Os^{5+} ions with d^0 ions such as W^{6+} and Ta^{5+} to explore the possibility of discovering practical multiferroic materials. This substitution could induce polarization in the crystal structure through the second order Jahn-Teller effect [28], potentially leading to the realization of desirable multiferroic properties.

3.2. Cd_2FeReO_6: a high-T_C double perovskite oxide with remarkable tunneling magnetoresistance

3.2.1. Introduction

B-site-ordered double perovskite (DP) oxides $A_2BB'O_6$ have been at the forefront of research in recent years due to their extraordinary magnetic and electrical properties, such as multiferroic behavior, half-metallic characteristics, and high Curie temperature (T_C).[29–31] These properties emerge from the interplay between the two ordered B and B' sublattices. In particular, DP oxides that combine 3d transition metals with 4d (or 5d) transition metals at B and B' sites have garnered significant attention as a frontier in material research for several decades, owing to their excellent properties. For instance, Sr_2FeMoO_6 exhibited a substantial magnetoresistance (~10%) at room temperature, [29] while Sr_2CrOsO_6 demonstrated an extremely high T_C (~725 K) [25,32].

Among the DP oxides, A_2FeReO_6 (A = Ca, Sr, Pb, Ba) form an impressive family due to their high Curie temperature (T_C) and magnetoresistance effects may lead useful applications in magnetic devices [33]. Systematic studies were carried out, revealing that the A-site ion significantly affects both of these properties. For example, the T_C appears to be inversely proportional to the ionic radius of the A-site ion, [34] suggesting that T_C may further increase with a reduced ionic radius. On the other hand, researchers have done some retrospective work on the origin of the magnetoresistance and different perspectives have emerged. Kobayashi et al. suggested the intergrain tunnelling process should be responsible for the magnetoresistance while Gopalakrishnan et al. supposed the conductive ground state and notable magnetoresistance are strongly influenced by the size and covalency tendency of A-cation inside the A_2FeReO_6 serials [33].

The size of Cd^{2+} ions is similar to that of Ca^{2+} ions ($r_{Cd}{}^{2+}$ = 1.31 Å; $r_{Ca}{}^{2+}$ = 1.34 Å); however, their Pauling electronegativity is significantly larger (χ_{Cd} = 1.69; χ_{Ca} = 1.00). Consequently, Cd-O bonds may exhibit a strong covalent character, and it is expected that this strong covalency may lead to various exotic phenomena [35], such as a covalency-driven structural evolution in the polar Cd-Nb-O pyrochlore system [27] and ferroelectric phase transition in perovskite-type oxides $CdTiO_3$ [26]. Therefore, with these considerations in mind, I attempted to synthesize a novel compound, Cd_2FeReO_6, with the following three objectives: first, to pursue a higher T_C; second, to investigate the impact of the A-site ion on the magnetoresistance effects; and third, to explore the potential for a polar ferrimagnet.

As a result, a new double perovskite Cd_2FeReO_6 was successfully achieved. Here, I report on the synthesis, crystal structure, and magnetic as well as electronic transport properties of the new member of A_2FeReO_6 family. In particular, it showed ferrimagnetic ordering at 460 K and exhibited soft magnetism, meanwhile its semiconducting behavior followed the Mott's variable-range-hopping (VRH) model and a tunnel magnetoresistance of -37% was involved in it.

3.2.2. Experimental

Polycrystalline Cd_2FeReO_6 was synthesized under high pressure and high temperature conditions. Cd_2FeReO_6 was prepared by mixing CdO (99.99%, Togawa Chemical), Fe_2O_3 (99.998%, Alfa Aesar), ReO_3 (laboratory made from 99.99% Re, Rare Metallic Co. Ltd.), and Fe (99.99%, Rare Metallic Co. Ltd.) in stoichiometric ratio and sealing the mixture in a Pt capsule. The capsule was then placed in a belt-type high-pressure apparatus and heated at 1400 °C under 6 GPa pressure for 1 hour. After heating, the capsule was quenched to room temperature and the pressure was gradually released over 40 minutes.

Synchrotron XRD data were recorded during a large temperature range (100-800 K) using a large Debye-Scherrer camera at beamline BL02B2 at SPring-8 [9,10]. two monochromatic beams with wavelength of 0.420259 Å and 0.420186 Å were used for the measurements. Before the measurements, a benchmark test was performed using a standard material (CeO_2) to determine the actual wavelength. A Lindemann glass capillary (inner diameter: 0.1mm) was used to collected the sample and it was rotated during the measurement. The RIETAN-VENUS program [11,12] was used for the analysis of the synchrotron XRD pattern.

Magnetic susceptibilities of Cd_2FeReO_6 were measured in the range of 2-570 K under an applied magnetic field of 10 kOe and conditions of zero-field cooling (ZFC) and field cooling (FC), using a magnetic property measurement system (MPMS3, Quantum Design Inc, San Diego, California). Isothermal magnetization measurements were performed between -70 to 70 kOe at different temperatures. The magnetic transport properties were performed using a four-probe method between 2 K and 400 K under magnetic fields up to 90 kOe using a physical property measurement system (PPMS, Quantum Design). The specific heat capacity (C_p) data were collected by a relaxation method using the commercial calorimeter option of the PPMS.

A zero-field ^{57}Fe Mössbauer spectrum was measured at room temperature (287 K) using a Wissel MVT-1000 Mössbauer spectrometer, with a ^{57}Co/Rh source in transmission mode. The sample was uniformly dispersed with α-Al_2O_3 and enclosed in a small acrylic container to form a thin layer. All Mössbauer spectra were calibrated at room temperature using α-Fe and analyzed using the MossA software package [13].

To verify the accurate composition of the high-pressure products, electron probe microanalysis (EPMA) was performed using a JEOL JXA-8500F instrument. The sintered surface was polished precisely with a 0.3 μm alumina-coated film.

3.2.3. Results and discussion

The crystal structure of Cd_2FeReO_6 was analyzed by synchrotron XRD. The space group $P2_1/n$ could be used to fit the crystal structure successfully, similar with many B-site-ordered DP oxides that have been reported previously. Although a trace impurity of ReO_2 (approximately 1.2 wt%) was detected in the sample, the majority of the sample was found to be pure DP oxide. The refined XRD pattern is displayed in **Figure 4.12**. The lattice constants for Cd_2FeReO_6 were determined to be $a = 5.35718(1)$ Å, $b = 5.44670(2)$ Å, $c = 7.69712(2)$ Å, and $\beta = 90.0676(3)$ °.

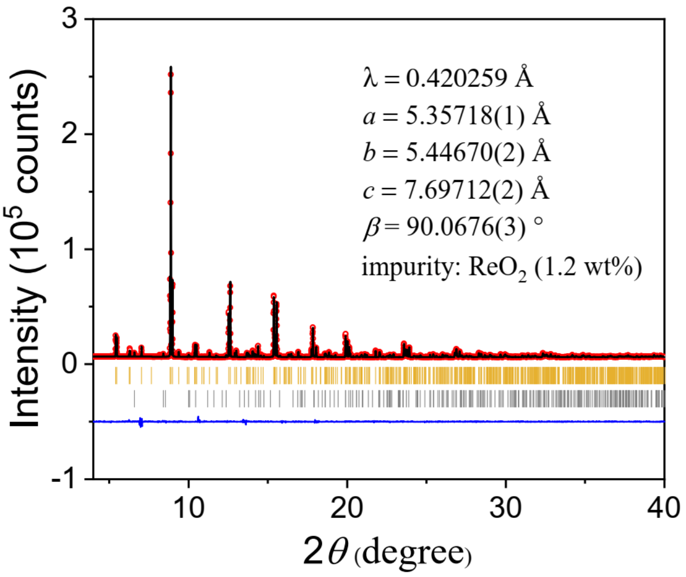

Figure 3.12. The refined synchrotron XRD pattern of Cd_2FeReO_6 with ReO_2 at room temperature (296-300 K). The observed pattern (circles), calculated pattern (solid lines), as well as a difference profile are shown in the panel. The vertical bars show possible Bragg reflection positions for Cd_2FeReO_6 (the first row) as well as impurity (the second row).

During the preliminary Rietveld refinement, it was observed that Cd atoms completely occupy the 4e(x, y, z) Wyckoff position. The P21/n structure model provided two independent Fe and Re sites, with the degree of B-site ordering varying depending on the synthesis conditions, ranging from 0% (completely disordered) to 100% (ordered rock-salt type). In the refinement process, I assumed that Fe and Re are randomly mixed at each individual position and imposed the constraint Occupancy(Fe) + Occupancy(Re) = 1 on the separate Fe and Re sites. The EPMA measurements further revealed that the Fe and Re ratio was close to 1:1 [Cd: Fe: Re: O = 17.0(4): 9.0(2): 8.7(1): 65.3(5) over 5 point average in at.%]. Therefore, to account for this observation, I added the constraints occupancy(Fe1) + occupancy(Fe2) = 1 and occupancy(Re1) + occupancy(Re2) = 1 in the refinement. The final results from the refinement indicate that Fe and Re atoms are partially ordered, with approximately 70% ordering. Additionally, the oxygen atoms O1, O2, and O3 are all located at independent 4e(x, y, z) sites. Detailed information regarding the structure refinement can be found in **Table 3.5**, while **Table 3.6** summarizes the reliable indexes and crystallographic parameters in detail.

Table 3.5 Crystallographic Parameters and structure refinement details of Cd_2FeReO_6 at 296 K

Source	Synchrotron
Chemical formula	Cd_2FeReO_6
Formular weight g/mol	562.870
Pressure	Ambient pressure
Wavelength (Å)	0.420259
Space group (No.)	$P2_1/n$ (no.14)
a (Å)	5.35718 (1)
b (Å)	5.44670 (2)
c (Å)	7.69712 (2)
α (°)	90
β (°)	90.0676 (3)
γ (°)	90
V (Å$^{3)}$	224.594 (1)
Z	2
d-space range (deg)	2~40
χ^2	4.0636
R_p (%)	1.685
R_{wp} (%)	2.387

Table 3.6 Structure parameters of Cd_2FeReO_6 at 296 K, which were analyzed using synchrotron XRD.

Atom	Wyckoff	g	x	y	z	B (Å^2)
Cd	4e	1	0.9919(3)	0.0411(1)	0.2505(2)	0.811(19)
Fe1/Re1	2d	0.839/0.161(3)	0.5	0	0.0	0.022(33)
Re2/Fe2	2c	0.839/0.161	0.5	0	0.5	0.017(10)
O1	4e	1	0.0988(10)	0.4633(12)	0.2431(11)	0.127(84)
O2	4e	1	0.6969(14)	0.2963(13)	0.0413(16)	0.127
O3	4e	1	0.1977(14)	0.2013(13)	0.9476(16)	0.127

Note. The space group was $P2_1/n$ (no. 14) at origin choice 2, $Z = 2$, and g was the occupation factor. Cd_2FeReO_6: $a = 5.35718(1)$ Å, $b = 5.44670(2)$ Å, $c = 7.69712(2)$ Å, $\beta = 90.0676(3)$° and $V = 224.594(1)$ Å^3. R Indices were $R_{wp} = 2.387\%$, $R_p = 1.685\%$, $R_B = 3.05\%$, and $R_F = 2.367\%$.

To investigate whether a phase transition occurred over a wide temperature range, in situ synchrotron XRD measurements were performed from 100 K to 800 K. As shown in **Figure 3.13a**, the peak positions shifted slightly to the lower angle side due to heating over the entire temperature range. This temperature change may be attributed to thermal expansion. A few unidentified impurities were formed at 800 K (see asterisks in the main panels). As shown in **Figure 3.13b**, lattice constants were determined from the XRD patterns, and all lattice constants showed a monotonous temperature change, suggesting no occurrence of the polar phase transition assumed in the temperature range of the measurement.

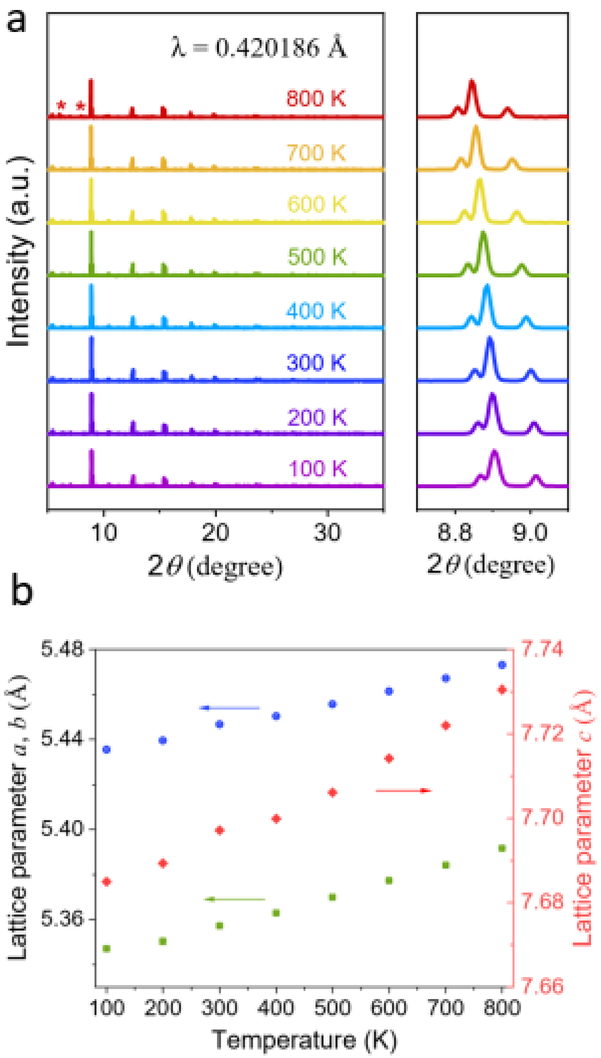

Figure 3.13. (a) In situ SXRD measurements from 100 K to 800 K. Asterisks represent unknown impurities. (b) Temperature dependence of the lattice parameters of Cd2FeReO6. The parameter β and the unite cell volume are not plotted for clarity.

Figure 3.14 shows the crystal model of Cd_2FeReO_6, where the Fe and Re ions alternate in a manner similar to an intertwined backgammon board, exhibiting the same characteristics as the rock salt-ordered type DP oxide. The Fe1/Re1-centered octahedra is predominantly occupied by Fe, whereas for the Re2/Fe2-centered position, Re is more prevalent. The mean interatomic distances, bond valence sums (BVS), and selected bond angles at room temperature are displayed in **Table 3.7**.

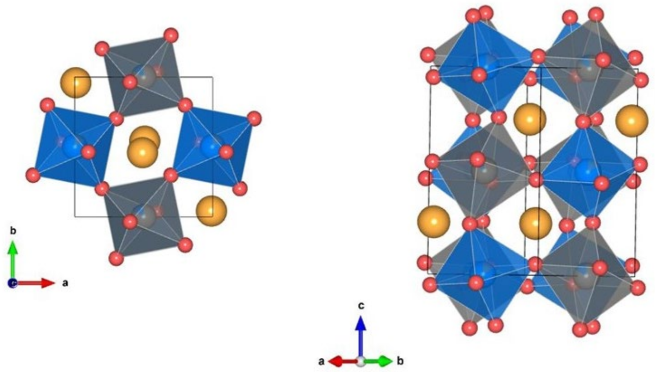

Figure 3.14. The crystal structure of Cd_2FeReO_6, blue and grey polyhedron show ReO_6 and FeO_6 octahedron respectively while Cd and O atoms are represented as orange and red solid spheres.

Table 3.7 Selected bond lengths, angles, and bond valence sums (BVS) of Cd_2FeReO_6 at room temperature.

	Cd_2FeReO_6
Fe1–O1 (×2)	2.065(9)
Fe1–O2 (×2)	1.957(8)
Fe1–O3 (×2)	1.995(8)
BVS (Fe1)	3.10
Re2–O1 (×2)	1.946(9)
Re2–O2 (×2)	1.984(8)
Re2–O3 (×2)	1.987(8)
BVS (Re)	4.43
Fe1–O1–Re2	147.2(4)
Fe1–O2–Re2	151.5(6)
Fe1–O3–Re2	147.2(6)

Note. BVS = $\sum_{i=1}^{N} v_i$, $v_i = \exp[(R_0 – l_i)/B]$, where N is the coordination number, B = 0.37. The values of R_0 are as follows: $R_0(\mathrm{F_e}^{3+}) = 1.759$ [18], $R_0(\mathrm{Re}^{5+}) = 1.86$ [38].

The average bond length of Fe-O in Cd_2FeReO_6 was 2.01 Å, which is comparable to that of Ca_2FeReO_6 (2.03 Å). [33] The BVS of Fe corresponding to this bond length was 3.10, suggesting that Fe in the compound is close to trivalent. It is reasonable to assume that the Fe^{3+} in Cd_2FeReO_6 is in a high-spin state, as is the Fe^{3+} in Ca_2FeReO_6. [33] On the other hand, the calculated BVS (4.43) was considerably smaller than the ideal value (5.00), although the average Re-O bond length <Re-O>=1.972 Å was comparable to the sum of Re^{5+} and O^{2-} ionic radii (1.98 Å). Upon further investigation, this situation was observed in other similar high-pressure products. For example, in Pb_2FeReO_6, <Re-O> = 2.00 Å and the BVS value of Re was 4.27, [39] which is also much smaller than the ideal value (5.00). It is possible that under-bonding is a common phenomenon in Re oxides stabilized at high pressure. The inter-octahedral Fe-O-Re bond angles are 147.2°, 151.5°, and 147.2°. These angles deviate significantly from 180°, indicating a stronger torsion of the inter-octahedral bonding.

The ^{57}Fe Mössbauer spectrum of Cd_2FeReO_6 measured at 287 K is shown in **Figure 3.15**. Like shown in the graph, it exhibits magnetic hyperfine splitting, indicating that the magnetic transition temperature is above room temperature. However, unlike the single six-line pattern, the spectrum can be roughly fitted by two strongly pronounced sextets with two smaller quadrupoles splitting. Usually, magnetic compounds with non-cubic symmetry have an electric field gradient and exhibit quadrupole interactions. Therefore, the combination of quadrupole interactions and magnetic hyperfine interactions is common [40]. The difference between the two sextets may be due to the fact that Cd_2FeReO_6 is not a completely ordered DP oxide but contains antisite defects. Consequently, the misplacement of Fe ions may cause different local environments, resulting in the two sets of hyperfine parameters. All the Mössbauer fitting parameters are summarized in **Table 3.8**. Based on the *IS* as well as the hyperfine fields (B_{hf}), It is confident that the Fe ions are in the 3+ oxidation state [19,20].

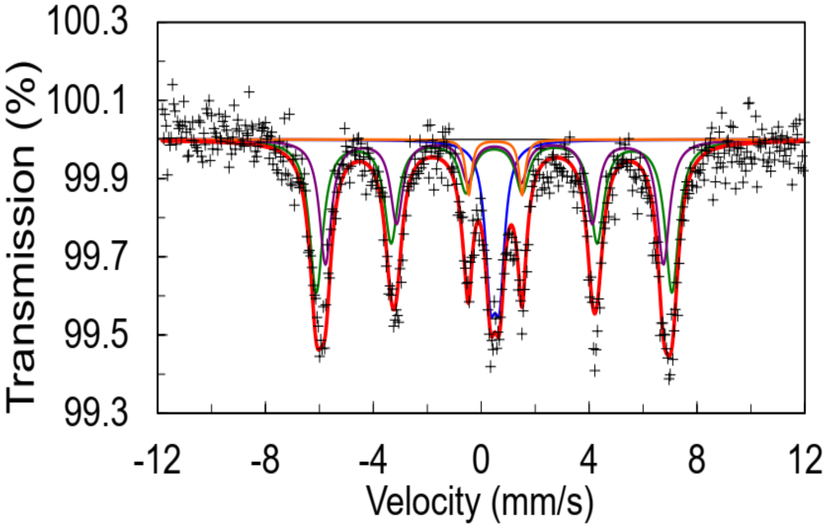

Figure 3.15. The ^{57}Fe Mössbauer spectra of Cd_2FeReO_6 measured at 287 K. The solid-colored curves correspond to the fitting, while the small markers represent the transmission.

Table 3.8. Fitting parameters of the Mössbauer spectrum of Cd_2FeReO_6 at 287 K.

components	*IS* (mm s^{-1})	B_{hf} (T)	QS (mm s^{-1})	FWHM (mm s^{-1})	*A* (%)
Fitting 1 (blue)	0.51(3)	-	0.333(55)	0.47(11)	16(2)
Fitting 2 (orange)	0.53(5)	-	1.982(91)	0.28(15)	4(1)
Fitting 3 (green)	0.48(2)	40.9(5)	-	0.61(12)	46(3)
Fitting 4 (purple)	0.49(2)	38.9(5)	-	0.55(15)	34(3)

Note: *IS*, B_{hf}, QS, and FWHM, and *A* correspond to the isomer shift, hyperfine field, quadrupole splitting parameter, line width, and relative area fraction, respectively. The colors in Figure 3 correspond to the respective subspectra.

The temperature dependence of the magnetic susceptibility of Cd_2FeReO_6 with an applied magnetic field of 10 kOe is presented in **Figure 3.16a**. The magnetic susceptibility was measured using the oven mode of MPMS3, up to 570 K, as the zero-field cooling (ZFC) curve and field cooling (FC) curve remained divergent at 390 K. A significant decrease was observed around 460 K, indicating a loss of long-range magnetic order. At 390 K, a small gap appears between the data sets obtained using different measuring modes, which is likely caused by a technical issue.

At higher temperatures, a preliminary Curie-Weiss fitting of the inverse susceptibility within the paramagnetic range (500-570 K) suggests a significantly positive Weiss temperature of 440 K. However, the observed magnetic moment is 3.77 μ_B per formula unit (f.u.), notably smaller than the theoretically expected spin-only moment of 6.56 μ_B per f.u. It is plausible that the chosen temperature range for the analysis was either too narrow or situated too closely to the magnetic transition point, possibly affecting the accuracy of the results.

The isothermal magnetizations of Cd_2FeReO_6 at 5 and 300 K are presented in **Figure 3.16b**. The spontaneous magnetization does not saturate even at 5 K, and its value of around 2.27 μ_B/f.u. is much lower than the theoretical FM-aligned spin-only magnetization of 7 μ_B/f.u. In contrast, it is closer to the difference of each spin-only magnetization (3 μ_B/f.u.), suggesting that Cd_2FeReO_6 is more likely to behave as a ferrimagnet. The underestimated moment may be the consequence of the large spin-orbit interaction of Re, similar to other cases [38,41]. The hysteresis loops for Cd_2FeReO_6 are all very narrow, indicating that it is a soft ferrimagnet. Even at 5 K, the coercive field (H_C) was only ~900 Oe. The remnant magnetization (M_r) was ~1.87 μ_B/f.u. at 5 K.

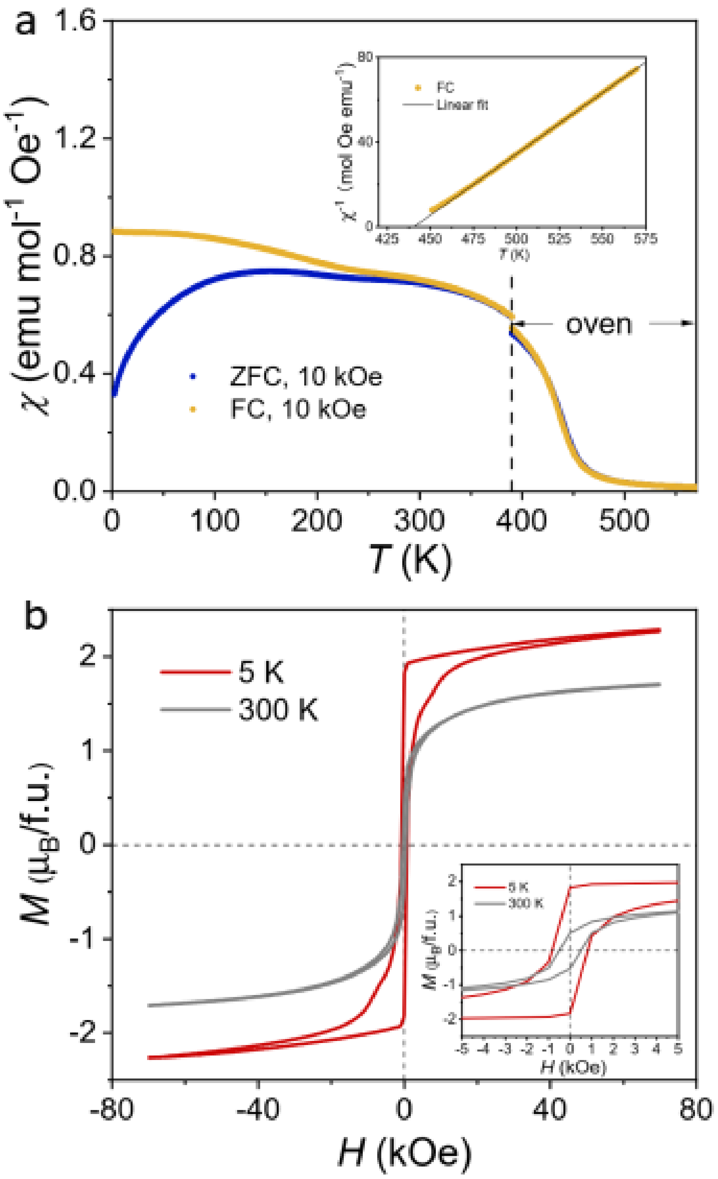

Figure 3.16. (a) Temperature dependence of χ and χ^{-1} (inset) of Cd_2FeReO_6 measured under H = 10 kOe. (b) Isothermal magnetization curves of Cd_2FeReO_6 at 5 K and 300 K.

The electrical resistivity, $\rho(T)$, was investigated using the rectangular polycrystalline pellet. As shown in **Figure 3.17a**, Cd_2FeReO_6 behave as a semiconductor throughout the entire temperature range at both zero magnetic field and 70 kOe. Two different fits were attempted for the data under zero field conditions, as depicted in the inset. The $\rho(T)$ was found to be nearly linear on the $T^{-1/4}$ scale, which is consistent with Mott's VRH conduction mechanism: $\rho(T) = \rho_0\exp[(T_0/T)^{1/4}]$, similar to other DP oxides such as Ca_2FeReO_6 [42].

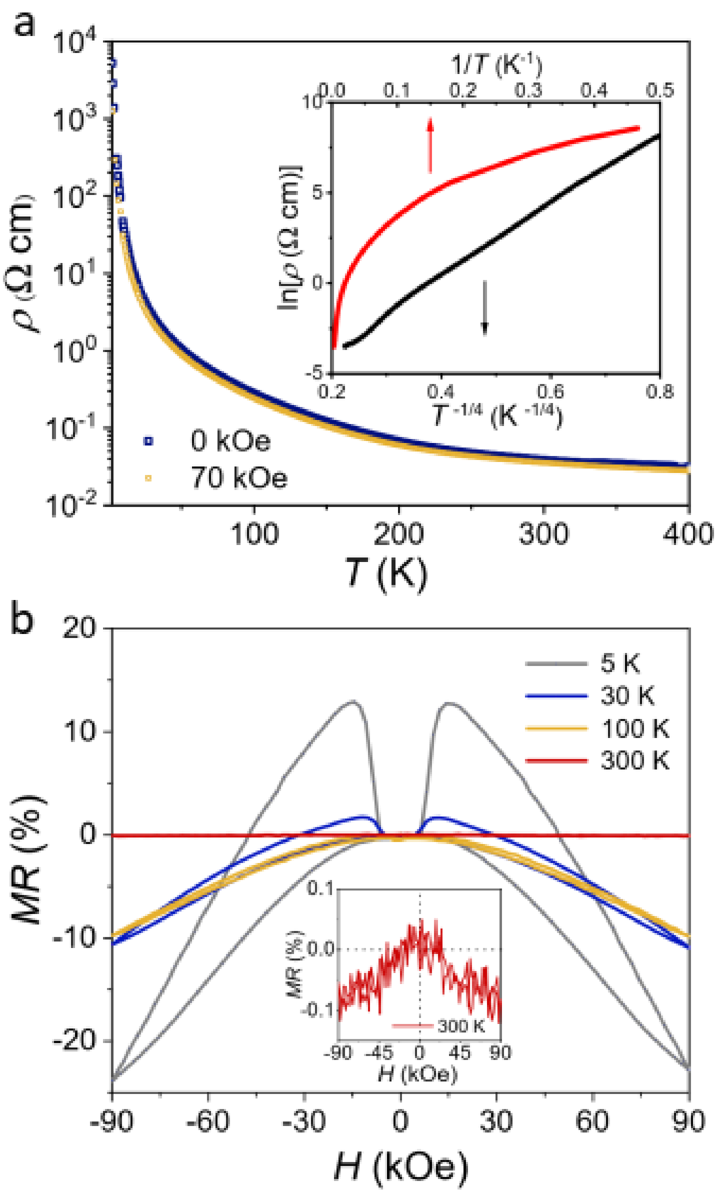

Figure 3.17. (a) The electrical resistivity of Cd_2FeReO_6 as a function of temperature under various magnetic fields, inset shows the corresponding ln(ρ) vs. T^{-1} and ln(ρ) vs. $T^{-1/4}$ curves of Cd_2FeReO_6. (b) The magnetoresistance of Cd_2FeReO_6 at temperatures of 5, 30, 100, and 300 K.

The most striking feature of this compound is the appearance of tunnel magnetoresistance; as in Sr_2FeReO_6,[35] the magnitude of magnetoresistance is defined as $MR(H) = 100\times[\rho(H)-\rho(0)]/\rho(0)$, where $\rho(0)$ is the resistance at zero field. The difference between the maximum and minimum magnetoresistance values reaches -37% at $T = 5$ K and $H = 90$ kOe, which is considerably larger than that of other members of the A_2FeReO_6 family. For example, for A = Ca, Pb, the magnetoresistance values are about 0%, for Ba -10% (5 K, 50 kOe),[43] and even for Sr, the most well-studied member, -21% (4.2 K, 70 kOe). [35] Even for the entire DP family, the maximum magnetoresistance value is -42% (4.2 K) for Sr_2FeMoO_6, [29] therefore the magnetoresistance observed in Cd_2FeReO_6 is quite impressive. However, unlike the case of Sr_2FeMoO_6, the magnetoresistance of Cd_2FeReO_6 decreases significantly with increasing temperature, down to about -0.1% at room temperature, as shown in the inset in **Figure 3.17b**.

C_p measurements were conducted for Cd_2FeReO_6 from 2 to 300 K while cooling. As illustrated in **Figure 3.18**, the C_p values for Cd_2FeReO_6 showed a continuous evolution over the entire temperature range, with fluctuations occurring at high temperatures that were likely attributed to technical noise caused by grease. The low-temperature C_p/T vs. T^2 data for the compound were fitted assuming lattice (C_{latt}), metallic (C_{el}) and hyperfine (C_{hyp}) contributions are included. Then the model becomes: $C_p/T = A/T^3 + \beta_1 T^2 + \beta_2 T^4 + \gamma$, in which the hyperfine contribution is $C_{hyp} = A/T^2$, the lattice term is $C_{latt} = \beta_1 T^3 + \beta_2 T^5$, and the metallic contribution could be written as $C_{el} = \gamma T$, where γ is the electronic specific heat coefficient and β_1 is a constant that relates to the Debye temperature Θ_D [43]. For Cd_2FeReO_6, a plot fit yields A = 211(27) mJ K mol^{-1}, $\gamma = 4.6(14)$ mJ mol^{-1} K^{-2} and $\beta = 4.2(2)\times10^{-4}$ J mol^{-1} K^{-4}, estimating the Debye temperature Θ_D value to be approximately 359(5) K. The non-zero γ value indicates that the conduction electrons contribute to C_p, somewhat divergent from the large resistance found at low temperatures. There are two possible sources for this discrepancy: first, since there is large disorder degree, some local spin-glassy behaviors may exist in the sample which may contribute to the observed non-zero γ [44]. On the other hand, the boundaries inside the polycrystalline sample may lead to significant electron scattering which will result in a higher resistivity as well. Attempts were made to obtain a sizeable single crystal to gain a more accurate value but so far, I did not get a single crystal sample with sufficient size for the resistivity measurements. Follow-up efforts should also be sustained to obtain more accurate results. Moreover, the non-zero A value consistent with the upturn in the C_p/T term at $T < 5$ K, indicating that, in addition to the electronic and lattice contributions, hyperfine contribution indeed exists in the sample.[45]

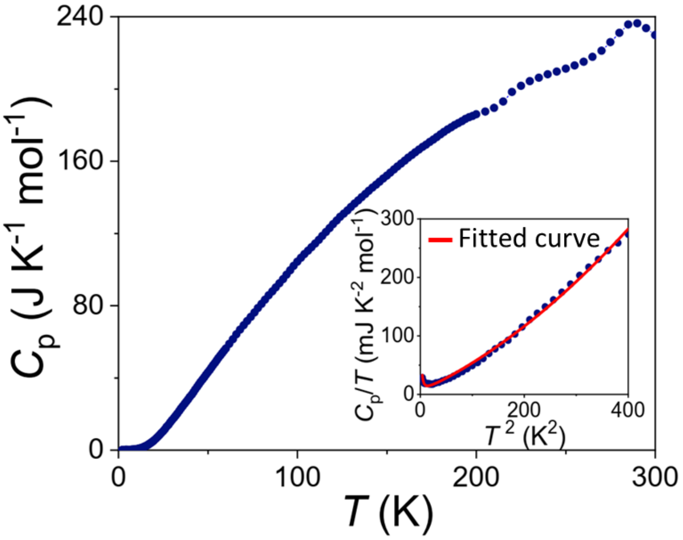

Figure 3.18. Temperature dependence of C_p for Cd_2FeReO_6 below 300 K. The inset shows a fitted curve of the low-temperature part of C_p/T vs. T^2.

To gain a deeper understanding of the magnetic and electrical properties of Cd_2FeReO_6, first-principles calculations were conducted using experimental structure parameters. In these calculations, the Fe and Re atoms were assumed to be perfectly ordered. The total and partial density of states (DOS) calculated by GGA without SOI are presented in **Figure 3.19a**. In this figure, the dashed line represents the Fermi energy (E_F), and the lowest panel shows the total DOS, while the other panels display the partial DOSs decomposed into atomic species. For comparison, the total and partial DOSs of Ca_2FeReO_6 were also calculated, which were based on the experimental structure of the low-temperature phase. [42] These results are shown in **Figure 3.19b**. The overall structures of the DOSs for Cd_2FeReO_6 and Ca_2FeReO_6 are similar; however, there are some minor differences between the two compounds. One noticeable difference is the contribution from Cd in Cd_2FeReO_6, which is distributed in a wide energy region, unlike the almost negligible contribution from Ca in Ca_2FeReO_6 in the energy region presented in **Figure 3.19a**. The DOS of Cd in Cd_2FeReO_6 arises from its 4d and 5s orbitals. This suggests that the hybridization between Cd and O is larger than that between Ca and O, as expected from the differences in Pauling electronegativity.

Within the framework of GGA, the calculated Cd_2FeReO_6 compound exhibits ferrimagnetism with a spin moment of 3.0 μ_B per formula unit. The electronic states between -7.5 eV and -2.0 eV are identified as O 2p bands that are hybridized with Fe 3d, Re 5d, and other orbitals. Above -2.0 eV, the states around the Fermi energy are primarily composed of

Fe 3d and Re 5d orbitals with hybridization of O 2p orbitals. The Fe 3d and Re 5d bands further split into e_g and t_{2g} bands. Notably, the Re 5d-e_g bands, which exist above 5 eV, are not shown in **Figure 3.19a** and **3.19b**. In the majority spin channel, the Fe 3d bands are fully occupied, while in the minority spin channel, they are positioned above the Fermi energy. On the other hand, the minority-spin Re 5d-t_{2g} bands are partially occupied. As a result, the majority spin DOS vanishes at the E_F, indicating that Cd_2FeReO_6 is characterized as a half-metal. In this scenario, minority-spin electrons exhibit metallic behavior, while minority-spin electrons behave like insulators with an energy gap of approximately 0.4 eV. This half-metallic behavior leads to complete spin-polarization of the conduction electrons at the Fermi level, making Cd_2FeReO_6 highly promising for spintronics applications. Similar to other half-metallic compounds,[29,41,46] the half-metallicity in Cd_2FeReO_6 is expected to result in a decrease in resistivity in the presence of an applied magnetic field, which is consistent with the experimental findings.

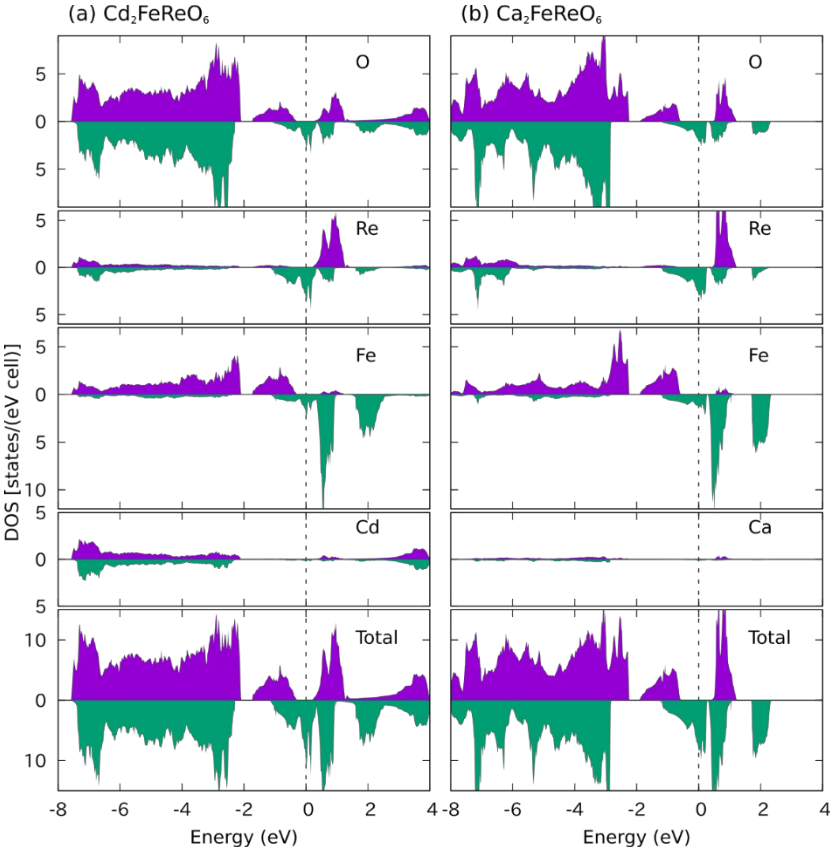

Figure 3.19. Total and partial DOS calculated using the GGA method without SOI for (a) Cd_2FeReO_6 and (b) Ca_2FeReO_6. The partial DOS of atomic species were calculated from the projected weights in muffin-tin radii. In each panel, the upper (lower) half presents the majority (minority) spin DOS.

How the electronic structure of Cd_2FeReO_6 is affected by on-site Coulomb interaction (U) and SOI were further explored. To investigate this, $U_{Fe} = 4$ eV was set and varied the U_{Re} up to 4 eV. Additionally, three different magnetic directions for the magnetization (M), namely M // (001), (010), or (100) were considered. The calculated total DOS is summarized in **Figure 3.20**. These findings indicate that even with the inclusion of SOI, the majority spin DOS at the E_F remains small. When the U_{Re} was increased up to 4 eV, Cd_2FeReO_6 exhibited a small energy gap opening. Interestingly, this behavior is qualitatively similar to previous calculations for Ca_2FeReO_6, [47] but there are quantitative differences between these two compounds. Specifically, it is observed that M // (001) yields the lowest energy for Cd_2FeReO_6 among the three magnetic directions tested. With this specific direction of M, Cd_2FeReO_6 remains metallic up to $U_{Re} = 3$ eV and opens an energy gap of approximately 0.08 eV at $U_{Re} = 4$ eV. In contrast, when the magnetization is directed to (010), the energy gap opens at a smaller U_{Re} value of 3 eV. Notably, in the case of Ca_2FeReO_6, the M // (010) gives the lowest energy, resulting in an energy gap opening at a smaller U_{Re} value of 3 eV. This discrepancy in behavior between Cd_2FeReO_6 and Ca_2FeReO_6 may be attributed to differences in the local structure around the Re atoms. [42]

Indeed, the contrasting magnetoresistance behaviors observed in Cd_2FeReO_6 and Ca_2FeReO_6 are intriguing. The absence of significant magnetoresistance in Ca_2FeReO_6, [43] despite its close structural similarity to Cd_2FeReO_6, suggests that even subtle differences in their electronic states can have a substantial impact on the magnetoresistance phenomenon. Understanding the underlying reasons for these discrepancies can provide valuable insights into the unique properties of double perovskite oxides and guide the design of materials with tailored functionalities. It is essential to note that the theoretical study did not consider the experimentally observed 30% antisite disorder in Cd_2FeReO_6. The presence of antisite disorder could have profound effects on the electronic and magnetic properties of the material, including its magnetoresistance behavior. Therefore, conducting further theoretical investigations that incorporate the effects of antisite disorder may shed light on the origin of the observed magnetoresistance in Cd_2FeReO_6.

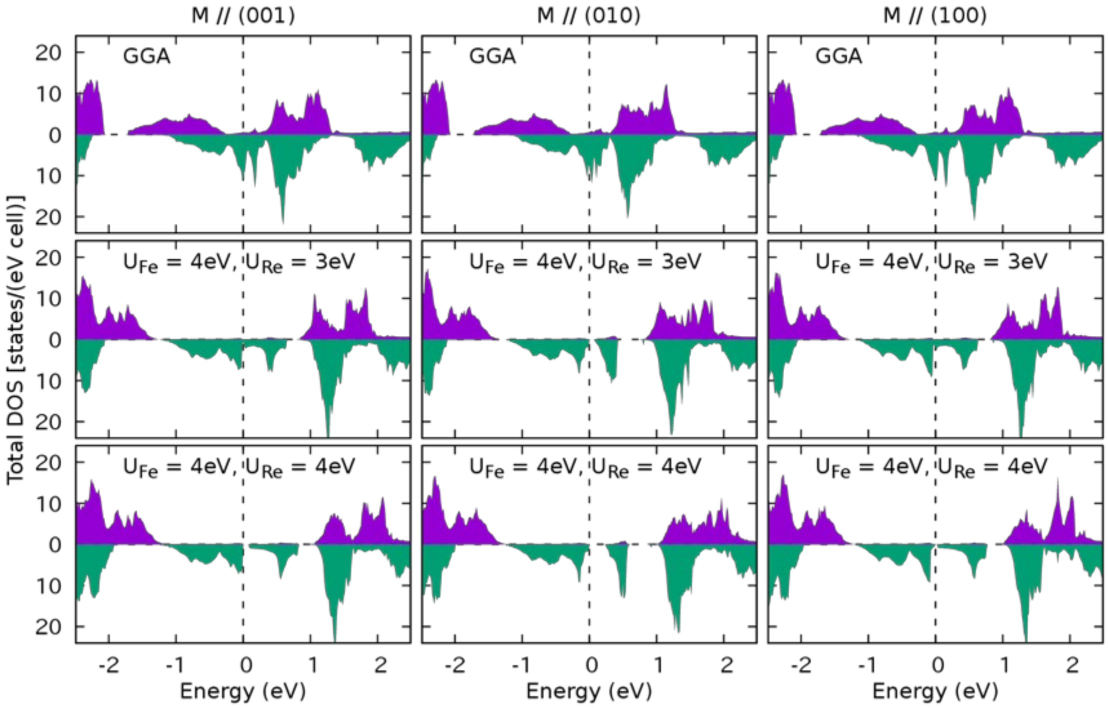

Figure 3.20: Total DOS of Cd_2FeReO_6 calculated using the GGA and GGA+*U* methods with SOI.

As illustrated in introduction, the non-magnetic A-site series A_2FeReO_6 (A = Ba, Pb, Sr, Ca) family presents a high Curie temperature (T_c), which appears to be inversely proportional to the ionic radius [34], the tendency has been plotted in **Figure 3.21**. and according to the graph, the hypothetical T_C corresponding to Cd is around 560 K, as indicated by the hollow star. However, the value obtained in the experiments was around 460 K, as shown by the solid star, which was different from the initial prediction. It is highly likely that large antisite disorder had a negative effect on the magnetic transition. This disorder may have led to the occurrence of local AFM Fe-O-Fe bonding, which disturbed the magnetic homogeneity over long ranges and significantly contributed to the decrease in T_c [48,49]. I attempted to produce high-pressure materials with less antisite disorder, but unfortunately, impurities such as $Cd_2Re_2O_7$ appeared when the temperature was lowered. Therefore, I believe that much higher pressure is necessary to obtain more ordered compounds with promising higher T_c.

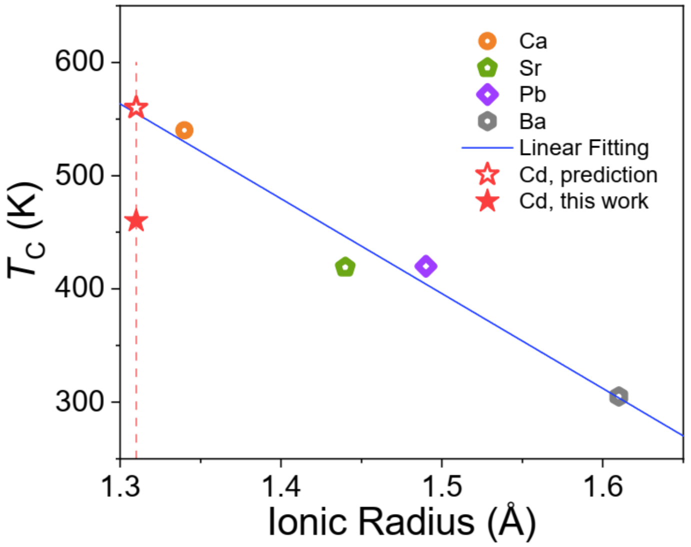

Figure 3.21. Roughly linear relationship between the ionic radius and the imaginary and real T_c of Cd_2FeReO_6. Data used in this plot: Ca [50], Sr [51], Pb [39], Ba [52].

Kobayashi *et al.* [35] investigated the analogous tunneling magnetoresistance of Sr_2FeReO_6 and attributed it to either inside the grain or at the domain boundaries as the main cause of the observed magnetoresistance. Meanwhile, Gopalakrishnan *et al.* [33] had offered a different insight about the magnetoresistance based on systematic studies of the A_2FeReO_6 series. They suggested that the higher magnetic tunability of Sr oxide could be primarily due to its location on the metal-insulator boundary between the metallic Ba and insulating Ca compound. Interestingly, although the sample is insulating, similar to the Ca counterpart (20 mΩ cm for Ca_2FeReO_6 [43] and 30 mΩ cm for Cd_2FeReO_6 at room temperature), the typical spin-valve-type magnetoresistance was observed in the compound.

The source of the magnetoresistance in the sample is therefore likely due to the fact that, as the applied magnetic field gradually increases, the spins within the microcrystalline domains begin to align orderly but not yet completely in one direction. As I will illustrate later, the compound is in a half-metallic state; thus, when the spin-polarized electron currents pass through magnetic regions with different magnetization directions, considerable scattering of spins may lead to the increase in resistivity. With the increase in the applied field, the domain-rotation process is then completed, and the spin scattering is substantially suppressed, resulting in the decrease in resistance. A comparison with the magnetization curve shows that the magnetic field at the turning point in magnetoresistance corresponds to the point where the magnetization curve flattens out. The high dependence of magnetoresistance on magnetic domain configuration and the decrease in the magnitude of magnetoresistance with increasing temperature suggest that the suppression of spin-dependent scattering by applied magnetic fields, either inside the grain or at the domain boundaries, is the main cause of the observed magnetoresistance.

Very recently, giant positive magnetoresistances, reaching up to thousands of percent, have been observed in thin films of half-metallic double perovskites. [53,54] It is crucial to note that these phenomena stem from an entirely distinct mechanism and are typically only viable at very low temperatures (below 10 K). Moreover, they exhibit a high sensitivity to temperature changes, with slight increases in temperature leading to substantial reductions in magnetoresistance values. On another front, significant linear magnetoresistance is also observed in certain topological insulators and Dirac or Weyl semimetals, such as Bi_2Te_3,[55] Cd_3As_2, [56] TaAs, [57] TlBiSSe. [58] Among these materials, the giant linear magnetoresistance can even reach 80000% at 9 T in Cd_3As_2.[42] However, the distinctive magnetoresistance exhibited by these materials arises from an entirely separate mechanism linked to modifications in the Fermi surface. Consequently, in comparison to typical ferromagnetic and ferrimagnetic oxides, which usually demonstrate negative magnetoresistance, the material continues to display a noteworthy tunneling magnetoresistance.

3.3. Conclusion

This study presents the synthesis and characterization of two novel oxides, Cd_2FeOsO_6 and Cd_2FeReO_6, and investigates their fundamental properties. Both compounds adopt the $P2_1/n$ space group.

In the Os-oxide, approximately 30% ordering is observed between the Fe and Os ions at the B site while the Re-oxide exhibits around 70% partially ordering of Fe^{3+} and Re^{5+} in the B site. Cd_2FeOsO_6 undergoes a ferromagnetic-to-paramagnetic transition at around 285 K. Notably, an EB effect is observed near this transition temperature (~260 K) and becomes more pronounced at lower temperatures. Interestingly, a substantial EB effect of 10 kOe is achieved with a remarkably weak applied magnetic field of 80 Oe, which is a noteworthy finding. The involvement of a partially ordered host material and the strong SOC of Os is suggested as a possible explanation for these observations, which deviates from existing mechanisms proposed for the EB effect. Further investigations are needed to gain a better understanding of the underlying mechanisms and to enhance the EB properties. In conclusion, this study presents a promising approach to harnessing the properties of partially ordered DP materials to achieve a significant EB effect near room temperature using a small cooling field. The results highlight the potential for substantial improvements in material properties through the strong SOC of 5*d* elements. Moreover, the synthesis of new DP oxides incorporating Cd at the A site opens up avenues for exploring advanced materials with potential applications. This work contributes to the field of materials science by demonstrating the feasibility of exploiting unique properties and lays the foundation for further advancements in this area.

For Cd_2FeReO_6, approximately 70% ordering of Fe^{3+} and Re^{5+} ions is discovered at the perovskite B-site. The presence of antisite disorder in Cd_2FeReO_6 may have influenced the empirically predicted high T_C of ferrimagnetic ordering; nonetheless, the measured T_C of 460 K significantly exceeds room temperature. Cd_2FeReO_6 exhibited semiconductor behavior consistent with Mott's variable-range hopping conduction model. However, the most remarkable property observed was its substantial low-field butterfly-type tunneling magnetoresistance of -37% at 5 K. This tunneling magnetoresistance is likely attributed to the modulation of spin scattering by an externally applied magnetic field during the domain rotation process. First-principles calculations further supported that Cd_2FeReO_6 displays a half-metallic state, which offers a plausible explanation for the observed magnetoresistance behavior. The distinct magnetoresistance behaviors exhibited by Cd_2FeReO_6 and Ca_2FeReO_6, along with the presence of antisite disorder in Cd_2FeReO_6, pose intriguing avenues for future research. Developing a comprehensive understanding of these factors through both theoretical investigations and experimental studies will prove essential in unlocking the full potential of double perovskite oxides and in exploring novel materials with unique magnetic and electronic properties for a range of technological applications.This study contributes to the expanding body of knowledge concerning the double perovskite family, underscoring its potential significance in the realm of materials science and spintronics research. The promising properties identified in Cd_2FeReO_6 and its related compounds warrant further investigation and exploration. By delving deeper into the electronic states and accounting for the effects of antisite disorder, invaluable insights into the remarkable attributes of double perovskite oxides could be obtained, thereby opening doors to their potential applications in various technological advancements.

Reference in Chapter 3

(1) Anusree V. K., Ranjana R. Das, P. Neenu Lekshmi, Ramchandra Dhal, Claire V. Colin, P. N. Santhosh. Giant Exchange Bias Effect in Ruddlesden-Popper Oxides $SrLaFe_{0.25+x}Mn_{0.25}Co_{0.5-x}O_4$(X=0,0.25): Role of the Cluster Glass Magnetic Phase in a Quasi-Two-Dimensional Perovskite. *Phys. Rev. B* **2020**, *102* (13), 134405.

(2) Fanghua Tian, Yebei Li, Qizhong Zhao, Kaiyan Cao, Dingchen Wang, Zhiyong Dai, Zhonghai Yu, Xiaoqin Ke, Yin Zhang, Chao Zhou, Wenliang Zuo, Sen Yang, Xiaoping Song. Giant Exchange Bias Induced via Tuning Interfacial Spins in Polycrystalline Fe_3O_4/CoO Bilayers. *Phys. Chem. Chem. Phys.* **2021**, *23* (8), 4805–4810.

(3) Eran Maniv, Ryan A. Murphy, Shannon C. Haley, Spencer Doyle, Caolan John, Ariel Maniv, Sanath K. Ramakrishna, Yun-Long Tang, Peter Ercius, Ramamoorthy Ramesh, Arneil P. Reyes, Jeffrey R. Long, James G. Analytis. Exchange Bias Due to Coupling between Coexisting Antiferromagnetic and Spin-Glass Orders. *Nature Physics* **2021**, *17* (4), 525–530.

(4) R. L. Stamps. Mechanisms for Exchange Bias. *J. Phys. D: Appl. Phys.* **2000**, *33* (23), R247.

(5) Zhe Ying, Bo Chen, Chunfeng Li, Boyuan Wei, Zheng Dai, Fengyi Guo, Danfeng Pan, Haijun Zhang, Di Wu, Xuefeng Wang, Shuai Zhang, Fucong Fei, Fengqi Song. Large Exchange Bias Effect and Coverage-Dependent Interfacial Coupling in $CrI_3/MnBi_2Te_4$ van Der Waals Heterostructures. *Nano Lett.* **2023**, *23* (3), 765–771.

(6) Yingying Wu, Wei Wang, Lei Pan, Kang L. Wang. Manipulating Exchange Bias in a Van Der Waals Ferromagnet. *Advanced Materials* **2022**, *34* (12), 2105266.

(7) Ajaya K. Nayak, Michael Nicklas, Stanislav Chadov, Panchanana Khuntia, Chandra Shekhar, Adel Kalache, Michael Baenitz, Yurii Skourski, Veerendra K. Guduru, Alessandro Puri, Uli Zeitler, J. M. D. Coey, Claudia Felser. Design of Compensated Ferrimagnetic Heusler Alloys for Giant Tunable Exchange Bias. *Nature Mater* **2015**, *14* (7), 679–684.

(8) Lei Ding, Lihua Chu, Pascal Manuel, Fabio Orlandi, Meicheng Li, Yanjiao Guo, Zhuohai Liu. Giant Spontaneous Exchange Bias in an Antiperovskite Structure Driven by a Canted Triangular Magnetic Structure. *Mater. Horiz.* **2019**, *6* (2), 318–325.

(9) M. Tanaka, Y. Katsuya, A. Yamamoto. A New Large Radius Imaging Plate Camera for High-Resolution and High-Throughput Synchrotron X-Ray Powder Diffraction by Multiexposure Method. *Review of Scientific Instruments* **2008**, *79* (7), 075106.

(10) M. Tanaka, Y. Katsuya, Y. Matsushita, O. Sakata. Development of a Synchrotron Powder Diffractometer with a One-Dimensional X-Ray Detector for Analysis of Advanced Materials. *Journal of the Ceramic Society of Japan* **2013**, *121* (1411), 287–290.

(11) F. Izumi, K. Momma. Three-Dimensional Visualization in Powder Diffraction. *Solid State Phenomena* **2007**, *130*, 15–20.

(12) K. Momma, F. Izumi. VESTA: A Three-Dimensional Visualization System for Electronic and Structural Analysis. *J Appl Cryst* **2008**, *41* (3), 653–658.

(13) C. Prescher, C. McCammon, L. Dubrovinsky. MossA: A Program for Analyzing Energy-Domain Mössbauer Spectra from Conventional and Synchrotron Sources. *J Appl Cryst* **2012**, *45* (2), 329–331.

(14) Hai L. Feng, M. Arai, Y. Matsushita, Y. Tsujimoto, Y. Guo, C. I. Sathish, X. Wang, Y. Yuan, M. Tanaka, K. Yamaura. High-Temperature Ferrimagnetism Driven by Lattice Distortion in Double Perovskite Ca_2FeOsO_6. *J. Am. Chem. Soc.* **2014**, *136* (9), 3326–3329.

(15) Avijit Kumar Paul, Martin Jansen, Binghai Yan, Claudia Felser, Manfred Reehuis, Paula M. Abdala. Synthesis, Crystal Structure, and Physical Properties of Sr_2FeOsO_6. *Inorg. Chem.* **2013**, *52* (11), 6713–6719.

(16) Sudipta Kanungo, Binghai Yan, Claudia Felser, Martin Jansen. Active Role of the Nonmagnetic Cations in Magnetic Interactions for the Double-Perovskite Sr_2BOsO_6 (B=Y, In, Sc). *Phys. Rev. B* **2016**, *93* (16), 161116.

(17) Y. Yuan, H. Feng, Y. Shi, Y. Tsujimoto, A. A. Belik, Y. Matsushita, M. Arai, J. He, M. Tanaka, K. Yamaura. High-Pressure Synthesis, Crystal Structure, and Magnetic Properties of $KSbO_3$-Type 5d Oxides $K_{0.84}OsO_3$ and $Bi_{2.93}Os_3O_{11}$. *Sci. Technol. Adv. Mater.* **2014**, *15* (6), 064901.

(18) N. E. Brese, M. O'Keeffe. Bond-Valence Parameters for Solids. *Acta Cryst B* **1991**, *47* (2), 192–197.

(19) H. Feng, P. Adler, M. Reehuis, W. Schnelle, P. Pattison, Andreas Hoser, Claudia Felser, Martin Jansen. High-Temperature Ferrimagnetism with Large Coercivity and Exchange Bias in the Partially Ordered 3d/5d Hexagonal Perovskite $Ba_2Fe_{1.12}Os_{0.88}O_6$. *Chem. Mater.* **2017**, *29* (2), 886–895.

(20) Peter Adler, Vadim Ksenofontov, Avijit Kumar Paul, Manfred Reehuis, Binghai Yan, Martin Jansen, Claudia Felser. Magnetic Phase Transitions and Iron Valence in the Double Perovskite Sr_2FeOsO_6. *Hyperfine Interact* **2014**, *226* (1), 289–297.

(21) D. Sánchez, J. A. Alonso, M. García-Hernández, M. J. Martínez-Lope, J. L. Martínez, Anders Mellergård. Origin of Neutron Magnetic Scattering in Antisite-Disordered Sr_2FeMoO_6 Double Perovskites. *Phys. Rev. B* **2002**, *65* (10), 104426.

(22) Biswajit Dalal, Xun Kang, Yoshitaka Matsushita, Alexei A. Belik, Yoshihiro Tsujimoto, Kazunari Yamaura. Inverse Exchange Bias Effects and Magnetoelectric Coupling of the Half-Doped Perovskite-Type Chromites $Gd_{0.5}Sr_{0.5}CrO_3$ and $Gd_{0.5}Ca_{0.5}CrO_3$. *Phys. Rev. B* **2022**, *106* (10), 104425.

(23) Zheng Deng, Xiao Wang, Mengqin Wang, Feiran Shen, Jine Zhang, Yuansha Chen, Hai L. Feng, Jiawang Xu, Yi Peng, Wenmin Li, Jianfa Zhao, Xiancheng Wang, Manuel Valvidares, Sonia Francoual, Olaf Leupold, Zhiwei Hu, Liu Hao Tjeng, Man-Rong Li, Mark Croft, Ying Zhang, Enke Liu, Lunhua He, Fengxia Hu, Jirong Sun, Martha Greenblatt, Changqing Jin. Giant Exchange-Bias-Like Effect at Low Cooling Fields Induced by Pinned Magnetic Domains in Y_2NiIrO_6 Double Perovskite. *Advanced Materials* **2023**, *35* (17), 2209759.

(24) Sanghoon Kim, Sachin Pathak, Sonny H. Rhim, Jongin Cha, Soyoung Jekal, Soon Cheol Hong, Hyun Hwi Lee, Sung-Hun Park, Han-Koo Lee, Jae-Hoon Park, Soogil Lee, Hans-Georg Steinrück, Apurva Mehta, Shan X. Wang, Jongill Hong. Giant Orbital Anisotropy with Strong Spin–Orbit Coupling Established at the Pseudomorphic Interface of the Co/Pd Superlattice. *Advanced Science* **2022**, *9* (24), 2201749.

(25) R. Morrow, K. Samanta, T. Saha D., J. Xiong, J. W. Freeland, D. Haskel, P. M. Woodward. Magnetism in Ca_2CoOsO_6 and Ca_2NiOsO_6: Unraveling the Mystery of Superexchange Interactions between 3d and 5d Ions. *Chem. Mater.* **2016**, *28* (11), 3666–3675.

(26) Brendan J. Kennedy, Qingdi Zhou, Maxim Avdeev. The Ferroelectric Phase of $CdTiO_3$: A Powder Neutron Diffraction Study. *Journal of Solid State Chemistry* **2011**, *184* (11), 2987–2993.

(27) Geneva Laurita, Daniel Hickox-Young, Samra Husremovic, Jun Li, Arthur W. Sleight, Robin Macaluso, James M. Rondinelli, Mas A. Subramanian. Covalency-Driven Structural Evolution in the Polar Pyrochlore Series $Cd_2Nb_2O_{7-x}$. *Chem. Mater.* **2019**, *31* (18), 7626–7637.

(28) Man-Rong Li, Peter W. Stephens, Maria Retuerto, Tapati Sarkar, Christoph P. Grams, Joachim Hemberger, Mark C. Croft, David Walker, Martha Greenblatt. Designing Polar and Magnetic Oxides: Zn_2FeTaO_6 - in Search of Multiferroics. *J. Am. Chem. Soc.* **2014**, *136* (24), 8508–8511.

(29) K.-I. Kobayashi, T. Kimura, H. Sawada, K. Terakura, Y. Tokura. Room-Temperature Magnetoresistance in an Oxide Material with an Ordered Double-Perovskite Structure. *Nature, Volume 395, Issue 6703, pp. 677-680 (1998).* **1998**, *395*, 677–680.

(30) D. Serrate, J. M. De Teresa, M. R. Ibarra. Double Perovskites with Ferromagnetism above Room Temperature. *J. Phys.: Condens. Matter* **2006**, *19* (2), 023201.

(31) Mark T. Anderson, Kevin B. Greenwood, Gregg A. Taylor, Kenneth R. Poeppelmeier. B-Cation Arrangements in Double Perovskites. *Progress in Solid State Chemistry* **1993**, *22* (3), 197–233.

(32) Y. Krockenberger, K. Mogare, M. Reehuis, M. Tovar, M. Jansen, G. Vaitheeswaran, V. Kanchana, F. Bultmark, Anna Delin, F. Wilhelm, A. Rogalev, A. Winkler, L. Alff. Sr_2CrOsO_6 : End Point of a Spin-Polarized Metal-Insulator Transition by 5d Band Filling. *Physical Review B. Condensed Matter and Materials Physics* **2007**, *75* (2).

(33) J. Gopalakrishnan, A. Chattopadhyay, S. B. Ogale, T. Venkatesan, R. L. Greene, A. J. Millis, K. Ramesha, B. Hannoyer, G. Marest. Metallic and Nonmetallic Double Perovskites: A Case Study of A_2FeReO_6(A= Ca, Sr, Ba). *Phys. Rev. B* **2000**, *62* (14), 9538–9542.

(34) K. Ramesha, L. Sebastian, B. Eichhorn, J. Gopalakrishnan. Pb_2FeReO_6: New Defect Pyrochlore Oxide with a Geometrically Frustrated Fe/Re Sublattice. *J. Mater. Chem.* **2003**, *13* (8), 2011–2014.

(35) K.-I. Kobayashi, T. Kimura, Y. Tomioka, H. Sawada, K. Terakura, Y. Tokura. Intergrain Tunneling Magnetoresistance in Polycrystals of the Ordered Double Perovskite Sr_2FeReO_6. *Phys. Rev. B* **1999**, *59* (17), 11159–11162.

(36) Ikuya Yamada, Akihiko Takamatsu, Naoaki Hayashi, Hidekazu Ikeno. Covalency Competition in the Quadruple Perovskite $CdCu_3Fe_4O_{12}$. *Inorg. Chem.* **2017**, *56* (15), 9303–9310.

(37) R. S. Perry, H. Kurebayashi, A. Gibbs, M. J. Gutmann. Crystal Structure and Crystal Growth of the Polar Ferrimagnet $CaBaFe_4O_7$. *Phys. Rev. Mater.* **2018**, *2* (5), 054403.

(38) X. Kang, A. A. Belik, Y. Tsujimoto, K. Yamaura. High-Pressure Synthesis and Magnetic and Electrical Properties of Fe-Doped $Bi_3Re_3O_{11}$ and $Bi_3Os_3O_{11}$. *Inorg. Chem.* **2022**.

(39) Kousuke Nishimura, Masaki Azuma, Shigeto Hirai, Mikio Takano, Yuichi Shimakawa. Synthesis and Physical Properties of Double Perovskite Pb_2FeReO_6. *Inorg. Chem.* **2009**, *48* (13), 5962–5966.

(40) Saburo Nasu. General Introduction to Mössbauer Spectroscopy. In *Mössbauer Spectroscopy: Tutorial Book*; Yoshida, Y., Langouche, G., Eds.; Springer: Berlin, Heidelberg, 2013; pp 1–22.

(41) M. Retuerto, M. Li, P. W. Stephens, J. Sánchez-Benítez, X. Deng, Gabriel Kotliar, Mark C. Croft, Alexander Ignatov, David Walker, Martha Greenblatt. Half-Metallicity in Pb_2CoReO_6 Double Perovskite and High Magnetic Ordering Temperature in Pb_2CrReO_6 Perovskite. *Chem. Mater.* **2015**, *27* (12), 4450–4458.

(42) K. Oikawa, T. Kamiyama, H. Kato, Y. Tokura. Structural Distortion on Metal–Insulator Transition in Ordered Double Perovskite Ca_2FeReO_6. *J. Phys. Soc. Jpn.* **2003**, *72* (6), 1411–1417.

(43) W. Prellier, V. Smolyaninova, Amlan Biswas, C. Galley, R. L. Greene, K. Ramesha, J. Gopalakrishnan. Properties of the Ferrimagnetic Double Perovskites A_2FeReO_6 (A = Ba and Ca). *J. Phys.: Condens. Matter* **2000**, *12* (6), 965.

(44) Zahida Malik, Andriy Grytsiv, H. Michor, Gerda Rogl, S. Puchegger, H. Müller, Martin Kriegisch, Ernst Bauer, C. Eisenmenger-Sittner, Peter Rogl. Physical Properties of the Ternary Borides $Ni_{21}Zn_2B_{20}$ and Ni_3ZnB_2. *Journal of Alloys and Compounds* **2013**, *550*, 302–307.

(45) Jiaoyan Shen, Jingming Zhou, Meng Zhao, Guo-zhen Liu, Ju Gao, Jinlei Yao Stoner. Enhanced Paramagnetism in Tungsten Tetraboride. *Journal of physics. Condensed matter : an Institute of Physics journal* **2015**, *28*, 026005.

(46) M. Li, M. Retuerto, Z. Deng, P. W. Stephens, M. Croft, Q. Huang, H. Wu, X. Deng, G. Kotliar, J. Sánchez-Benítez, J. Hadermann, D. Walker, M. Greenblatt. Giant Magnetoresistance in the Half-Metallic Double-Perovskite Ferrimagnet Mn_2FeReO_6. *Angewandte Chemie International Edition* **2015**, *54* (41), 12069–12073.

(47) B. C. Jeon, Choong H. Kim, S. J. Moon, Woo Seok Choi, Hogyun Jeong, Y. S. Lee, J. Yu, C. J. Won, J. H. Jung, N. Hur, T. W. Noh. Electronic Structure of Double Perovskite A_2FeReO_6 (A = Ba and Ca): Interplay between Spin-Orbit Interaction, Electron Correlation, and Lattice Distortion. *J Phys Condens Matter* **2010**, *22* (34), 345602.

(48) Abhijit S. Ogale, S. B. Ogale, R. Ramesh, T. Venkatesan. Octahedral Cation Site Disorder Effects on Magnetization in Double-Perovskite Sr_2FeMoO_6: Monte Carlo Simulation Study. *Appl. Phys. Lett.* **1999**, *75* (4), 537–539.

(49) Hai L. Feng, Madhav Prasad Ghimire, Zhiwei Hu, Sheng-Chieh Liao, Stefano Agrestini, Jie Chen, Yahua Yuan, Yoshitaka Matsushita, Yoshihiro Tsujimoto, Yoshio Katsuya, Masahiko Tanaka, Hong-Ji Lin, Chien-Te Chen, Shih-Chang Weng, Manuel Valvidares, Kai Chen, Francois Baudelet, Arata Tanaka, Martha Greenblatt, Liu Hao Tjeng, Kazunari Yamaura. Room-Temperature Ferrimagnetism of Anti-Site-Disordered Ca_2MnOsO_6. *Phys. Rev. Materials* **2019**, *3* (12), 124404.

(50) W. Westerburg, O. Lang, C. Ritter, C. Felser, W. Tremel, G. Jakob. Magnetic and Structural Properties of the Double-Perovskite Ca_2FeReO_6. *Solid State Communications* **2002**, *122* (3), 201–206.

(51) Masanori Abe, Takehiko Nakagawa, Shōichiro Nomura. Magnetic and Mössbauer Studies of the Ordered Perovskites $Sr_2Fe_{1+x}Re_{1-x}O_6$. *J. Phys. Soc. Jpn.* **1973**, *35* (5), 1360–1365.

(52) E. Granado, J. C. Cezar, C. Azimonte, J. Gopalakrishnan, K. Ramesha. Electronic Structure of Fe and Magnetism in the 3d/5d Double Perovskites Ca_2FeReO_6 and Ba_2FeReO_2. *Phys. Rev. B* **2019**, *99* (19), 195118.

(53) Ji Zhang, Wei-Jing Ji, Jie Xu, Xiao-Yu Geng, Jian Zhou, Zheng-Bin Gu, Shu-Hua Yao, Shan-Tao Zhang. Giant Positive Magnetoresistance in Half-Metallic Double-Perovskite Sr_2CrWO_6 Thin Films. *Science Advances* **2017**.

(54) Zhao-Cai Wang, Lei Chen, Shuang-Shuang Li, Jing-Shi Ying, F. Tang, Guan-Yin Gao, Y. Fang, Weiyao Zhao, David Cortie, Xiaolin Wang, Ren-Kui Zheng. Giant Linear Magnetoresistance in Half-Metallic Sr_2CrMoO_6 Thin Films. *npj Quantum Materials* **2021**, *6* (1), 1–8.

(55) Xiaolin Wang, Yi Du, Shixue Dou, Chao Zhang. Room Temperature Giant and Linear Magnetoresistance in Topological Insulator Bi_2Te_3 Nanosheets. *Phys. Rev. Lett.* **2012**, *108* (26), 266806.

(56) A. Narayanan, M. D. Watson, S. F. Blake, N. Bruyant, L. Drigo, Y. L. Chen, D. Prabhakaran, B. Yan, C. Felser, T. Kong, P. C. Canfield, A. I. Coldea. Linear Magnetoresistance Caused by Mobility Fluctuations in Doped Cd_3As_2. *Phys. Rev. Lett.* **2015**, *114* (11), 117201.

(57) Xiaochun Huang, Lingxiao Zhao, Yujia Long, Peipei Wang, Dong Chen, Zhanhai Yang, Hui Liang, Mianqi Xue, Hongming Weng, Zhong Fang, Xi Dai, Genfu Chen. Observation of the Chiral-Anomaly-Induced Negative Magnetoresistance in 3D Weyl Semimetal TaAs. *Phys. Rev. X* **2015**, *5* (3), 031023.

(58) Mario Novak, Satoshi Sasaki, Kouji Segawa, Yoichi Ando. Large Linear Magnetoresistance in the Dirac Semimetal TlBiSSe. *Phys. Rev. B* **2015**, *91* (4), 041203.

Chapter 4 High-pressure synthesis and magnetic and electrical properties of Fe-doped $Bi_3Re_3O_{11}$ and $Bi_3Os_3O_{11}$

4.1. Introduction

ABO_3 compounds form a series of interesting crystal structures, including perovskite, ilmenite, corundum, pyroxene, and $KSbO_3$-type.[1] Among them, $KSbO_3$-type oxides have diverse and attractive properties such as ionic conductivity and electrocatalysis in $Bi_3Ru_3O_{11}$,[2,3] remarkable non-Fermi-liquid behavior in structurally related $La_4Ru_6O_{19}$,[4] and the highest T_c record of 307 K among insulating and semiconducting ferromagnets in $Bi_3Mn_3O_{11.6}$ [5]. As a result, $KSbO_3$-type compounds, together with perovskite oxides, have attracted a great deal of attention in recent years.

In the $KSbO_3$-type structure, Sb_2O_{10} dimers sharing corners and edges form a three-dimensional framework, which is filled with different units, thus forming various lattices with different space groups.[6] For example, the K atoms in $KSbO_3$ and the Bi_3O_2 units in $Bi_3Ru_3O_{11}$ are regularly arranged in the channel, forming the *Pn*-3 lattice,[5] while the K atoms in $KBiO_3$ [7] and Sr atoms in $Sr_2Re_3O_9$ [8] result in the *Im*-3 lattice. Meanwhile, the La_4O units in $La_4M_6O_{19}$-type compounds (*M*: metal atom),[8] which are usually off-stoichiometric, form the *I*23 lattice.[4,9] $Bi_3M_3O_{11}$ compounds, which are usually cubic with the space group of *Pn*-3, form the largest family of $KSbO_3$-type oxides. This was likely due to the propensity of Bi atoms to form structures with various counter elements. To the best of our knowledge, the following bismuth-based $KSbO_3$-type oxides have been synthesized: $Bi_3Ru_3O_{11}$,[2] $Bi_3Os_3O_{11}$,[3] $Bi_3Re_3O_{11}$,[8] $Bi_3Ge_3O_{10.5}$,[10] $Bi_3Cr_{2.91}O_{11}$,[11] $Bi_3Mn_3O_{11+\delta}$ ($-0.5 \leq \delta \leq 0.6$),[5,12] $Bi_3Mn_{1.9}Te_{1.1}O_{11}$,[13] $Bi_3CrSb_2O_{11}$,[14] $Bi_3FeSb_2O_{11}$,[14] $Bi_2LaFeSb_2O_{11}$,[14] $Bi_2LaMnSb_2O_{11}$,[14] $Bi_2LaCrSb_2O_{11}$,[14] $NaBi_2Sb_3O_{11}$,[15] and $Bi_6Ti_5WO_{22}$,[16] $Bi_9Ni_2Sb_7O_{33}$.[17] However, all but $Bi_3Mn_3O_{11+\delta}$ and $Bi_3Cr_{2.91}O_{11}$ are paramagnetic and show no long-range magnetic ordering down to low temperature. In particular, 5d oxides show only weak temperature-dependent paramagnetism in the temperature range.

In recent years, combining 5d and 3d (or 4d and 3d) transition metals in materials has become a proven way to explore useful new magnetic and magnetoelectric properties; for example, Sr_2FeMoO_6 exhibits colossal magnetoresistance at room temperature,[18,19] Sr_2FeReO_6

shows half-metal properties with a Curie temperature above 400 K,[20] Sr_2CrOsO_6 has the highest ferrimagnetic ordering temperature (725 K) among double-perovskite oxides,[21,22] and Ca_2FeOsO_6 exhibits room-temperature ferrimagnetism due to structural distortion.[23,24] Since doping of 3d elements into 5d or 4d element sites is promising for the design of new magnetic materials, this study aims to replace some of the 5d elements in $KSbO_3$-type oxides with 3d elements to explore and develop electronic properties and materials for spintronics and related device research fields. Specifically, because rhenates such as Mn_2FeReO_6[25,26] and Mn_2MnReO_6 [27] and osmates such as $LiOsO_3$ [28] and $NaOsO_3$ [29] exhibit remarkable 5d properties, I selected $KSbO_3$-type $Bi_3Re_3O_{11}$ and $Bi_3Os_3O_{11}$ as target materials (both are paramagnetic down to the minimum temperature) and investigated the possibility of improving material properties by doping with iron.

Consequently, I have successfully doped $Bi_3Re_3O_{11}$ and $Bi_3Os_3O_{11}$ with Fe up to 29 atomic% using high-temperature and high-pressure conditions. Herein, I report on the synthesis, crystal structures, and magnetic and electrical properties of the maximally doped $Bi_3Re_{2.13}Fe_{0.87}O_{11}$ and $Bi_3Os_{2.45}Fe_{0.55}O_{11}$. In particular, I find that $Bi_3Os_{2.45}Fe_{0.55}O_{11}$ exhibits magnetic characteristics at 490 K, the highest temperature ever reported for a $KSbO_3$-type material.

4.2. Experimental

Polycrystalline materials were synthesized via a solid-state reaction under high-pressure and high-temperature conditions. Early in the synthesis, attempts were made to replace 1/3 of the Re (or Os) in $Bi_3Re_3O_{11}$ (or $Bi_3Os_3O_{11}$) with Fe, but because of the formation of impurity phases in the final product, the composition ratios were adjusted to minimize them, and eventually the purest material was obtained in the following ratio. $Bi_3Re_{2.13}Fe_{0.87}O_{11}$ was synthesized from a mixture of Bi_2O_3 (99.99%, Soekawa Chem), Fe_2O_3 (99.998%, Alfa Aesar), ReO_3 (laboratory made from 99.99% Re, Rare Metallic Co. Ltd.), and Re (99.99%, Rare Metallic Co. Ltd.) in the ratio of 3:2:3.14:0.46, which was thoroughly ground and sealed in an Au capsule. The capsule was incorporated into a multi-anvil high-pressure apparatus (CTF-MA1500P; C&T Factory Co., Ltd., Tokyo, Japan) and heated at 900 °C for 40 min under a pressure of 6 GPa. After heating, the capsule was quenched below 100 °C within 30 s and the pressure was gradually released over several hours to obtain the target material. Another osmium oxide was obtained using the same procedure. The differences were that the mixing procedure was performed in a glove box filled with Ar, and the raw materials for $Bi_3Os_{2.45}Fe_{0.55}O_{11}$ were Bi_2O_3 (99.99%, Soekawa Chem), Fe_2O_3 (99.998%, Alfa Aesar), OsO_2 (laboratory made from 99.95% Os, Nanjing Dongrui Platinum Co. Ltd.), and $KClO_4$ (99.5%, Kishida Chem) in a ratio of 3:0.75:5.6:0.94. Higher temperatures were required for the formation of osmium oxide, and the temperature was increased to 1100 °C. Syntheses with lower doping levels were also attempted, but in the end, it was very difficult to obtain pure single-phase materials. For example, at least two $KSbO_3$-type mixed phases with different Fe/Re ratios were obtained for the rhenium material, and significant pyrochlore impurities appeared in the osmium material. Since the exact phase relations were unknown, the purest materials were selected and the fundamental properties of the Fe-doped materials were investigated.

In the laboratory, X-ray diffraction (XRD) of the high-pressure products showed that trace impurities such as Fe_2O_3, Fe_3O_4, and KCl remained; therefore, the products were washed repeatedly with HCl and distilled water and dried at 120°C for 2 days.

Structural determination was performed using synchrotron X-ray diffraction (XRD). High-resolution synchrotron powder XRD data were obtained at room temperature using a monochromatized beam (λ = 0.413854 Å) at beamline BL02B2 at SPring-8, Japan.[30,31] Prior to the measurement, a benchmark test was performed using a standard (CeO_2) to confirm the wavelength. The powder was placed in a Lindenmann glass capillary (0.1 mm inner diameter) and rotated during measurement. The RIETAN-VENUS program was used to analyze the synchrotron XRD patterns.[32,33]

The temperature dependence of the direct current (DC) and alternating current (AC) magnetic susceptibilities was measured using a magnetometer (MPMS3, Quantum Design Inc, San Diego, California) at temperatures between 2 K and 550 K, an applied magnetic field of 10 kOe, and zero-field cooling (ZFC) and magnetic field cooling (FC) conditions. Isothermal magnetization curves were also measured in the -70 to 70 kOe field range. Magneto-transport properties were recorded using a four-probe method between 2 K and 300 K in magnetic fields up to 90 kOe using a physical property measurement system (PPMS, Quantum Design). The specific heat (C_p) was measured by the relaxation method between 2 and 300 K using grease (N Apiezon) and the commercial calorimeter option of PPMS.

To determine the exact metal composition of the high-pressure products, electron probe microanalysis (EPMA) was performed using a JEOL JXA-8500F instrument. The sintered surfaces were precisely polished with a 0.3μm alumina-coated film.

4.3. Results and discussion

4.3.1. Determination of the chemical composition and crystal structure

The synchrotron XRD patterns of $Bi_3Re_{2.13}Fe_{0.87}O_{11}$ and $Bi_3Os_{2.45}Fe_{0.55}O_{11}$ are shown in **Figure 4.1.** Except for the identified trace impurities (2.4 wt% $BiFeO_3$ in $Bi_3Re_{2.13}Fe_{0.87}O_{11}$ and 2.2 wt% OsO_2 in $Bi_3Os_{2.45}Fe_{0.55}O_{11}$), the samples are single phase and all diffraction peaks are indexed based on a $KSbO_3$-type structure (space group *Pn*-3). The cubic lattice constant of $Bi_3Re_{2.13}Fe_{0.87}O_{11}$ was a = 9.40771(8) Å and that of $Bi_3Os_{2.45}Fe_{0.55}O_{11}$ was a = 9.38007(3) Å. Rietveld refinement revealed that Bi atoms completely occupied the 8*e*(*x*, *x*, *x*) and 4*b*(0, 0, 0) Wyckoff positions, Fe and Re (Os) atoms were randomly placed at the 12 *g* position, and O atoms were distributed at independent 8*e*(*x*, *x*, *x*), 12*f*(*x*, 0.25, 0.25), and 24*h*(*x*, *y*, *z*) positions. The final crystallographic parameters are presented in **Table 4.1.** During the analysis, the constraint occupancy(Fe) + occupancy(Re/Os) = 1 was imposed on the Fe and Re(Os) sites. The resulting Re/Fe ratio was approximately 0.27/0.73, which is in close agreement with the Re/Fe = 0.29/0.71 obtained by EPMA. However, it was fixed to the EPMA ratio. On the other hand, the Os/Fe ratio was quite unstable during the analysis but was finally fixed at 0.18/0.82 based on the EPMA results.

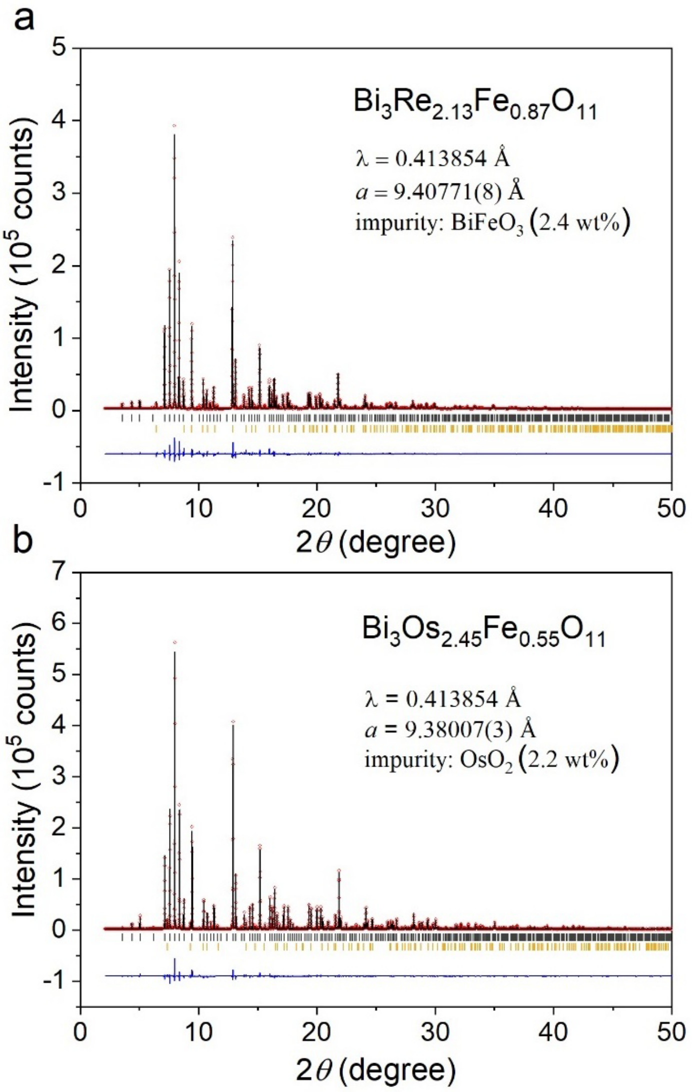

Figure 4.1. Rietveld analysis of synchrotron XRD patterns of (a) $Bi_3Re_{2.13}Fe_{0.87}O_{11}$ with $BiFeO_3$ as the impurity phase and (b) $Bi_3Os_{2.45}Fe_{0.55}O_{11}$ with OsO_2 as the impurity phase at room temperature. Observed (circles), calculated (all lines), and difference profiles (bottom). The array of short vertical bars represents the calculated positions of the diffraction peaks by the structural model.

Table 4.1 Structure Parameters of $Bi_3Re_{2.13}Fe_{0.87}O_{11}$ and $Bi_3Os_{2.45}Fe_{0.55}O_{11}$

Atom	Wyckoff	*g*	*x*	*y*	*z*	*B* (Å^2)
			$Bi_3Re_{2.13}Fe_{0.87}O_{11}$			
Bi1	8*e*	1	0.38206(7)	= *x*	= *x*	1.670(22)
Bi2	4*b*	1	0	0	0	1.599(27)
Re1/Fe1	12*g*	0.29/0.71	0.38762(12)	0.75	0.25	0.349(13)

O1	8*e*	1	0.1439(9)	= *x*	= *x*	1
O2	12*f*	1	0.5900(14)	0.25	0.25	1
O3	24*h*	1	0.6022(10)	0.2444(8)	0.5405(14)	1
$Bi_3Os_{2.45}Fe_{0.55}O_{11}$						
Bi1	8*e*	1	0.38179(4)	= *x*	= *x*	1.356(12)
Bi2	4*b*	1	0	0	0	1.173(13)
Os1/Fe1	12*g*	0.18/0.82	0.38977(6)	0.75	0.25	0.207(5)
O1	8*e*	1	0.1448(6)	= *x*	= *x*	1
O2	12*f*	1	0.5933(9)	0.25	0.25	1
O3	24*h*	1	0.6023(8)	0.2443(6)	0.5384(10)	1

Note. The space group was *Pn*-3 (no. 201) at origin choice 2, $Z = 4$, and g was the occupation factor. $Bi_3Re_{2.13}Fe_{0.87}O_{11}$: $a = 9.40771(8)$ Å and $V = 832.629(12)$ Å^3. *R* Indices are $R_{wp} = 9.38\%$, $R_p = 6.357\%$, $R_B = 4.335\%$, and $R_F = 2.982\%$. $Bi_3Os_{2.45}Fe_{0.55}O_{11}$: $a = 9.38007(3)$ Å and $V = 825.313(4)$ Å^3. *R* Indices are $R_{wp} = 6.80\%$, $R_p = 4.83\%$, $R_B = 3.26\%$, and $R_F = 2.19\%$.

The crystal structures of $Bi_3Re_{2.13}Fe_{0.87}O_{11}$ and $Bi_3Os_{2.45}Fe_{0.55}O_{11}$ were almost identical; therefore, only one is depicted here to prevent duplication (**Figure 4.2.**). The Bi atoms are not shown for clarity. The structural view clearly shows the characteristic tunneling motif, as observed in other $KSbO_3$-type oxides: the Re(Os)/Fe atoms occupy the octahedral center, and the $[Re(Os)/Fe]_2O_{10}$ dimer is composed of edge-sharing octahedral pairs, with adjacent dimers located in a vertical plane to form O3 corner sharing, thereby linking them into a geometrically frustrated 3D network.

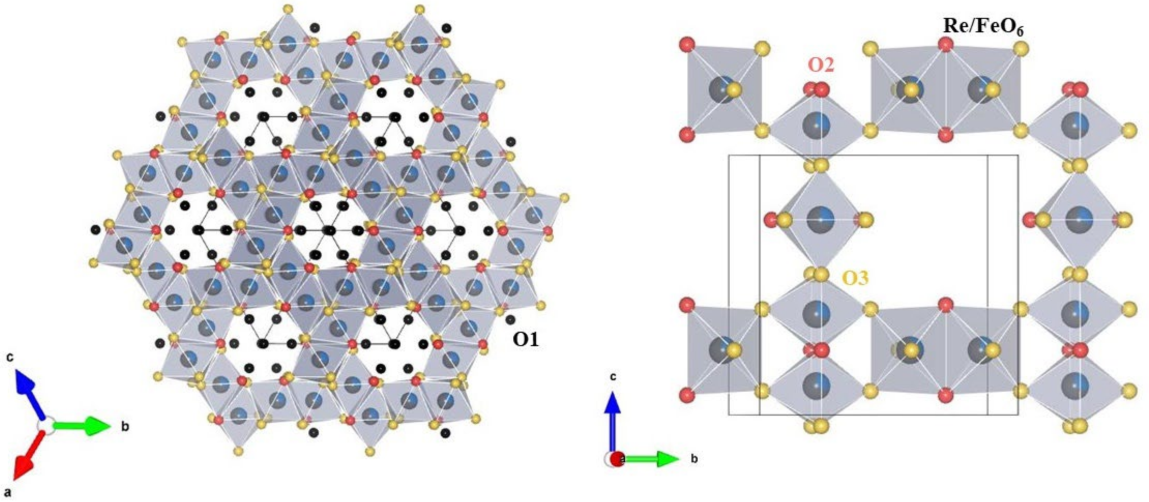

Figure 4.2. (upper) Crystal structure of $Bi_3Re_{2.13}Fe_{0.87}O_{11}$ viewed in the <111> direction, and (lower, slightly tilted toward the a-axis) a bc-plane showing connections between $(Re/Fe)O_6$ octahedra. For clarity, Bi atoms are not shown.

Due to the close proximity of the octahedra, the Os(Fe)-Os(Fe) and Re(Fe)-Re(Fe) distances were found to be short (2.658 Å and 2.602 Å, respectively). The values for osmium oxide are close to the bond length of undoped $Bi_{2.93}Os_3O_{11}$ (2.6610 Å),[34] suggesting that a metallic bond is formed. The Re(Fe)-Re(Fe) distance is longer than the distance for $Bi_3Re_3O_{11}$ (2.456 Å),[8] but since it is shorter than the Os-Os bond distance (2.6610 Å),[34] it is inferred that metallic bonding is also involved in the chemical bonding of $Bi_3Re_{2.13}Fe_{0.87}O_{11}$.

Table 4.2. shows the bond lengths, angles, and bond valence sums (BVS) for each oxide; since I have not obtained a single crystal, the accurate Fe-O and Re(Os)-O bond lengths could not be measured precisely, therefore I can only use the average bond lengths from the polycrystalline results to make an overall estimate. The BVS values for the Bi sites are comparable to the 3.00 for Bi expected for the stoichiometric $Bi_3M_3O_{11}$. This result indicates the effectiveness of the BVS for these oxides. Assuming a valence of +3.00 for the Fe ions doped in each oxide, the BVS for Re is expected to be 4.88 and 4.63 for Os. However, the BVS values for Fe (3.24 of $Bi_3Re_{2.13}Fe_{0.87}O_{11}$ and 3.35 of $Bi_3Os_{2.45}Fe_{0.55}O_{11}$) were slightly higher than expected. However, the BVS values for Re and Os (Re = 4.87; Os = 4.50) are close to the expected values. It is possible that Fe is overbonded, although the effect of metallic bonding must be considered. This complex bonding state may be the consequence of a delicate stress balance between the compression and tension inside the crystal structure, which is stabilized by high-pressure heating.

Table 4.2. Selected bond lengths, angles, and bond balance sums (BVS) of $Bi_3Re_{2.13}Fe_{0.87}O_{11}$ and $Bi_3Os_{2.45}Fe_{0.55}O_{11}$ at room temperature.

	$Bi_3Re_{2.13}Fe_{0.87}O_{11}$		$Bi_3Os_{2.45}Fe_{0.55}O_{11}$
Bi1–O1 (×3)	2.267(9)	Bi1–O1 (×3)	2.251(6)
Bi1–O2 (×3)	2.629(11)	Bi1–O2 (×3)	2.644(7)
Bi1–O3 (×3)	2.862(11)	Bi1–O3 (×3)	2.846(8)
BVS (Bi1)	2.96	BVS (Bi1)	3.03
Bi2–O1 (×2)	2.345(5)	Bi2–O1 (×2)	2.353(4)
Bi2–O3 (×6)	2.521(9)	Bi2–O3 (×6)	2.511(6)
BVS (Bi2)	2.91	BVS (Bi2)	2.95
Re/Fe–O2 (×2)	1.986(11)	Os/Fe–O2 (×2)	1.970(7)
Re/Fe–O3 (×2)	1.974(14)	Os/Fe–O3 (×2)	1.966(9)
Re/Fe–O3 (×2)	2.001(12)	Os/Fe–O3 (×2)	1.987(10)

BVS (Fe)	3.24	BVS (Fe)	3.35
BVS (Re)	4.87	BVS (Os)	4.50
O3–Re/Fe–O2	90.6(3)	O3–Os/Fe–O2	86.9(3)
O3–Re/Fe–O3	85.4(5)	O3–Os/Fe–O3	85.9(4)
O3–Re/Fe–O3	90.6(5)	O3–Os/Fe–O3	91.1(4)
O3–Re/Fe–O2	93.0(3)	O3–Os/Fe–O2	96.5(4)
O3–Re/Fe–O2	86.7(5)	O3–Os/Fe–O2	92.6(2)
O3–Re/Fe–O3	88.1(7)	O3–Os/Fe–O3	89.7(5)
O2–Re/Fe–O2	98.6(6)	O2–Os/Fe–O2	90.3(2)
O2–Re/Fe–O3	174.5(5)	O2–Os/Fe–O3	176.2(3)
O3–Re/Fe–O3	174.5(6)	O3–Os/Fe–O3	175.7(5)

Note. BVS = $\sum_{i=1}^{N} v_i$, v_i = exp[(R_0–l_i)/B], N is the coordination number, B = 0.37, $R_0(\mathrm{B_i}^{3+})$ = 2.094,[35] $R_0(\mathrm{F_e}^{3+})$ = 1.759,[35] $R_0(\mathrm{Os}^{5+})$ = 1.868,[34] $R_0(\mathrm{Re}^{5+})$ = 1.86.[36]

4.3.2 Magnetic properties

The magnetic properties of polycrystalline $Bi_3Re_{2.13}Fe_{0.87}O_{11}$ were investigated. Figure 3a shows the temperature dependence of magnetic susceptibility on an applied magnetic field of 10 kOe. Clearly, the magnetic susceptibility increased with decreasing temperature, and the ZFC and FC curves diverged below 22 K. This suggests competition between the different magnetic interactions or spin frustration inside the material. At higher temperatures, a Curie-Weiss fit of the inverse of the susceptibility in the paramagnetic region (250 ~ 350 K) yields an effective magnetic moment of 5.48 μ_B per $Re_{2.13}Fe_{0.87}$ and a large negative Weiss temperature (θ_w) = -222.38 K. The theoretically predicted spin-only moment is 8.55 μ_B per $Re_{2.13}Fe_{0.87}$, so the observed moment is underestimated, possibly because of the large spin-orbit interaction of Re.[37] The Weiss temperature suggests that the magnetic interactions are predominantly antiferromagnetic (AFM).

In **Figure 4.3.**, the magnetization-field plot at 5 K shows a hysteresis loop, indicating a ferrimagnetic (FIM) or spin glass (SG) state rather than an AFM state. At 50 K and 100 K, the material was predominantly paramagnetic. AC magnetic susceptibility measurements were performed to elucidate its magnetic nature, and the susceptibility $\chi'(T)$ as a function of temperature at several frequencies in an AC magnetic field of 8 Oe is shown in Fig. 3c. There is clearly a frequency dependency near the phase-transition point. As the frequency increased, the peak shifted toward higher temperatures and its magnitude decreased. When T_f is considered as the freezing temperature, the physical quantity p [= $T_f\Delta/(T_f\Delta\log f)$], which is usually determined by the peak shift, can be applied to characterize the glassy behavior. In the case of $Bi_3Re_{2.13}Fe_{0.87}O_{11}$, the value of p was approximately 0.0489, which is in the region of typical SG systems (p =0.0045–0.08).[38] It can be concluded that the spin glassy behavior rather than the FIM transition is more likely to be involved in this material.

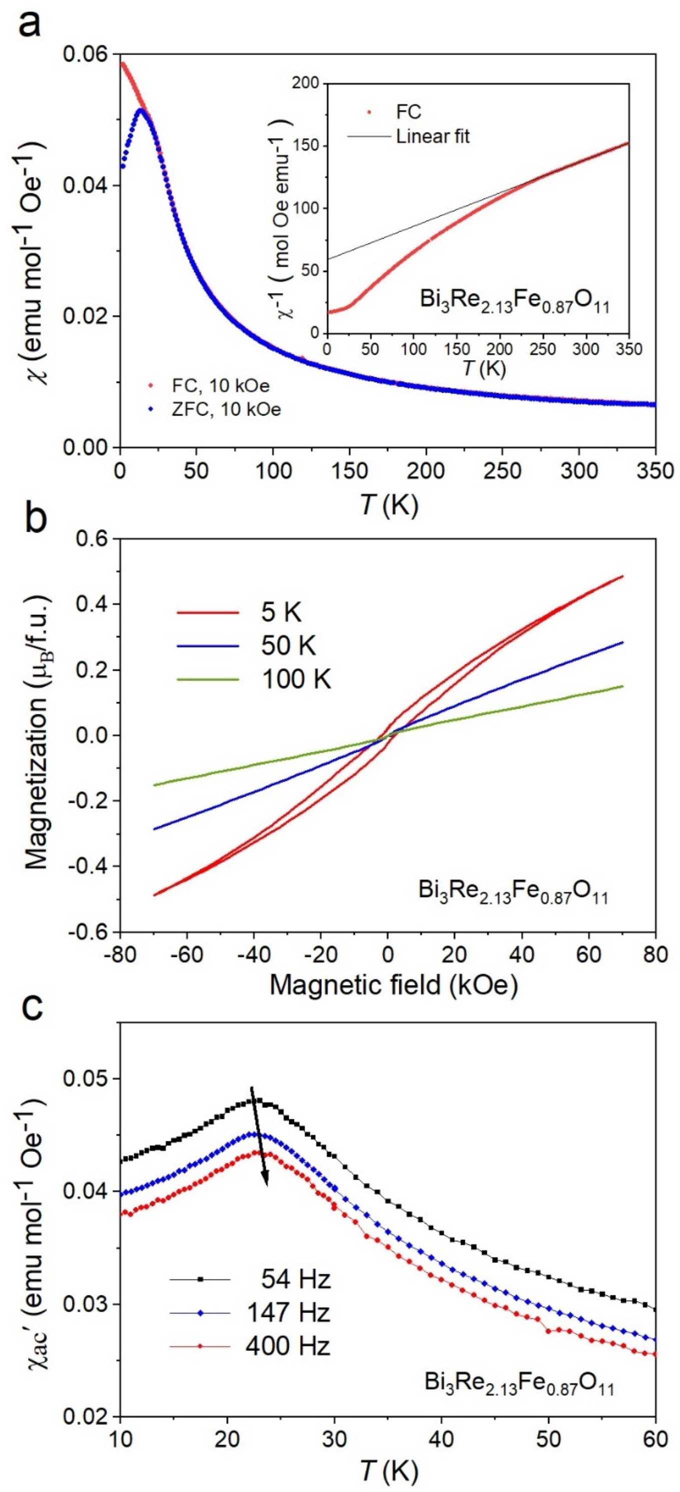

Figure 4.3. (a) Temperature dependence of χ and χ^{-1} (inset) of $Bi_3Re_{2.13}Fe_{0.87}O_{11}$ measured at H = 10 kOe (b) Isothermal magnetization curves of $Bi_3Re_{2.13}Fe_{0.87}O_{11}$ at 5, 50, and 100 K. (c) Real part of the AC χ of $Bi_3Re_{2.13}Fe_{0.87}O_{11}$ (χ' vs. T). Measurements were made at zero DC field with cooling from 60 to 10 K using an AC magnetic field of 8 Oe and different frequencies (f = 54, 147, 400 Hz).

Figure 4.4a shows the temperature dependence of the magnetic susceptibility of $Bi_3Os_{2.45}Fe_{0.55}O_{11}$ at 10 kOe. Because the FC and ZFC curves diverged even as the temperature increased to 350 K, the magnetic susceptibility was examined above this temperature using the oven mode of MPMS3. It can be found that the divergence persisted until approximately 490 K, after which susceptibility decreased, proving that the paramagnetic state had arrived. I also noticed that a gap exists between the measurements of the different modes: the gap in the ZFC curve is fairly small, whereas the gap in the FC curve is somewhat larger. Since magnetic field cooling took place before the Curie point was reached in the normal experiments, certain magnetic moments that naturally freeze below the Curie point are no longer freely aligned by the magnetic field, which is one explanation for the nontrivial gap in the FC curves.

Below 490 K, the magnetic susceptibility increased with temperature decreasing, and a broad kink was observed in the ZFC curve at approximately 250 K. Therefore, I varied the applied magnetic field and measured the ZFC curve up to 350 K again. When the applied magnetic field was reduced to 1 kOe, the broad peak became less noticeable, and no additional anomalies in the magnetic susceptibility measurement were observed. Therefore, the gradual increase was considered to be due to the inhomogeneity of the material, similar to the phenomenon observed in $Ba_2Fe_{1.12}Os_{0.88}O_6$.[39]

Owing to technical limitations and difficulties, measurements were performed only up to 550 K for the $Bi_3Os_{2.45}Fe_{0.55}O_{11}$. Therefore, the paramagnetic region is relatively narrow, and consequently, the thermal variation of the inverse susceptibility χ^{-1} and the Curie-Weiss fitting are not presented here.

Similar to the results obtained for $Bi_3Re_{2.13}Fe_{0.87}O_{11}$, AC magnetic susceptibility measurements at temperatures below 390 K were also performed to investigate the magnetic nature of $Bi_3Os_{2.45}Fe_{0.55}O_{11}$. As shown in **Figure 4.4b**, there is a clear frequency dependence of the χ' vs. T curve near T_f, suggesting the existence of a spin glassy behavior in this material. A possible reason for the emergence of glassy behavior is that, at low temperature, the inhibition of the thermal motion of spins are enhanced and the interatomic interactions become fierce and due to the geometrically frustrated $KSbO_3$-type structure, spins are less likely to remain the linear arrangement but more inclined to range randomly to form an irregular long-range disorder, which is the spin glass state. Again, the physical quantity p was estimated, and its value of 0.0448 falls within the classical spin glass range; the lack of measurements above 390 K is due to the fact that spin glassy behavior generally occurs at low temperatures.

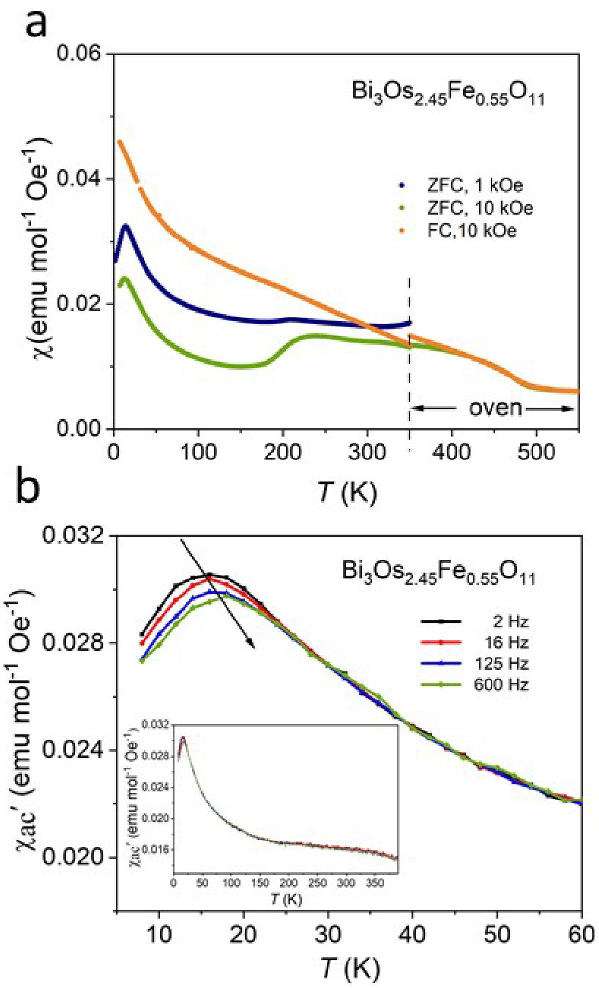

Figure 4.4. (a) Thermal evolution of χ for $Bi_3Os_{2.45}Fe_{0.55}O_{11}$ measured at $H = 1$ and10 kOe. (b) Real part (χ' vs T) of AC magnetic susceptibilities of $Bi_3Os_{2.45}Fe_{0.55}O_{11}$. Measurements were carried out at zero dc magnetic field and cooling from 390 to 7 K using $H_{ac} = 5$ Oe amplitude and different frequencies ($f = 2$, 16, 125, 600 Hz).

Figure 4.5a. shows the isothermal magnetization curves at several temperatures from 5 to 350 K to further investigate the nature of the transition. Below T_f(=16 K), an S-shape with small elongated hysteresis, typical of materials with SG-like magnetic properties, occurs. As previously mentioned, AC susceptibility measurements (**Figure 4.4b**) indicate that magnetic properties similar to those of an SG emerge in the temperature range. The hysteresis loop at room temperature shows a magnetic moment of approximately 0.06 μ_B/f.u at around 20 kOe.

This could be attributed to the coexistence of iron-related oxides, but the iron oxides had already been removed by hydrochloric acid immersion, and the only non-magnetic impurity, OsO_2, was identified at approximately 2 wt% by high-energy synchrotron radiation. Thus, quantitative discussions indicate that it is highly unlikely that unexpected magnetic impurities are responsible for magnetization; rather, it is due to the intrinsic properties of the main phase.

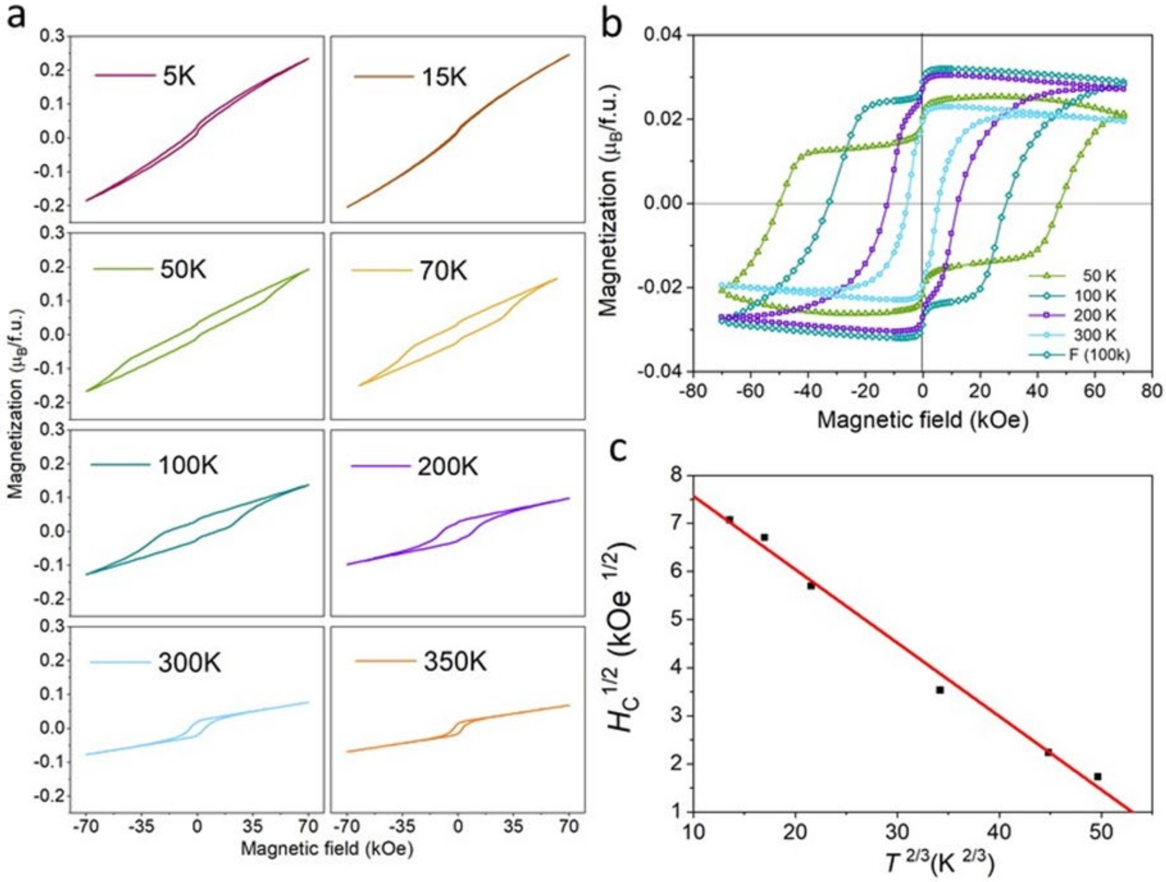

Figure 4.5. (a) Isothermal magnetization curves of $Bi_3Os_{2.45}Fe_{0.55}O_{11}$ between 5 to 350 K. (b) Hysteresis loops of $Bi_3Os_{2.45}Fe_{0.55}O_{11}$ with AFM contribution removed. (c) The linear relationship between $H_C^{1/2}$ and $T^{2/3}$.

Anomalous behavior is observed between T_f and room temperature. Below about 200 K, the loops become much stiffer upon cooling, but do not appear to be very large, and this phenomenon is not well understood. To better understand this peculiar problem, the hysteresis loops were treated as in the case of Mn_2LiReO_6.[40] That is, the linear AFM $M(H)$ response was subtracted from the data, as shown in **Figure 4.5b.** Several points should be noted in this regard. First, the maximum spontaneous moment decays with decreasing temperature: from 0.03 μ_B/f.u. at 100 K to 67% of that (0.02 μ_B/f.u.) at 50 K. Considering the glassy behavior due to the large magnetic frustration of the tunneling network, it is reasonable to attribute this unusual phenomenon to spin rearrangements that develop into the SG-like behavior, similar to the spin rearrangements observed, for example, in Mn_2NiReO_6.[41] Second, small steps occur in the low-field region near the origin; at 50 K, the magnetization (~0.021 μ_B/f.u.) decreases by about 30 % as the field direction changes, suggesting the existence of domain reorientation, as in Mn_2LiReO_6.[40] Third, the temperature dependence of the coercive force line H_C is plotted linearly between $H_C^{1/2}$ and $T^{2/3}$ in **Figure 4.5c.**, suggesting the presence of so-called strong magnetic wall pinning, which explains the large coercivity appearing in the material.

4.3.3 Electrical transport

Figure 4.6a shows that $Bi_3Os_{2.45}Fe_{0.55}O_{11}$ exhibits semiconducting behavior over the entire temperature range at $H = 0$ and 70 kOe. The magnetoresistance can be defined as $\mathrm{MR}(H) = 100\times[R(H)-R(0)]/R(0)$, and the inset shows a negative increase with increasing magnetic field, reaching a maximum value of -10% at 5 K and 90 kOe. This suggests that the suppression of spin fluctuations in an external high magnetic field contributes to a gradual decrease in the magnetoresistance and promotes transport. At room temperature, the resistivity is about 0.01 Ω•cm, and the resistivity increases with decreasing temperature. Plotting the data on a $T^{-1/4}$ scale, as shown in **Figure 4.6b**, reveals that the resistivity is nearly linear on the $T^{-1/4}$ scale. This is consistent with Mott's variable range hopping (VRH) conduction mechanism $\rho = \rho_0\exp[(T_0/T)^{1/4}]$, where the parameters ρ_0 and T_0 are extracted to be 1.67 μΩ•cm and 3266 K, respectively, by fitting the data.

Figure 4.6c shows the temperature dependence of ρ in the $Bi_3Os_{2.45}Fe_{0.55}O_{11}$. This feature is not consistent with the expectations for a semiconducting oxide with an energy gap, and the absence of a phase transition at approximately 250 K suggests that the true conductivity of $Bi_3Os_{2.45}Fe_{0.55}O_{11}$ may be masked by its polycrystalline nature, including resistive grain boundaries and impurities. Therefore, further studies using single crystals of this compound are needed to clarify the nature of the electrical conduction in $Bi_3Os_{2.45}Fe_{0.55}O_{11}$. Attempts to obtain single crystals under high-temperature and high-pressure conditions have been unsuccessful.

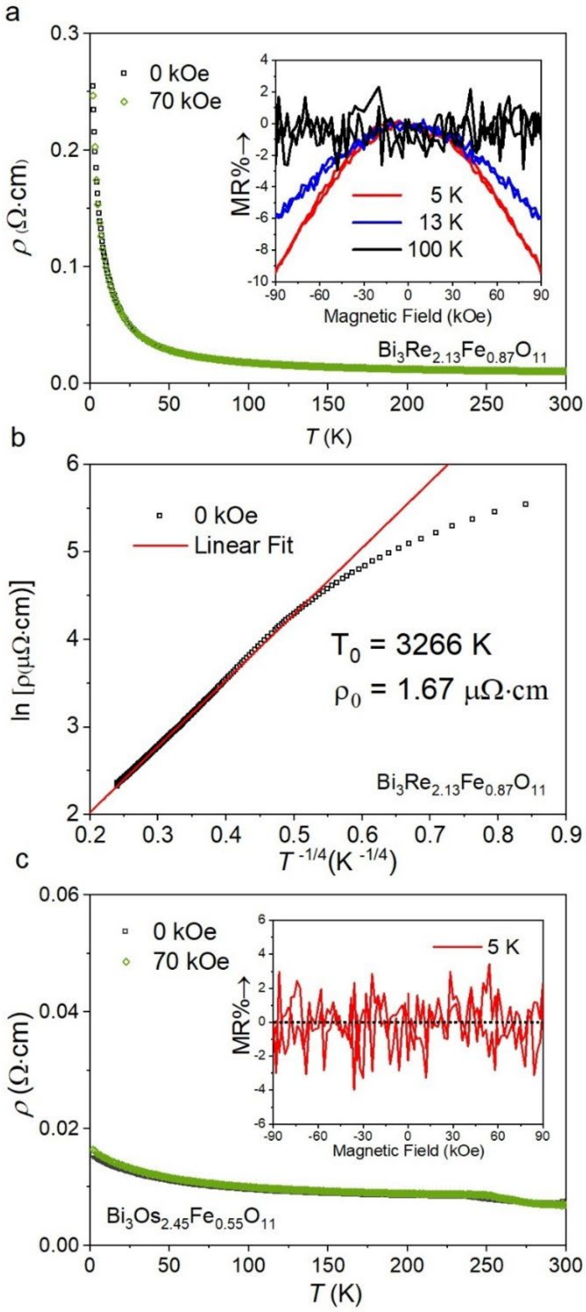

Figure 4.6. (a) Temperature dependence of the electrical resistivity of $Bi_3Re_{2.13}Fe_{0.87}O_{11}$ under different magnetic fields. The inset displays the magnetoresistance at 5, 13, and 100 K. (b) The corresponding ln(ρ) vs $T^{-1/4}$ curves of $Bi_3Re_{2.13}Fe_{0.87}O_{11}$. (c) Resistivity versus temperature plot of $Bi_3Os_{2.45}Fe_{0.55}O_{11}$ at different magnetic fields. The inset shows no magnetoresistance occurs at even 5 K.

4.3.4. Specific heat

Heat capacity measurements of the compounds were performed on Cp vs. T curves from 2 to 300 K during cooling. As shown in **Figure 4.7a.** and **Figure 4.7b.**, the C_p values changed monotonically with no characteristic anomalies in the temperature range. There was no peak near the magnetic transition point, which is consistent with the spin glassy behavior inferred above. The low-temperature part of the C_p/T vs. T^2 plot for each compound was analyzed using the approximate Debye model $C_p/T = \beta T^2+\gamma$, where γ is the electronic specific heat coefficient and β is a constant that contains the Debye temperature Θ_D ($\sim\beta^{1/3}$). For $Bi_3Os_{2.45}Fe_{0.55}O_{11}$, a plot fit yields $\gamma = 33.0(11)$ mJ mol^{-1} K^{-2} and $\beta = 4.19(3)\times10^{-3}$ J mol^{-1} K^{-4}, and for $Bi_3Re_{2.13}Fe_{0.87}O_{11}$ $\gamma = 33.2(9)$ mJ mol^{-1} K^{-2} and $\beta = 4.02(2)\times10^{-3}$ J mol^{-1} K^{-4}. The non-zero γ values indicate that the conduction electrons contribute significantly to C_p, consistent with the small electrical resistivities of the compounds. The estimated Θ_D values β for $Bi_3Re_{2.13}Fe_{0.87}O_{11}$ and $Bi_3Os_{2.45}Fe_{0.55}O_{11}$ are 199(1) K and 202(1) K, respectively, which are smaller than 250 K for the related compound, $Bi_{2.93}Os_3O_{11}$.[34]

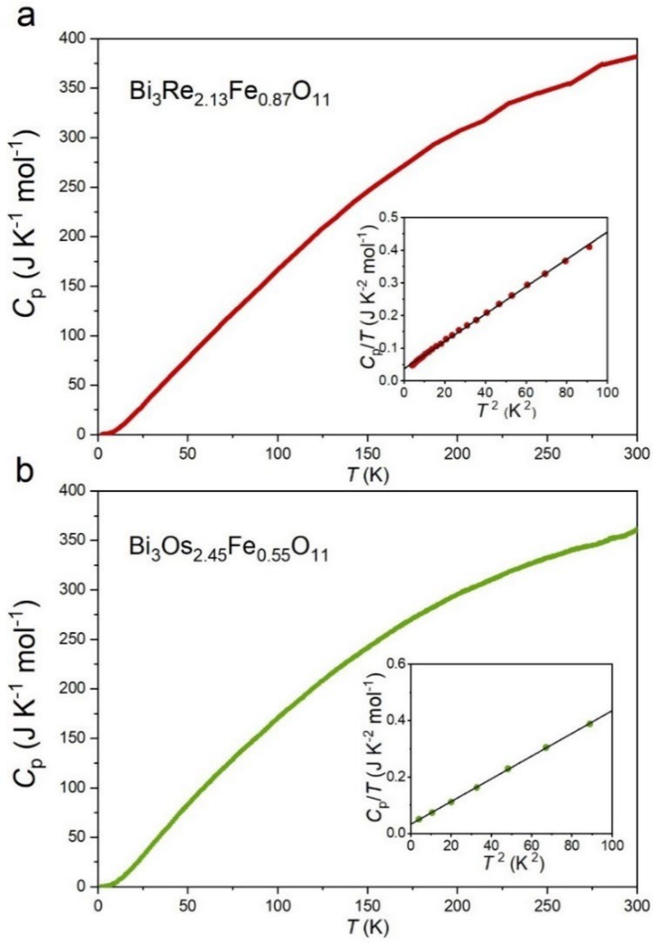

Figure 4.7. (a) Temperature dependence of C_p for $Bi_3Re_{2.13}Fe_{0.87}O_{11}$ and (b) $Bi_3Os_{2.45}Fe_{0.55}O_{11}$, respectively. The inset shows a linear fit of the low-temperature measurements of C_p/T vs. T^2.

4.4. Conclusion

$Bi_3Re_{2.13}Fe_{0.87}O_{11}$ and $Bi_3Os_{2.45}Fe_{0.55}O_{11}$, two Fe-doped 5d oxides, were synthesized at high temperatures and pressures. Synchrotron XRD analysis confirmed that these compounds belong to the $KSbO_3$-type family of the space group *Pn*-3, and their exact metal compositions were determined by EPMA. Unlike many other $KSbO_3$-type 5d oxides that exhibit only paramagnetism, spin glassy like behavior and magnetoresistance were observed in rhenium oxide, and ferrimagnetism was confirmed in osmium oxide, with the highest magnetic ordering temperature of 490 K in the $KSbO_3$-type.

This result suggests that $KSbO_3$-type 5d oxides are a group of compounds that are capable of developing spintronic material properties through doping of 3d elements. More importantly, sufficient $KSbO_3$-type materials are available to be used as host compounds, an abundance of 3d elements can be selected as doping candidates, and the doping ratio can be tuned and controlled by heat treatment. The Fe-doping levels of $Bi_3Re_3O_{11}$ and $Bi_3Os_3O_{11}$ may change when the heating conditions are changed. This possibility is currently being investigated. The results of this study indicate that doping with 3d elements may be employed to develop $KSbO_3$-type 5d oxides with both theoretical significance and practical value.

Reference in Chapter 4

(1) Daniel M. Giaquinta, Hans-Conrad Zur Loye. Structural Predictions in the ABO_3 Phase Diagram. *Chemistry of materials* **1994**, *6* (4), 365–372.

(2) G. R. Facer, M. M. Elcombe, B. J. Kennedy. Bismuth Ruthenium Oxides. Neutron Diffraction and Photoelectron Spectroscopic Study of $Bi_2Ru_2O_7$ and $Bi_3Ru_3O_{11}$. *Aust. J. Chem.* **1993**, *46* (12), 1897–1907.

(3) T. Fujita, K. Tsuchida, Y. Yasui, Y. Kobayashi, M. Sato. Transport, Thermal and Magnetic Properties of $Bi_3Os_3O_{11}$ and $Bi_3Ru_3O_{11}$. *Physica B: Condensed Matter* **2003**, *329–333*, 743–744.

(4) P. Khalifah, K. D. Nelson, R. Jin, Z. Q. Mao, Y. Liu, Q. Huang, X. P. A. Gao, A. P. Ramirez, R. J. Cava. Non-Fermi-Liquid Behaviour in La4Ru6O19. *Nature* **2001**, *411* (6838), 669–671.

(5) A. A. Belik, E. Takayama.M. Effects of Oxygen Content on $Bi_3Mn_3O_{11+\delta}$: From 45 K Antiferromagnetism to Room-Temperature True Ferromagnetism. *J. Am. Chem. Soc.* **2010**, *132* (35), 12426–12432.

(6) A. W. Sleight, R. J. Bouchard. New Cubic Potassium Antimony Oxide Derivative Structure with Interpenetrating Networks. Crystal Structure of Bismuth Gallium Antimony Oxide. *Inorg. Chem.* **1973**, *12* (10), 2314–2316.

(7) T. N. Nguyen, D.M. Giaquinta, W. M. Davis, H. C. zur Loye. Electrosynthesis of $KBiO_3$ (Potassium Bismuth Oxide): A Potassium Ion Conductor with the $KSbO_3$ (Potassium Antimony Oxide) Tunnel Structure. *Chem. Mater.* **1993**, *5* (9), 1273–1276.

(8) H. Suzuki, H. Ozawa, H. Sato. Anomalous Electric Conductions in $KSbO_3$-Type Metallic Rhenium Oxides. *Journal of the Physical Society of Japan* **2007**, *76* (4), 044805–044805.

(9) P. Khalifah, R. J. Cava. Metal-Metal Bonding in the $KSbO_3$-Type Oxides $La_4Ru_6O_{19}$ and $La_3Ru_3O_{11}$ A Mechanism for Band Gap Formation in t^{2g} States. *Phys. Rev. B* **2001**, *64* (8), 085111.

(10) J. Cheng, A. J. E. Rettie, M. R. Suchomel, H. Zhou, J. Yan, J. Song, L. G. Marshall, S. A. Larregola, J. Zhou, J. B. Goodenough. High-Pressure Synthesis, Structure, and Photoluminescence of a New $KSbO_3$-Type Bismuth Germanate $Bi_3Ge_3O_{10.5}$. *Inorg. Chem.* **2013**, *52* (4), 2138–2141.

(11) W. Yi, Y. Matsushita, A. Sato, K. Kosuda, M. Yoshitake, A. A. Belik. $Bi_3Cr_{2.91}O_{11}$: A Ferromagnetic Insulator from Cr^{4+}/Cr^{5+} Mixing. *Inorg. Chem.* **2014**, *53* (16), 8362–8366.

(12) A. A. Belik, Eiji Takayama-Muromachi. $BicMn_3O_{11}$: A New $KSbO_{11}$-Type Random Ferrimagnet with High T_c. *J. Am. Chem. Soc.* **2009**, *131* (27), 9504–9505.

(13) M. Li, M. Retuerto, Y. Bok Go, T. Emge, M. Croft, A. Ignatov, K. V. Ramanujachary, W. Dachraoui, J. Hadermann, M. Tang, J. Zhao, M. Greenblatt. Synthesis, Crystal Structure, and Properties of $KSbO_3$-Type $Bi_3Mn_{1.9}Te_{1.1}O_{11}$. *Journal of Solid State Chemistry* **2013**, *197*, 543–549.

(14) K. Ramesha, A. S. Prakash, M. Sathiya, G Madras, A. K. Shukla. Synthesis of New $(Bi, La)_3MSb_2O_{11}$ Phases (M = Cr, Mn, Fe) with $KSbO_3$-Type Structure and Their Magnetic and Photocatalytic Properties. *Bull Mater Sci* **2011**, *34* (2), 271–277.

(15) J.C Champarnaud.M, B. Frit, A. Aftatl, M. Elfarissi. $NaBi_2Sb_3O_{11}$: An Ordered Structure Related to the Cubic $KSbO_3$ Type. *Eur. j. solid state inorg. chem* **1995**, *32* (5), 493–504.

(16) T. Jardiel, D. G. Calatayud, M. Rodríguez, D. Fernández-Hevia, A. C. Caballero. Synthesis of Metastable $Bi_6Ti_5WO_{22}$ Phase by the Mechanochemical Method. *Materials Letters* **2013**, *94*, 58–60.

(17) A. V. Egorysheva, O. G. Ellert, Y. V. Zubavichus, O. M. Gajtko, N. N. Efimov, R. D. Svetogorov, V. Yu. Murzin. New Complex Bismuth Oxides in the Bi_2O_3–NiO–Sb_2O_5 System and Their Properties. *Journal of Solid State Chemistry* **2015**, *225*, 97–104.

(18) K.-I. Kobayashi, T. Kimura, H. Sawada, K. Terakura, Y. Tokura. Room-Temperature Magnetoresistance in an Oxide Material with an Ordered Double-Perovskite Structure. *Nature* **1998**, *395* (6703), 677–680.

(19) D. D. Sarma, E. V. Sampathkumaran, S. Ray, R. Nagarajan, S. Majumdar, A. Kumar, G. Nalini, T. N. Guru. Row Magnetoresistance in Ordered and Disordered Double Perovskite Oxide, Sr_2FeMoO_6. *Solid State Communications* **2000**, *114* (9), 465–468.

(20) K.-I. Kobayashi, T. Kimura, Y. Tomioka, H. Sawada, K. Terakura, Y. Tokura. Intergrain Tunneling Magnetoresistance in Polycrystals of the Ordered Double Perovskite Sr_2FeReO_6. *Phys. Rev. B* **1999**, *59* (17), 11159–11162.

(21) Y. Krockenberger, K. Mogare, M. Reehuis, M. Tovar, M. Jansen, G. Vaitheeswaran, V. Kanchana, F. Bultmark, A. Delin, F. Wilhelm, A. Rogalev, A. Winkler, L. Alff. Sr_2CrOsO_6: End Point of a Spin-Polarized Metal-Insulator Transition by 5d Band Filling. *Phys. Rev. B* **2007**, *75* (2), 020404.

(22) R. Morrow, J. R. Soliz, A. J. Hauser, J. C. Gallagher, M. A. Susner, M. D. Sumption, A. A. Aczel, J. Yan, F. Yang, P. M. Woodward. Effect of Chemical Pressure on High Temperature Ferrimagnetic Double Perovskites Sr_2CrOsO_6 and Ca_2CrOsO_6. *Journal of Solid State Chemistry* **2016**, *238*, 46–52.

(23) Hai L. Feng, M. Arai, Y. Matsushita, Y. Tsujimoto, Y. Guo, C. I. Sathish, X. Wang, Y. Yuan, M. Tanaka, K. Yamaura. High-Temperature Ferrimagnetism Driven by Lattice Distortion in Double Perovskite Ca_2FeOsO_6. *J. Am. Chem. Soc.* **2014**, *136* (9), 3326–3329.

(24) H. Wang, S. Zhu, X. Ou, H. Wu. Ferrimagnetism in the Double Perovskite Ca_2FeOsO_6: A Density Functional Study. *Phys. Rev. B* **2014**, *90* (5), 054406.

(25) A. M. Arévalo-López, G. M. McNally, J. P. Attfield. Large Magnetization and Frustration Switching of Magnetoresistance in the Double-Perovskite Ferrimagnet Mn_2FeReO_6. *Angewandte Chemie International Edition* **2015**, *54* (41), 12074–12077.

(26) M. Li, M. Retuerto, Z. Deng, P. W. Stephens, M. Croft, Q. Huang, H. Wu, X. Deng, G. Kotliar, J. Sánchez-Benítez, J. Hadermann, D. Walker, M. Greenblatt. Giant Magnetoresistance in the Half-Metallic Double-Perovskite Ferrimagnet Mn_2FeReO_6. *Angewandte Chemie International Edition* **2015**, *54* (41), 12069–12073.

(27) M. Li, J. P. Hodges, M. Retuerto, Z. Deng, P. W. Stephens, M. C. Croft, X. Deng, G. Kotliar, J. Sánchez-Benítez, D. Walker, M. Greenblatt. Mn_2MnReO_6: Synthesis and Magnetic Structure Determination of a New Transition-Metal-Only Double Perovskite Canted Antiferromagnet. *Chem. Mater.* **2016**, *28* (9), 3148–3158.

(28) Y. Shi, Y. Guo, X. Wang, A. J. Princep, D. Khalyavin, P. Manuel, Y. Michiue, A. Sato, K. Tsuda, S. Yu, M. Arai, Y. Shirako, M. Akaogi, N. Wang, K. Yamaura, A. T. Boothroyd. A Ferroelectric-like Structural Transition in a Metal. *Nature Materials* **2013**, *12* (11), 1024–1027.

(29) Y. G. Shi, Y. F. Guo, S. Yu, M. Arai, A. A. Belik, A. Sato, K. Yamaura, E. Takayama-Muromachi, H. F. Tian, H. X. Yang, J. Q. Li, T. Varga, J. F. Mitchell, S. Okamoto. Continuous Metal-Insulator Transition of the Antiferromagnetic Perovskite $NaOsO_3$. *Phys. Rev. B* **2009**, *80* (16), 161104.

(30) M. Tanaka, Y. Katsuya, A. Yamamoto. A New Large Radius Imaging Plate Camera for High-Resolution and High-Throughput Synchrotron X-Ray Powder Diffraction by Multiexposure Method. *Review of Scientific Instruments* **2008**, *79* (7), 075106.

(31) M. Tanaka, Y. Katsuya, Y. Matsushita, O. Sakata. Development of a Synchrotron Powder Diffractometer with a One-Dimensional X-Ray Detector for Analysis of Advanced Materials. *Journal of the Ceramic Society of Japan* **2013**, *121* (1411), 287–290.

(32) F. Izumi, K. Momma. Three-Dimensional Visualization in Powder Diffraction. *Solid State Phenomena* **2007**, *130*, 15–20.

(33) K. Momma, F. Izumi. VESTA: A Three-Dimensional Visualization System for Electronic and Structural Analysis. *J Appl Cryst* **2008**, *41* (3), 653–658.

(34) Y. Yuan, H. Feng, Y. Shi, Y. Tsujimoto, A. A. Belik, Y. Matsushita, M. Arai, J. He, M. Tanaka, K. Yamaura. High-Pressure Synthesis, Crystal Structure, and Magnetic Properties of $KSbO_3$-Type 5d Oxides $K_{0.84}OsO_3$ and $Bi_{2.93}Os_3O_{11}$. *Sci. Technol. Adv. Mater.* **2014**, *15* (6), 064901.

(35) N. E. Brese, M. O’Keeffe. Bond-Valence Parameters for Solids. *Acta Cryst B* **1991**, *47* (2), 192–197.

(36) J. Greedan, C. Thompson, L. Chi, A. Hallas, M. Wilson, Timothy Munsie, Ian Swainson, Andrew Grosvenor, John Hayes, Graeme Luke. Synthesis, Structure, and Magnetic Properties of Novel B-Site Ordered Double Perovskites, $SrLaMReO_6$ (M = Mg, Mn, Co and Ni). *Dalton Trans.* **2015**, *44*.

(37) M. Retuerto, M. Li, P. W. Stephens, J. Sánchez-Benítez, X. Deng, Gabriel Kotliar, Mark C. Croft, Alexander Ignatov, David Walker, Martha Greenblatt. Half-Metallicity in Pb_2CoReO_6 Double Perovskite and High Magnetic Ordering Temperature in Pb_2CrReO_6 Perovskite. *Chem. Mater.* **2015**, *27* (12), 4450–4458.

(38) *Spin Glasses : An Experimental Introduction*; CRC Press, 1993.

(39) H. Feng, P. Adler, M. Reehuis, W. Schnelle, P. Pattison, Andreas Hoser, Claudia Felser, Martin Jansen. High-Temperature Ferrimagnetism with Large Coercivity and Exchange Bias in the Partially Ordered 3d/5d Hexagonal Perovskite $Ba_2Fe_{1.12}Os_{0.88}O_6$. *Chem. Mater.* **2017**, *29* (2), 886–895.

(40) E. Solana-Madruga, C. Ritter, O. Mentré, J. P. Attfield, Á. M. Arévalo-López. Giant Coercivity and Spin Clusters in High Pressure Polymorphs of Mn_2LiReO_6. *J. Mater. Chem. C* **2022**, *10* (11), 4336–4341.

(41) Elena Solana-Madruga, Khalid N. Alharbi, Maria Herz, Pascal Manuel, J. Paul Attfield. Unconventional Magnetism in the High Pressure ‘All Transition Metal’ Double Perovskite Mn_2NiReO_6. *Chemical Communications* **2020**, *56* (83), 12574–12577.

Chapter 5 High-pressure synthesis of half-doped perovskites $MnV_{0.5}Nb_{0.5}O_3$ and $MnV_{0.5}Ta_{0.5}O_3$ with unusual A-site small Mn atoms

5.1. Introduction

Perovskites have been a prominent research area for several decades and have garnered significant attention due to the intriguing phenomena exhibited by ABO_3-type perovskite oxides. These phenomena include ferroelectricity in materials like $BaTiO_3$ [1,2,3], $SrTiO_3$ [4,5], $PbTiO_3$ [6,7], $KNbO_3$ [8,9], high-T_c superconductivity in $BaPb_{1-x}Bi_xO_3$ [10], colossal magnetoresistance in $NdBaMn_2O_6$ [11], $LaMnO_3$ [12], Sr_2CrWO_6 [13], charge/orbital ordering in $Ln_{1-x}A_xMnO_3$ (Ln = Rare Earth, A = Ca or Sr) [14], $Sm_{0.5}Ba_{0.5}MnO_3$ [15], $PbFeO_3$ [16], multiferroicity in BiCrO3 [17], $BiMnO_3$ [18,19] and $BiFeO_3$ [20,21], superconductivity in (Ba, K)SbO_3 [22] , $MgCNi_3$ [23], photoelectricity in $CsPbX_3$ (X = Br or I) [24], exotic magnetism in Ca_2MnReO_6 [25] and significant thermoelectricity in $CsSnI_3$ [26] and so on, which make them promising materials for both scientific investigations and industrial applications.

Usually, transition-metal cations occupy *B*-sites while larger alkaline-earth or rare-earth ions locate in *A*-sites. In 1971, Shono *et al.* [27] demonstrated that under high-pressure conditions, it is possible to fill the A-sites with relatively small transition metal cations, leading to the synthesis of perovskite-type $MnVO_3$. Introducing magnetic elements at A-sites can induce exotic properties, such as ferroelectricity or magnetic ferroelectricity, through strong interactions with elements at B-sites. Consequently, extensive research into unusual A-site manganese was undertaken to explore their unique magnetic and electronic properties, leading to the discovery of many excellent properties, such as multiferroism in $CaMnTi_2O_6$ [28] and the unusual site-selective doping effect in $AMn_3V_4O_{12}$ (A = Na^+, Ca^{2+}, La^{3+}) [29]. Notably, in 2015, Arévalo *et al.* reported a double perovskite Mn_2FeReO_6 [30], which exhibits a high Curie temperature of 520 K and displays large magnetoresistance, making it a significant candidate for potential applications in spintronics. Subsequently, canted antiferromagnetic properties were identified in Mn_2MnReO_6 [31], unconventional magnetism in Mn_2NiReO_6 [32], and multiple transition metal sublattice magnetic effects in $Mn_2(Fe_{0.8}Mo_{0.2})MoO_6$ [33], providing further insights into the rich magnetic behavior of these materials.

Therefore, the search for unusual A-site manganese oxides with unique magnetic and electronic properties holds great potential for the scientific design, theoretical exploration, and practical application of new materials. In this study, I explored the properties of $MnVO_3$, first synthesized in 1971 [27], and introduced d^0 ions, Nb^{5+} and Ta^{5+}, into the structure to explore possible magnetic ferroelectricity. Consequently, $MnV_{0.5}Nb_{0.5}O_3$ was synthesized under high-pressure and high-temperature conditions of 6 GPa and 1300°C, respectively, while $MnV_{0.5}Ta_{0.5}O_3$ was synthesized at 6 GPa and 900°C. Structural analysis by synchrotron radiation X-ray diffraction confirmed that both $MnV_{0.5}Nb_{0.5}O_3$ and $MnV_{0.5}Ta_{0.5}O_3$ are half-doped perovskite oxides and not double perovskite oxides. Furthermore, the absence of a polar structure indicated that the materials do not exhibit ferroelectricity at room temperature. However, magnetization measurements confirmed antiferromagnetic ordering at 17 K and 18 K for $MnV_{0.5}Nb_{0.5}O_3$ and $MnV_{0.5}Ta_{0.5}O_3$, respectively, with a slight contribution of thermal and magnetic field hysteresis. Additionally, both compounds also exhibit semiconducting behavior at estimated activation energies of about 0.13 eV and 0.31 eV, respectively. Unfortunately, the observed electrical conductivity in these materials posed challenges in performing accurate dielectric measurements, as it could introduce significant noise in the data, hindering the assessment of their response to electric fields and their potential as ferroelectrics. The observed antiferromagnetic nature and semiconducting behavior in these A-site manganese oxides underscore the potential of these materials for future research in the exploration of their unique magnetic and electronic properties.

5.2. Experimental

Polycrystalline $MnV_{0.5}Nb_{0.5}O_3$ and $MnV_{0.5}Ta_{0.5}O_3$ were synthesized using high-purity materials: MnO (99.99%, High Purity Chemical Co. Ltd.), V_2O_3 (99.99%, High Purity Chemical Co. Ltd.), Nb_2O_5 (99.9%, Rare Metallic Co. Ltd.), and Ta_2O_5 (99.9%, Rare Metallic Co. Ltd.). The powders of MnO, V_2O_3, and Nb_2O_5 (or Ta_2O_5) were mixed in stoichiometric ratios and then pressed into pellets after thorough grinding. Subsequently, the $MnV_{0.5}Nb_{0.5}O_3$ sample was enclosed in a Pt capsule and heated at 1300 °C for 1 hour under a pressure of 6 GPa using a multi-anvil-type high-pressure apparatus (CTF-MA1500P, C&T Factory Co., Ltd, Japan). Following the heating process, the pressure was gradually released over several hours. The synthesis procedure for $MnV_{0.5}Ta_{0.5}O_3$ was similar to $MnV_{0.5}Nb_{0.5}O_3$, but the temperature used was 900 °C.

Synchrotron XRD data were investigated at room temperature using a large Debye-Scherrer camera at beamline BL02B2 at SPring-8 [34,35], Japan. The incident beam was monochromatized at $\lambda = 0.420259$ Å. A benchmark test was performed using a standard (CeO_2) to confirm the wavelength before the measurements. The samples were put into Lindenmann glass capillaries (inner diameter: 0.1 mm) and rotated during the measurements. The RIETAN-VENUS software package was used to analyze the synchrotron XRD patterns [36,37].

Magnetic properties were investigated using a magnetic property measurement system (MPMS-XL-7T, Quantum Design). Magnetic susceptibilities (χ) were measured over the temperature range of 2 to 300 K, under both zero-field-cooling (ZFC) and field-cooling (FC) conditions, in a fixed applied magnetic field of 10 kOe. Isothermal magnetization measurements were conducted at temperatures of 5 K and 50 K, spanning magnetic fields between 70 kOe and -70 kOe.

The electrical properties and specific heat of both $MnV_{0.5}Nb_{0.5}O_3$ and $MnV_{0.5}Ta_{0.5}O_3$ were measured using a Physical Property Measurement System (PPMS, Quantum Design). The temperature dependence of electric resistivity (ρ) was recorded using a four-probe method, with the temperature range for $MnV_{0.5}Nb_{0.5}O_3$ being approximately 140-300 K. To establish connections between the sample and the device terminals, silver paste and platinum wires (50 μm in diameter) were utilized. The measured current during the experiments was maintained at 1 mA. Furthermore, the temperature dependence of specific heat capacities (C_p) was measured using the same machine, employing a thermal relaxation method. These measurements were conducted over the temperature range from 2 to 300 K.

5.3. Results and discussion

5.3.1. Crystal Structure.

The analyzed SXRD pattern and the refined crystallographic parameters of both $MnV_{0.5}Nb_{0.5}O_3$ and $MnV_{0.5}Ta_{0.5}O_3$ obtained at room temperature are presented in **Figure.5.1** and **Table.5.1**. Here the crystal structure model proposed for $MnVO_3$ was employed as the mode of the Rietveld refinement. Both of them were successfully identified using the space group of *Pnma*. Trace impurities were discovered in both samples, in $MnV_{0.5}Nb_{0.5}O_3$, around 5.3 wt% $MnNb_2O_6$ was detected and in $MnV_{0.5}Ta_{0.5}O_3$, around 2.5 wt% VTaO4 was traced. The lattice constants of $MnV_{0.5}Nb_{0.5}O_3$ were calculated as follows: a = 5.40739(7) Å, b =

7.59492(9) Å, c = 5.22262(6) Å. Similarly, for $\mathrm{MnV_{0.5}Ta_{0.5}O_3}$, the lattice constants were determined as: a = 5.41934(3) Å, b = 7.61121(4) Å, c = 5.23227(2) Å. While exploring possible double perovskite structure models reported for other Mn-containing compounds at the A-site of double perovskite oxides [30-32], I found them to be unlikely to fit the observed patterns.

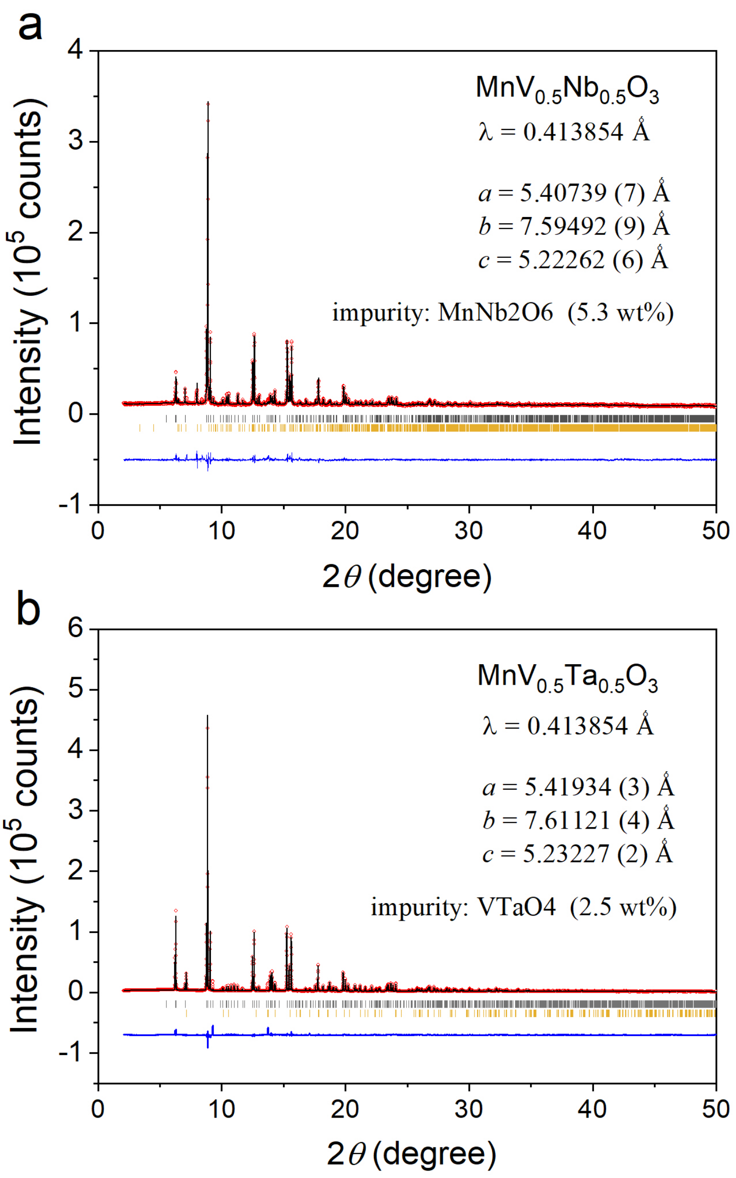

Figure 5.1. Synchrotron XRD data for $\mathrm{MnV_{0.5}Nb_{0.5}O_3}$ and $\mathrm{MnV_{0.5}Ta_{0.5}O_3}$ in the orthorhombic *Pnma* structure at room temperature (296-300 K). Each panel displays the observed pattern (red circles), calculated pattern (black solid lines), and the difference profile (blue curves). Vertical bars indicate possible Bragg reflection positions for the main phase (the first row) and the impurity (the second row).

Analysis of the refinement results reveals that Mn atoms occupy the 4*c* (*x*, 0.25, *z*) Wyckoff positions fully, while V and Nb/Ta atoms are randomly distributed in the 4*a* (0, 0, 0) sites. The ratio of V and Nb/Ta was fixed at 1:1 in the refinements, based on the stoichiometry of the starting raw materials. Oxygen atoms O1 and O2 are located at independent positions, 4*c* (*x*, 0.25, *z*) and 8*d* (*x*, *y*, *z*), respectively. The final detailed lattice parameters, atomic coordinates, and temperature factors are summarized and presented in **Table 5.1.**

Table 5.1. Structure Parameters of $MnV_{0.5}Nb_{0.5}O_3$ and $MnV_{0.5}Ta_{0.5}O_3$

Atom	Wyckoff	*g*	*x*	*y*	*z*	*B* (Å^2)
			$MnV_{0.5}Nb_{0.5}O_3$			
Mn	4*c*	1	0.0515(3)	0.25	0.4875(5)	1.23(5)
V/Nb	4*a*	0.5/0.5	0	0	0	0.61(2)
O1	4*c*	1	0.4558(13)	0.25	0.6092(11)	0.12(16)
O2	8*d*	1	0.2994(10)	0.0591(6)	0.1892(9)	0.65(1)
			$MnV_{0.5}Ta_{0.5}O_3$			
Mn	4*c*	1	0.0510(2)	0.25	0.4878(5)	1.48(3)
V/Ta	4*a*	0.5/0.5	0	0	0	0.58(1)
O1	4*c*	1	0.4561(11)	0.25	0.6164(10)	0.40(12)
O2	8*d*	1	0.3032(8)	0.0588(5)	0.1899(8)	0.65(9)

Note. The space group was *Pnma* (no. 62) at origin choice 2, $Z = 4$, and *g* was the occupation factor. $MnV_{0.5}Nb_{0.5}O_3$: a = 5.40739(7) Å, b = 7.59492(9) Å, c = 5.22262(6) Å and V = 412.669(10) Å^3. *R* Indices are R_{wp} = 5.343%, R_p = 3.859%, R_B = 6.608%, and R_F = 7.208%. $MnV_{0.5}Ta_{0.5}O_3$: a = 5.41934(3) Å, b = 7.61121(4) Å, c = 5.23227(2) Å and V = 412.669(10) Å^3. *R* Indices are R_{wp} = 8.232%, R_p = 4.724%, R_B = 5.532%, and R_F = 4.151%.

To illustrate the crystal structure, one compound was chosen, and it is displayed in **Figure.5.2a**. as both compounds crystallize in the same space group of *Pnma*. The left side of the figure shows the crystal structure observed along the c-axis, with a slight shift in the direction of observation for better visibility. On the right side is the view perpendicular to the c-axis. Notably, both compounds exhibit octahedral distortions and connected twisting compared to the ideal cubic perovskites. In **Figure.5.2b**, a comparison of the lattice parameters and unit cell volumes of $MnV_{0.5}Nb_{0.5}O_3$ and $MnV_{0.5}Ta_{0.5}O_3$ with the related compound $MnVO_3$ was present. Here the horizontal coordinates are labelled with elements rather than ionic radii because Nb^{5+} and Ta^{5+} have the same ionic radii, so I take a listing of 3d, 4d and 5d elements. The comparison clearly indicates that the lattice parameters and unit cell volumes increase monotonically with the increase of the atomic numbers.

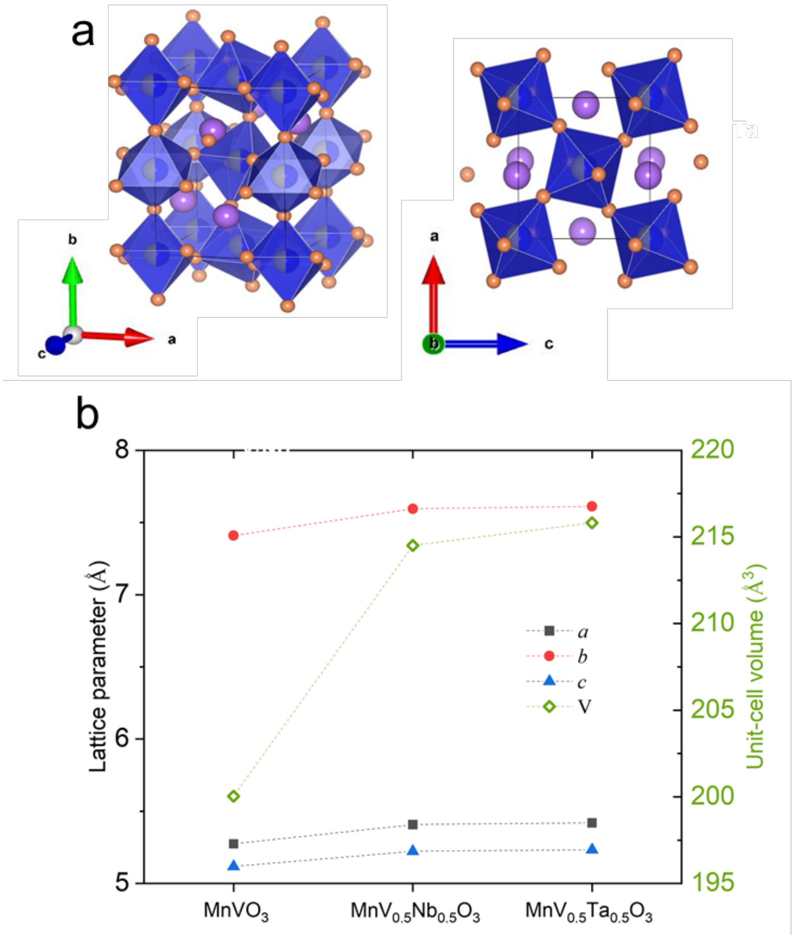

Figure 5.2. (a) Structure for MnV$_{0.5}$Nb$_{0.5}$O$_3$ and (b) a comparison of lattice parameters among MnV$_{0.5}$Nb$_{0.5}$O$_3$, MnV$_{0.5}$Ta$_{0.5}$O$_3$ and MnVO$_3$.

The valence states of Mn, V, and Nb (or Ta) atoms were determined based on the bond distances in different compounds, and the bond valence sums (BVS) [38] results are presented in **Table.5.2**. The BVS calculations for Mn in both MnV$_{0.5}$Nb$_{0.5}$O$_3$ and MnV$_{0.5}$Ta$_{0.5}$O$_3$ yielded a value of 1.82, indicating a 2+ valence state for Mn in both compounds. The BVS values for the V atoms corresponded to 3+, and for Nb (or Ta) atoms, they were very close to 5+, suggesting the effectiveness of the BVS method for determining the valence states of these elements in the compounds.

Table 5.2. Selected bond lengths, angles, and bond balance sums (BVS) of MnV$_{0.5}$Nb$_{0.5}$O$_3$ and MnV$_{0.5}$Ta$_{0.5}$O$_3$ at room temperature.

MnV$_{0.5}$Nb$_{0.5}$O$_3$	Bond lengths (Å); BVS; bond angles (°)	MnV$_{0.5}$Ta$_{0.5}$O$_3$	Bond lengths (Å); BVS; bond angles (°)

Mn – O1	3.159(7)	Mn – O1	3.203(6)
Mn – O1	3.283(8)	Mn – O1	4.273(3)
Mn – O1	2.277(8)	Mn – O1	2.296(6)
Mn – O1	2.169(7)	Mn – O1	2.134(6)
Mn – O2 (×2)	2.515(6)	Mn – O2 (×2)	2.695(5)
Mn – O2 (×2)	2.194(6)	Mn – O2 (×2)	2.188(5)
Mn – O2 (×2)	2.697(6)	Mn – O2 (×2)	2.533(5)
Mn – O2 (×2)	3.459(6)	Mn – O2 (×2)	3.471(5)
BVS (Mn)	1.82	BVS (Mn)	1.82
V/Nb – O1 (×2)	1.997(2)	V/Ta - O1 (×2)	2.012(2)
V/Nb – O2 (×2)	1.949(6)	V/Ta – O2 (×2)	1.971(5)
V/Nb – O2 (×2)	2.003(6)	V/Ta – O2 (×2)	1.993(5)
BVS (V)	3.14	BVS (V)	3.06
BVS (Nb)	4.95	BVS (Ta)	4.94
V(Nb) – O1 – V(Nb)	143.9(4)	V(Ta) – O1 – V(Ta)	142.1(3)
V(Nb) – O2 – V(Nb)	144.0(3)	V(Ta) – O2 – V(Ta)	143.7(3)

Note. BVS = $\sum_{i=1}^{N} v_i$, v_i = exp[(R_0–l_i)/B], N is the coordination number, B = 0.37, R_0(Mn^{2+}) = 1.79, R_0(V^{3+}) = 1.743, R_0(Nb^{5+}) = 1.911, R_0(Ta^{5+}) = 1.920,[38]

5.3.2. Magnetic property

The temperature dependence of χ under an applied magnetic field of 10 kOe for both compounds is shown in **Figure 5.3**. Peaks were observed at around 17 K and 18 K for MnV$_{0.5}$Nb$_{0.5}$O$_3$ and MnV$_{0.5}$Ta$_{0.5}$O$_3$, respectively. The χ^{-1} vs. T data (200 - 300 K) were fitted using the Curie-Weiss law (see the inset of **Figure 5.3**), resulting in Curie constants of 3.94 and 4.92 emu mol^{-1} K^{-1} (equivalent to effective magnetic moments of 5.61 and 6.27 μ_B), and Weiss temperatures of -95.9 K and -92.56 K for MnV$_{0.5}$Nb$_{0.5}$O$_3$ and MnV$_{0.5}$Ta$_{0.5}$O$_3$, respectively. Theoretical calculations within the simple spin-only model predicted a magnetic moment of 6.25 μ_B for all compounds. Remarkably, the observed effective magnetic moments were comparable to the theoretical results. The large negative Weiss temperatures indicate the presence of antiferromagnetic interactions in these compounds.

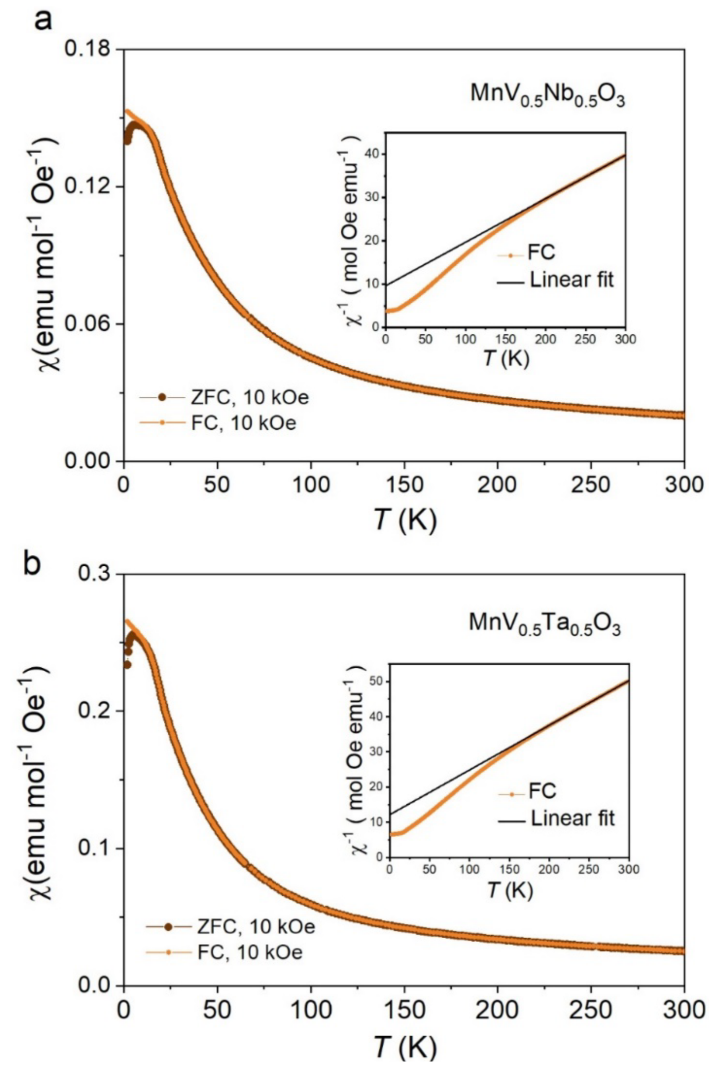

Figure 5.3. (a) Temperature dependence of magnetic susceptibility (χ) for $MnV_{0.5}Nb_{0.5}O_3$ and (b) $MnV_{0.5}Ta_{0.5}O_3$. Insets show the χ^{-1} vs. T curves used for the Curie-Weiss law fittings.

From the ZFC and FC curves, I observe divergence at low temperatures, suggesting that the compounds may exhibit antiferromagnetic or spin-glass behavior at low temperatures. To investigate the intrinsic nature of the magnetic ground state, the isothermal magnetization curves at 5 K and 50 K were plotted in **Figure 5.4**. Even at 5 K and below 7 T, the magnetizations do not saturate, and the values are approximately 0.8 μ_B per formula unit (f.u.) for $MnV_{0.5}Nb_{0.5}O_3$ and 1.0 μ_B per f.u. for $MnV_{0.5}Ta_{0.5}O_3$, far below the expected spin-only value of 6 μ_B per f.u. The linear $M(H)$ curves at 50 K suggest the paramagnetic states, while the typical 'S'-shaped hysteresis loops at 5 K indicate the presence of either antiferromagnetic ordering or spin-glass behavior in the samples. To precisely determine the spin alignments, I conducted heat capacity measurements to confirm the accurate magnetic behavior of the samples.

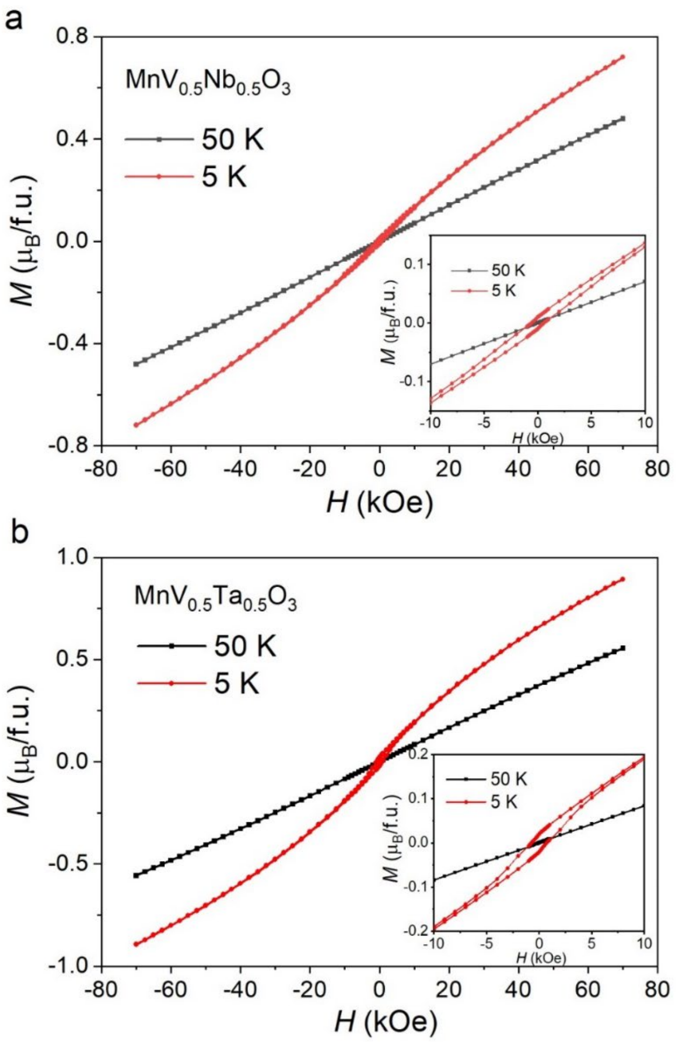

Figure 5.4. (a) Magnetic field-dependent magnetization for $MnV_{0.5}Nb_{0.5}O_3$ and (b) $MnV_{0.5}Ta_{0.5}O_3$ at temperatures of 5 and 50 K.

5.3.3. Heat capacity

To investigate the magnetic transitions, I conducted temperature-dependent C_p measurements for both compounds. The C_p/T vs. T data were recorded during cooling from 300 to 2 K, and the results are presented in **Figure. 5.5**. Clear peaks were observed at the magnetic transition temperature points, indicating the presence of long-range order transitions in the compounds. These prominent peaks are likely connected to the splitting observed in the ZFC and FC curves, primarily arising from the long-range antiferromagnetic transition. However, it is worth noting that a magnetic glassy transition cannot be completely ruled out, as evidenced by a peak-like feature in some cases, although a broad hump is typically observed

[39]. Further detailed studies will be required to fully elucidate the nature of the magnetic transitions in these compounds.

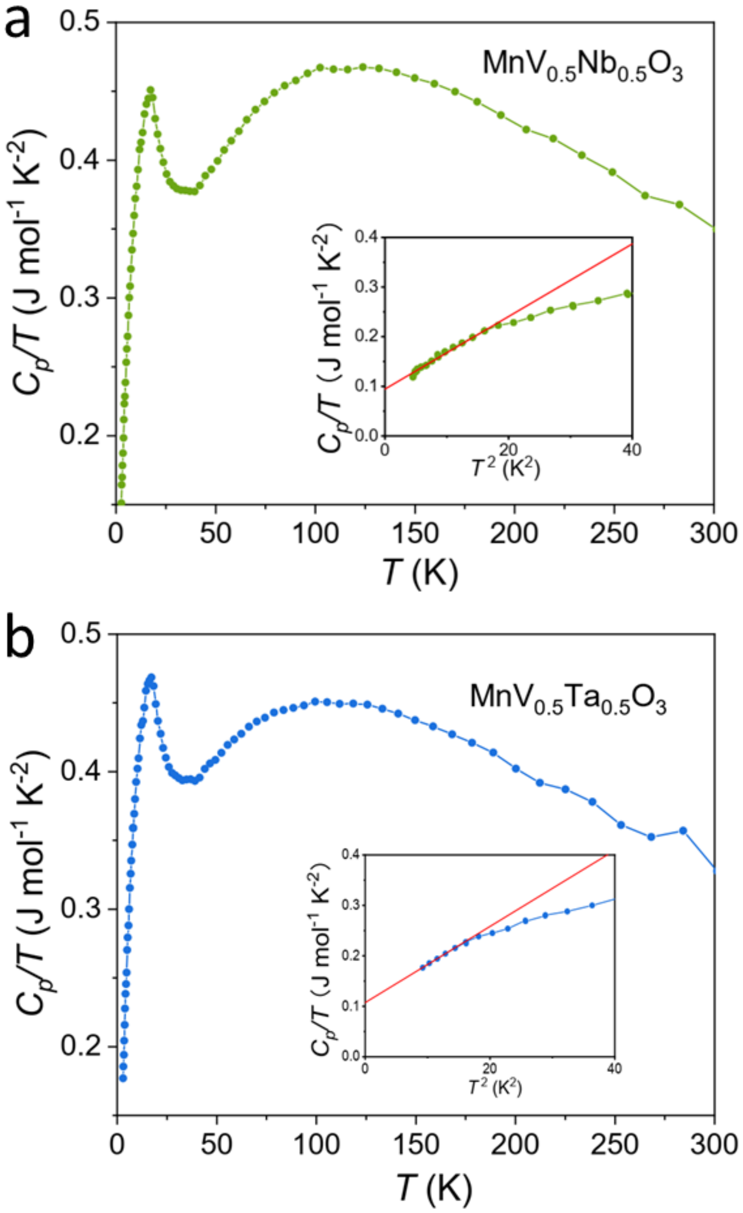

Figure 5.5. (a) Temperature dependence of specific heat capacity (C_p) for $MnV_{0.5}Nb_{0.5}O_3$ and (b) $MnV_{0.5}Ta_{0.5}O_3$. (Inset) The C_p/T vs. T^2 data in the low-temperature region were fitted using a linear model.

In the low-temperature region, the C_p/T vs. T^2 plot for each compound was analyzed using the approximate Debye model $C_p/T = \beta T^2+\gamma$, where γ is the electronic specific heat coefficient and β is a constant that contains the Debye temperature Θ_D ($\sim\beta^{1/3}$). For $MnV_{0.5}Nb_{0.5}O_3$, the linear fitting yields $\gamma = 94.0(2)$ mJ mol^{-1} K^{-2} and $\beta = 7.31(2) \times 10^{-3}$ J mol^{-1}

K^{-4}, and for $MnV_{0.5}Ta_{0.5}O_3$, $\gamma = 111(1)$ mJ mol^{-1} K^{-2} and $\beta = 7.2(1) \times 10^{-3}$ J mol^{-1} K^{-4}. Indeed, the non-zero γ values typically indicate significant contributions from conduction electrons to the C_p. However, the absence of electrical conductivity in the compound at low temperatures suggests that this γ is likely attributed to other sources beyond conduction electrons. It is possible that a component related to magnetic ordering or other magnetic effects is contributing to the specific heat. To fully understand and explain this phenomenon, further comprehensive investigations are required. These may include studying the magnetic field dependence of C_p, conducting additional density functional theory (DFT) calculations, and performing in-depth analyses of the compound's magnetic properties. These combined efforts will provide valuable insights into the nature of the specific heat behavior and its underlying mechanisms in $MnV_{0.5}Nb_{0.5}O_3$ and $MnV_{0.5}Ta_{0.5}O_3$ at low temperatures.

5.3.4. Electronic property

The temperature dependence of the ρ for polycrystalline $MnV_{0.5}Nb_{0.5}O_3$ and $MnV_{0.5}Ta_{0.5}O_3$ displayed insulating behaviors, as shown in **Figure 5.6**. The ρ at room temperature were approximately 100 Ω cm and 1000 Ω cm for $MnV_{0.5}Nb_{0.5}O_3$ and $MnV_{0.5}Ta_{0.5}O_3$, respectively, consistent with their semiconductor nature. As the measurement temperature decreased below 130 K for $MnV_{0.5}Nb_{0.5}O_3$ and 200 K for $MnV_{0.5}Ta_{0.5}O_3$, the ρ exceeded the test range of the instrument, making it challenging to obtain measurements at even lower temperatures. Notably, the prototype compound from which they are derived, $MnVO_3$, exhibits metallic properties. The large difference in electrical conductivity observed in $MnV_{0.5}Nb_{0.5}O_3$ and $MnV_{0.5}Ta_{0.5}O_3$ may be attributed to the addition of Nb^{5+} and Ta^{5+} ions, which reduces the valence of V from a 4+ state to a 3+ state. This change causes the absence of itinerant electrons present in the original system and their replacement with pairs of electrons, resulting in a dramatic increase in ρ.

The data were fitted using the Arrhenius equation, and the relative activation energy of $MnV_{0.5}Nb_{0.5}O_3$ and $MnV_{0.5}Ta_{0.5}O_3$ were estimated to be 0.13 eV and 0.31 eV, respectively. These experimentally evaluated values confirm that both compounds exhibit semiconducting behavior. Additionally, the Efros-Shklovskii variable-range hopping conduction model was employed, $\rho = \rho_0 \exp[(T_0/T)^{1/2}]$ [40], to analyze the data, and it was found that the data seem to fit the model well. Further in-depth discussions about the transport properties will be expected after single crystal growth is achieved, and transport measurements are conducted.

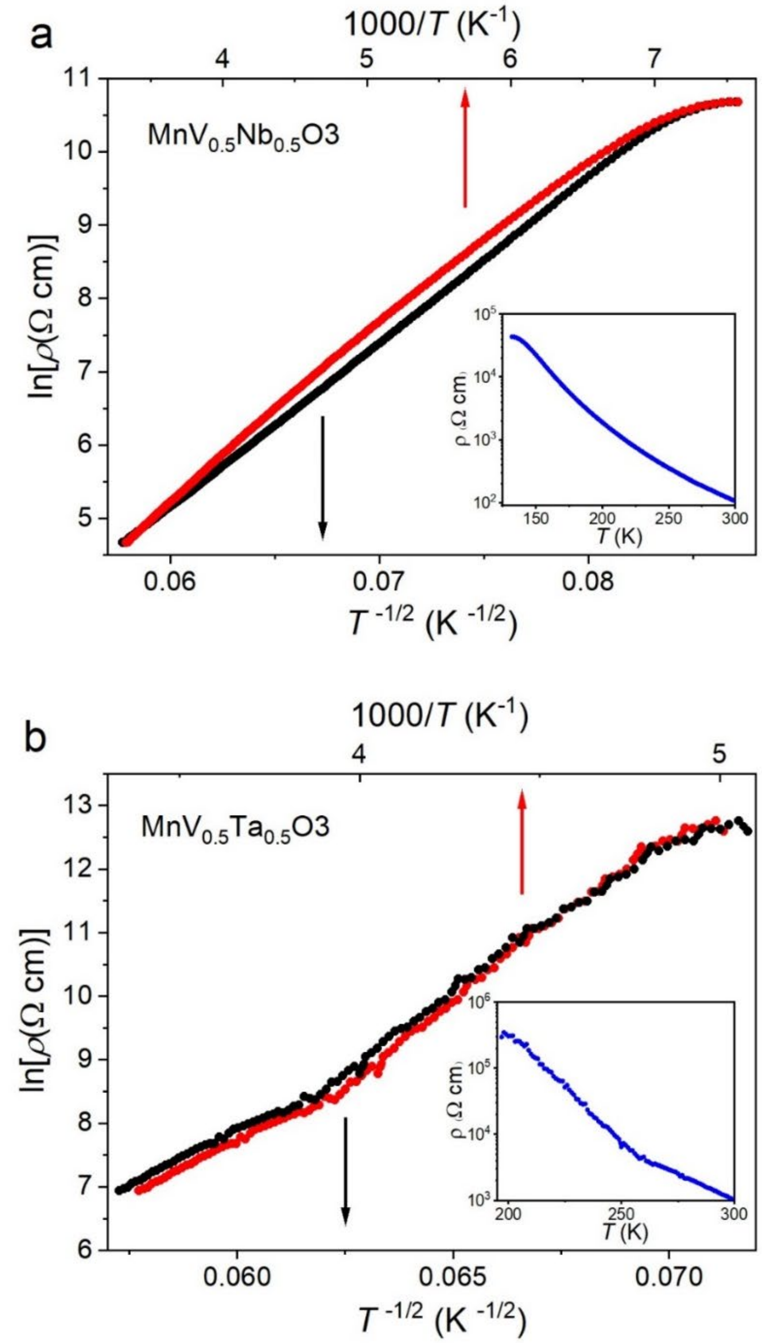

Figure 5.6. (a) Electrical resistivity (ρ) for $MnV_{0.5}Nb_{0.5}O_3$ and (b) $MnV_{0.5}Ta_{0.5}O_3$

5.4. Conclusion

In summary, my study successfully synthesized two novel half-doped perovskites, $MnV_{0.5}Nb_{0.5}O_3$ and $MnV_{0.5}Ta_{0.5}O_3$, with unique magnetic and electronic properties due to the incorporation of small Mn atoms at the A site. The crystallographic analysis confirmed their *Pnma* structure, distinct from an ordered perovskite. Magnetic measurements revealed antiferromagnetic behavior below 17 K and 18 K for the respective compounds, with a slight contribution of hysteresis. Furthermore, the observed semiconductor-like behavior in electrical conductivity highlights their potential for electronic applications. These results underscore the significance of these materials with unusual A-site small Mn atoms and open new avenues for further research into their unique magnetic and electronic properties. Future studies should explore single crystal growth and in-depth transport measurements to advance the understanding and unlock their practical applications in electronic and magnetic devices.

Reference in Chapter 5

(1) Veronica F. Michel, Tobias Esswein, Nicola A. Spaldin. Interplay between Ferroelectricity and Metallicity in $BaTiO_3$. *J. Mater. Chem. C* **2021**, *9* (27), 8640–8649.

(2) Millicent B. Smith, Katharine Page, Theo Siegrist, Peter L. Redmond, Erich C. Walter, Ram Seshadri, Louis E. Brus, Michael L. Steigerwald. Crystal Structure and the Paraelectric-to-Ferroelectric Phase Transition of Nanoscale $BaTiO_3$. *J. Am. Chem. Soc.* **2008**, *130* (22), 6955–6963.

(3) Ronald E. Cohen. Origin of Ferroelectricity in Perovskite Oxides. *Nature* **1992**, *358* (6382), 136–138.

(4) J. H. Haeni, P. Irvin, W. Chang, R. Uecker, P. Reiche, Y. L. Li, S. Choudhury, W. Tian, M. E. Hawley, B. Craigo, A. K. Tagantsev, X. Q. Pan, S. K. Streiffer, L. Q. Chen, S. W. Kirchoefer, J. Levy, D. G. Schlom. Room-Temperature Ferroelectricity in Strained $SrTiO_3$. *Nature* **2004**, *430* (7001), 758–761.

(5) Ruijuan Xu, Jiawei Huang, Edward S. Barnard, Seung Sae Hong, Prastuti Singh, Ed K. Wong, Thies Jansen, Varun Harbola, Jun Xiao, Bai Yang Wang, Sam Crossley, Di Lu, Shi Liu, Harold Y. Hwang. Strain-Induced Room-Temperature Ferroelectricity in $SrTiO_3$ Membranes. *Nature Communications* **2020**, *11* (1), 3141.

(6) V. G. Bhide, K. G. Deshmukh, M. S. Hegde. Ferroelectric Properties of $PbTiO_3$. *Physica* **1962**, *28* (9), 871–876.

(7) Shujun Zhang, Fei Li. High Performance Ferroelectric Relaxor-$PbTiO_3$ Single Crystals: Status and Perspective. *Journal of Applied Physics* **2012**, *111* (3), 031301.

(8) Linyun Liang, Y. L. Li, Long-Qing Chen, S. Y. Hu, Guang-Hong Lu. Thermodynamics and Ferroelectric Properties of $KNbO_3$. *Journal of Applied Physics* **2009**, *106* (10), 104118.

(9) Izumi Masuda, Ken-Ichi Kakimoto, Hitoshi Ohsato. Ferroelectric Property and Crystal Structure of KNbO3 Based Ceramics. *J Electroceram* **2004**, *13* (1), 555–559.

(10) A. W. Sleight, J. L. Gillson, P. E. Bierstedt. High-Temperature Superconductivity in the $BaPb_{1-x}Bi_xO_3$ Systems. *Solid State Communications* **1975**, *17* (1), 27–28.

(11) S. Yamada, N. Abe, H. Sagayama, K. Ogawa, T. Yamagami, T. Arima. Room-Temperature Low-Field Colossal Magnetoresistance in Double-Perovskite Manganite. *Phys. Rev. Lett.* **2019**, *123* (12), 126602.

(12) Maria Baldini, Takaki Muramatsu, Mohammad Sherafati, Ho-kwang Mao, Lorenzo Malavasi, Paolo Postorino, Sashi Satpathy, Viktor V. Struzhkin. Origin of Colossal Magnetoresistance in $LaMnO_3$ Manganite. *Proceedings of the National Academy of Sciences* **2015**, *112* (35), 10869–10872.

(13) Ji Zhang, Wei-Jing Ji, Jie Xu, Xiao-Yu Geng, Jian Zhou, Zheng-Bin Gu, Shu-Hua Yao, Shan-Tao Zhang. Giant Positive Magnetoresistance in Half-Metallic Double-Perovskite Sr_2CrWO_6 Thin Films. *Science Advances* **2017**.

(14) C. N. R. Rao. Charge, Spin, and Orbital Ordering in the Perovskite Manganates, $Ln_{1-x}A_xMnO_3$ (Ln = Rare Earth, A = Ca or Sr). *J. Phys. Chem. B* **2000**, *104* (25), 5877–5889.

(15) Masaya Uchida, Daisuke Akahoshi, Reiji Kumai, Yasuhide Tomioka, Taka-hisa Arima, Yoshinori Tokura, Yoshio Matsui. Charge/Orbital Ordering Structure in Ordered Perovskite $Sm_{1/2}Ba_{1/2}MnO_3$. *J. Phys. Soc. Jpn.* **2002**, *71* (11), 2605–2608.

(16) Xubin Ye, Jianfa Zhao, Hena Das, Denis Sheptyakov, Junye Yang, Yuki Sakai, Hajime Hojo, Zhehong Liu, Long Zhou, Lipeng Cao, Takumi Nishikubo, Shogo Wakazaki, Cheng Dong, Xiao Wang, Zhiwei Hu, Hong-Ji Lin, Chien-Te Chen, Christoph Sahle, Anna Efiminko, Huibo Cao, Stuart Calder, Ko Mibu, Michel Kenzelmann, Liu Hao Tjeng, Runze Yu, Masaki Azuma, Changqing Jin, Youwen Long. Observation of Novel Charge Ordering and Spin Reorientation in Perovskite Oxide $PbFeO_3$. *Nature Communications* **2021**, *12* (1), 1917.

(17) João Pedro Cardoso, Davide Delmonte, Edmondo Gilioli, Elena L. Fertman, Alexey V. Fedorchenko, Vladimir V. Shvartsman, Vaidotas Paukšta, Robertas Grigalaitis, Jūras Banys, Dmitry D. Khalyavin, Joaquim M. Vieira, Andrei N. Salak. Phase Transitions in the Metastable Perovskite Multiferroics $BiCrO_3$ and $BiCr_{0.9}Sc_{0.1}O_3$: A Comparative Study. *Inorg. Chem.* **2020**, *59* (13), 8727–8735.

(18) Liang-Jun Zhai, Huai-Yu Wang. The Magnetic and Multiferroic Properties in $BiMnO_3$. *Journal of Magnetism and Magnetic Materials* **2017**, *426*, 188–194.

(19) Fuyuhiko Sugawara, Shuichi Iiida, Yasuhiko Syono, Syun-iti Akimoto. Magnetic Properties and Crystal Distortions of $BiMnO_3$ and $BiCrO_3$. *J. Phys. Soc. Jpn.* **1968**, *25* (6), 1553–1558.

(20) De-Chang Jia, Jia-Huan Xu, Hua Ke, Wen Wang, Yu Zhou. Structure and Multiferroic Properties of $BiFeO_3$ Powders. *Journal of the European Ceramic Society* **2009**, *29* (14), 3099–3103.

(21) Diego Carranza-Celis, Alexander Cardona-Rodríguez, Jackeline Narváez, Oscar Moscoso-Londono, Diego Muraca, Marcelo Knobel, Nancy Ornelas-Soto, Andreas Reiber, Juan Gabriel Ramírez. Control of Multiferroic Properties in $BiFeO_3$ Nanoparticles. *Scientific Reports* **2019**, *9* (1), 3182.

(22) Minu Kim, Graham M. McNally, Hun-Ho Kim, Mohamed Oudah, Alexandra S. Gibbs, Pascal Manuel, Robert J. Green, Ronny Sutarto, Tomohiro Takayama, Alexander Yaresko, Ulrich Wedig, Masahiko Isobe, Reinhard K. Kremer, D. A. Bonn, Bernhard Keimer, Hidenori Takagi. Superconductivity in $(Ba,K)SbO_3$. *Nature Materials* **2022**, *21* (6), 627–633.

(23) T. He, Q. Huang, A. P. Ramirez, Y. Wang, K. A. Regan, N. Rogado, M. A. Hayward, M. K. Haas, J. S. Slusky, K. Inumara, H. W. Zandbergen, N. P. Ong, R. J. Cava. Superconductivity in the Non-Oxide Perovskite $MgCNi_3$. *Nature* **2001**, *411* (6833), 54–56.

(24) Fangze Liu, Siraj Sidhik, Mark A. Hoffbauer, Sina Lewis, Amanda J. Neukirch, Vitaly Pavlenko, Hsinhan Tsai, Wanyi Nie, Jacky Even, Sergei Tretiak, Pulickel M. Ajayan, Mercouri G. Kanatzidis, Jared J. Crochet, Nathan A. Moody, Jean-Christophe Blancon, Aditya D. Mohite. Highly Efficient Photoelectric Effect in Halide Perovskites for Regenerative Electron Sources. *Nature Communications* **2021**, *12* (1), 673.

(25) A. S. Cavichini, M. T. Orlando, J. B. Depianti, J. L. Passamai, F. Damay, F. Porcher, E. Granado. Exotic Magnetism and Spin-Orbit-Assisted Mott Insulating State in a 3d/5d Double Perovskite. *Phys. Rev. B* **2018**, *97* (5), 054431.

(26) Tianjun Liu, Xiaoming Zhao, Jianwei Li, Zilu Liu, Fabiola Liscio, Silvia Milita, Bob C. Schroeder, Oliver Fenwick. Enhanced Control of Self-Doping in Halide Perovskites for Improved Thermoelectric Performance. *Nature Communications* **2019**, *10* (1), 5750.

(27) Yasuhiko Syono, Syun-Iti Akimoto, Yasuo Endoh. High Pressure Synthesis of Ilmenite and Perovskite Type $MnVO_3$ and Their Magnetic Properties. *Journal of Physics and Chemistry of Solids* **1971**, *32* (1), 243–249.

(28) Akihisa Aimi, Daisuke Mori, Ko-ichi Hiraki, Toshihiro Takahashi, Yue Jin Shan, Yuichi Shirako, Jianshi Zhou, Yoshiyuki Inaguma. High-Pressure Synthesis of *A* -Site Ordered Double Perovskite $CaMnTi_2O_6$ and Ferroelectricity Driven by Coupling of *A* -Site Ordering and the Second-Order Jahn–Teller Effect. *Chem. Mater.* **2014**, *26* (8), 2601–2608.

(29) Shoubao Zhang, Takashi Saito, Masaichiro Mizumaki, Wei-tin Chen, Takenori Tohyama, Yuichi Shimakawa. Site-Selective Doping Effect in $AMn_3V_4O_{12}$ ($A = Na^+$, Ca^{2+}, and La^{3+}). *J. Am. Chem. Soc.* **2013**, *135* (16), 6056–6060.

(30) A. M. Arévalo-López, G. M. McNally, J. P. Attfield. Large Magnetization and Frustration Switching of Magnetoresistance in the Double-Perovskite Ferrimagnet Mn_2FeReO_6. *Angewandte Chemie International Edition* **2015**, *54* (41), 12074–12077.

(31) M. Li, J. P. Hodges, M. Retuerto, Z. Deng, P. W. Stephens, M. C. Croft, X. Deng, G. Kotliar, J. Sánchez-Benítez, D. Walker, M. Greenblatt. Mn_2MnReO_6: Synthesis and Magnetic Structure Determination of a New Transition-Metal-Only Double Perovskite Canted Antiferromagnet. *Chem. Mater.* **2016**, *28* (9), 3148–3158.

(32) E. Solana.M., K N. A., M. Herz, P. Manuel, J. Paul Attfield. Unconventional Magnetism in the High Pressure 'All Transition Metal' Double Perovskite Mn_2NiReO_6. *Chemical Communications* **2020**, *56* (83), 12574–12577.

(33) Man-Rong Li, Peter W. Stephens, Mark Croft, Zheng Deng, Wenmin Li, Changqing Jin, Maria Retuerto, Jason P. Hodges, Corey E. Frank, MeiXia Wu, David Walker, Martha Greenblatt. $Mn_2(Fe_{0.8}Mo_{0.2})MoO_6$: A Double Perovskite with Multiple Transition Metal Sublattice Magnetic Effects. *Chem. Mater.* **2018**, *30* (14), 4508–4514.

(34) M. Tanaka, Y. Katsuya, A. Yamamoto. A New Large Radius Imaging Plate Camera for High-Resolution and High-Throughput Synchrotron X-Ray Powder Diffraction by Multiexposure Method. *Review of Scientific Instruments* **2008**, *79* (7), 075106.

(35) M. Tanaka, Y. Katsuya, Y. Matsushita, O. Sakata. Development of a Synchrotron Powder Diffractometer with a One-Dimensional X-Ray Detector for Analysis of Advanced Materials. *Journal of the Ceramic Society of Japan* **2013**, *121* (1411), 287–290.

(36) F. Izumi, K. Momma. Three-Dimensional Visualization in Powder Diffraction. *Solid State Phenomena* **2007**, *130*, 15–20.

(37) K. Momma, F. Izumi. VESTA: A Three-Dimensional Visualization System for Electronic and Structural Analysis. *J Appl Cryst* **2008**, *41* (3), 653–658.

(38) N. E. Brese, M. O'Keeffe. Bond-Valence Parameters for Solids. *Acta Cryst B* **1991**, *47* (2), 192–197.

(39) Alexei A. Belik, Ran Liu, Kazunari Yamaura. Dielectric and Spin-Glass Magnetic Properties of the A-Site Columnar-Ordered Quadruple Perovskite $Sm_2CuMn(MnTi_3)O_{12}$. *Materials* **2022**, *15* (23), 8306.

(40) A. L. Efros, B. I. Shklovskii. Coulomb Gap and Low Temperature Conductivity of Disordered Systems. *J. Phys. C: Solid State Phys.* **1975**, *8* (4), L49.

Chapter 6 General Conclusions and Future Prospects

6.1. General conclusions

Over the past few decades, 5*d* transition metal oxides have attracted a great deal of interest due to their diverse properties. The exploration of new materials involving 5*d* transition metal elements is expected to be very helpful in establishing and enhancing new novel properties of materials. Therefore, this thesis is working on new 5*d* metal oxides with the hope of discovering and understanding new interesting physical phenomena. Included in this thesis are six perovskite-related 5*d* metal oxides, which were all synthesized under high-pressure and high-temperature (HPHT) conditions. I have combined a variety of experimental devices to systematically characterize their crystal structures as well as physical properties. The main results are summarized below.

Two new double perovskites, Cd_2FeOsO_6 and Cd_2FeReO_6 were synthesized under high-temperature and high-pressure conditions, using Cd as an uncommon A-site occupant. Synchrotron XRD refinements indicated that both of them fall into the $P2_1/n$ space group and are partially ordered at the B site. Electrical measurements evidenced that both of them are semiconductors and follow the Mott's VRH model. Magnetic measurements demonstrated that Cd_2FeOsO_6 presented a ferrimagnetic phase transition at 283 K and large coercivity fields as well as giant exchange bias effect with remarkable small cooling field were discovered as well. Another compound Cd_2FeReO_6 displays a ferrimagnetic ordered with $T_c \sim 460K$ and a large tunneling magnetoresistance of ~37% was observed at 5K and 90 kOe. In addition, the first-principles calculation suggested its half-metallic properties. Taken together, the work presented here suggest that the occupation of the A-site with Cd in double perovskites is a new promising route for exploring new materials with potential applications.

The $KSbO_3$-type family has been almost ignored by researchers due to their huge structural frustration and the lack of excellent performance findings. This study revealed $KSbO_3$-type 5*d* oxides, which exhibit only weak temperature-dependent paramagnetism to date, are a group of compounds that can be converted into spintronic materials by doping with 3d elements, leading to the development of new $KSbO_3$-type materials with both theoretical and practical significance. Specifically, I succeeded in synthesizing doped $Bi_3Re_3O_{11}$ and $Bi_3Os_3O_{11}$ with Fe up to 29 atomic% using high-temperature and high-pressure conditions. Their crystal structures were confirmed to belong the space group *Pn*-3 through the

Synchrotron XRD analysis. From the basic physical property measurements, the spin glassy like behavior below 22K and negative magnetoresistance ~10% were observed in rhenium oxide, and ferrimagnetism was confirmed in osmium oxide. In particular, a striking characteristic was noticed: at 490 K, the highest temperature yet reported for $KSbO_3$-type materials, $Bi_3Os_{2.45}Fe_{0.55}O_{11}$ demonstrates magnetic characteristics.

Usually, transition-metal cations occupy *B*-sites but it was found that filling of the *A*-sites with relatively large transition metal cations is possible under high-pressure conditions. In my work, two new *A*-site manganite perovskites $MnV_{0.5}Nb_{0.5}O_3$ and $MnV_{0.5}Ta_{0.5}O_3$ were obtained under high-pressure and high-temperature conditions. The synchrotron XRD study revealed that both of them belong to the $GdFeO_3$-type structure with the space group *Pnma.* Magnetic property measurements indicated both of them behavior as ferrimagnets with a phase transition point at 17 and 18 K for $MnV_{0.5}Nb_{0.5}O_3$ and $MnV_{0.5}Ta_{0.5}O_3$, respectively. Electrical transport measurements suggested both compounds are semiconductors, following the Efros-Shklovskii variable-range hopping conduction model with activation energies of 0.13 eV for $MnV_{0.5}Nb_{0.5}O_3$ and 0.31 eV for $MnV_{0.5}Ta_{0.5}O_3$.

6.2. Future prospects

My current work also offers many aspects that can be developed, as described in detail below:

(i) In Cd_2FeOsO_6, I found that a very small cooling field can trigger a large EB effect, making it of great value for potential theoretical research and practical application. **Figure 6.1** illustrated the performance comparison with other representative materials Y_2NiIrO_6 [4], Mn-Pt-Ga Heusler alloys [5], $Mn_{3.5}Co_{0.5}N$ [6] and a series of Mn_3Ir/FM films [7]. The main difficulty it needs to overcome at present is mainly to increase the usable temperature range to room temperature. In the future, the synthesis conditions could be changed to adjust the antisite degree in the compound, or doping with other elements could be attempted to improve the performance of the material.

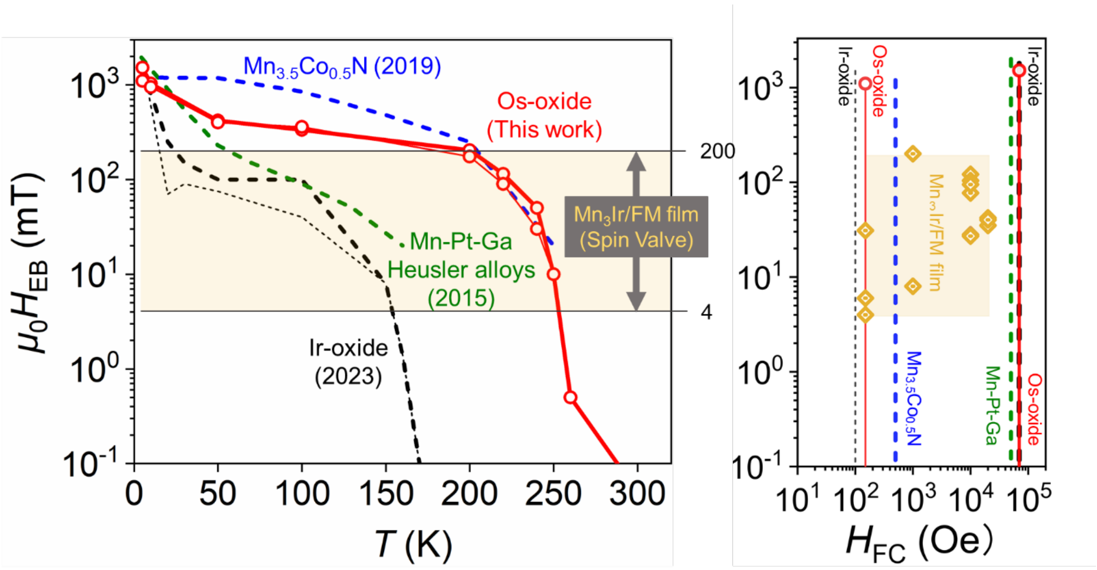

Figure 6.1. EB effect performance comparison between Cd_2FeOsO_6 and other representative materials.

(ii) The doping of $Bi_3Re_3O_{11}$ and $Bi_3Os_3O_{11}$ with iron greatly improves the performance of $KSbO_3$-type compounds. More profoundly, there are adequate $KSbO_3$-type materials available as host compounds, in addition to $Bi_3M_3O_{11}$ (M: metal atom) compounds, which are usually cubic with the space group of Pn-3, the $KSbO_3$ family also contains compounds belonging to other space groups such as $La_4Ru_6O_{19}$ [1] in the I23 lattice, $KBiO_3$ [2] and $Sr_2Re_3O_9$ [3] in the Im-3 lattice. Also, abundance of 3d elements can be selected as doping candidates, and the doping ratio can be adjusted and controlled by the thermal treatments. Therefore, there are lots of research work can be developed based on this idea, and I am currently continuing to follow up on the doping of $Bi_3Ru_3O_{11}$ with Fe. **Figure 6.2** shows the SXRD results of the doped $Bi_3Fe_{0.67}Ru_{2.33}O_{11}$, next I will investigate its physical properties.

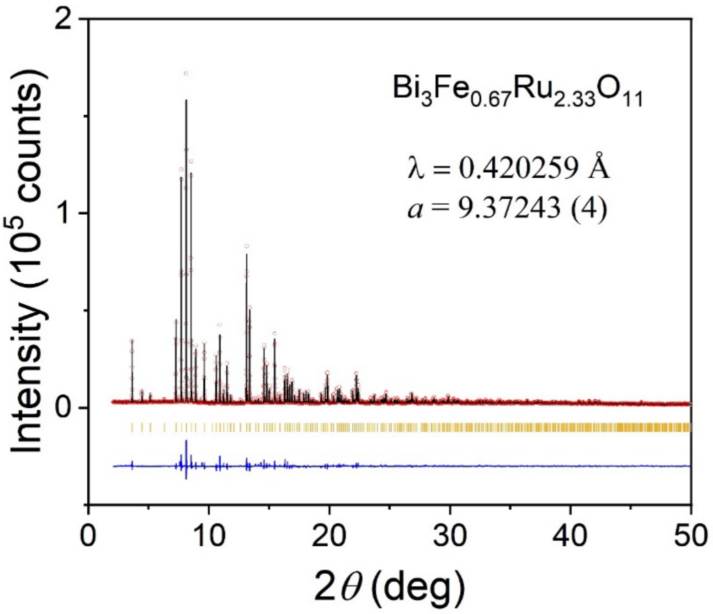

Figure 6.2. Synchrotron XRD refinement results of $Bi_3Fe_{0.67}Ru_{2.33}O_{11}$.

(iii) Under high pressure conditions, transition metal atoms can be used for A-site occupation to form unusual A-site magnetic manganite in which wide variety of outstanding physical properties can be sought among them. Based on this idea, there are still lots of B-site 3*d*/4*d*(5*d*) combinations have potential possibilities to obtain excellent exotic physical properties.

With these considerations in mind, there are still many research studies can be done and works on the synthesis of new compounds to explore materials with potentially excellent properties could be done.

References in Chapter 6

(1) P. Khalifah, K. D. Nelson, R. Jin, Z. Q. Mao, Y. Liu, Q. Huang, X. P. A. Gao, A. P. Ramirez, R. J. Cava. Non-Fermi-Liquid Behaviour in $La_4Ru_6O_{19}$. *Nature* **2001**, *411* (6838), 669–671.

(2) T. N. Nguyen, D.M. Giaquinta, W. M. Davis, H. C. zur Loye. Electrosynthesis of $KBiO_3$ (Potassium Bismuth Oxide): A Potassium Ion Conductor with the $KSbO_3$ (Potassium Antimony Oxide) Tunnel Structure. *Chem. Mater.* **1993**, *5* (9), 1273–1276.

(3) H. Suzuki, H. Ozawa, H. Sato. Anomalous Electric Conductions in $KSbO_3$-Type Metallic Rhenium Oxides. *Journal of the Physical Society of Japan* **2007**, *76* (4), 044805–044805.

(4) Zheng Deng, Xiao Wang, Mengqin Wang, Feiran Shen, Jine Zhang, Yuansha Chen, Hai L. Feng, Jiawang Xu, Yi Peng, Wenmin Li, Jianfa Zhao, Xiancheng Wang, Manuel Valvidares, Sonia Francoual, Olaf Leupold, Zhiwei Hu, Liu Hao Tjeng, Man-Rong Li, Mark Croft, Ying Zhang, Enke Liu, Lunhua He, Fengxia Hu, Jirong Sun, Martha Greenblatt, Changqing Jin. Giant Exchange-Bias-Like Effect at Low Cooling Fields Induced by Pinned Magnetic Domains in Y_2NiIrO_6 Double Perovskite. *Advanced Materials* **2023**, *35* (17), 2209759.

(5) Ajaya K. Nayak, Michael Nicklas, Stanislav Chadov, Panchanana Khuntia, Chandra Shekhar, Adel Kalache, Michael Baenitz, Yurii Skourski, Veerendra K. Guduru, Alessandro Puri, Uli Zeitler, J. M. D. Coey, Claudia Felser. Design of Compensated Ferrimagnetic Heusler Alloys for Giant Tunable Exchange Bias. *Nature Mater* **2015**, *14* (7), 679–684.

(6) Lei Ding, Lihua Chu, Pascal Manuel, Fabio Orlandi, Meicheng Li, Yanjiao Guo, Zhuohai Liu. Giant Spontaneous Exchange Bias in an Antiperovskite Structure Driven by a Canted Triangular Magnetic Structure. *Mater. Horiz.* **2019**, *6* (2), 318–325.

(7) James M. Taylor, Edouard Lesne, Anastasios Markou, Fasil Kidane Dejene, Benedikt Ernst, Adel Kalache, Kumari Gaurav Rana, Neeraj Kumar, Peter Werner, Claudia Felser, Stuart S. P. Parkin. Epitaxial Growth, Structural Characterization, and Exchange Bias of Noncollinear Antiferromagnetic Mn_3Ir Thin Films. *Phys. Rev. Mater.* **2019**, *3* (7), 074409.

List of appended publications

This thesis is based on the following publications.

1. Scientific papers

1. **<u>Xun Kang</u>**, Ryuta Ishikawa, Alexei A. Belik, Yoshihiro Tsujimoto, Satoshi Kawata, Kazunari Yamaura. Achieving Large Exchange Bias Effect in Cd_2FeOsO_6 with Small Cooling Fields. *Chem. Mater.* **2023**. 35, 20, 8621-8628.

2. **<u>Xun Kang</u>**, Alexei A. Belik, Yoshihiro Tsujimoto, Kazunari Yamaura. High-Pressure Synthesis and Magnetic and Electrical Properties of Fe-Doped $Bi_3Re_3O_{11}$ and $Bi_3Os_3O_{11}$**.** *Inorg. Chem.* **2022**. 61, 51, 21148-21156.

3. **<u>Xun Kang</u>**, Ryuta Ishikawa, Alexei A. Belik, Yoshihiro Tsujimoto, Satoshi Kawata, Kazunari Yamaura. Cd_2FeReO_6: a high-TC double perovskite oxide with remarkable tunneling magnetoresistance. *Inorg. Chem.* **2023**. 62, 45, 18474-18484.

4. **<u>Xun Kang</u>**, Alexei A. Belik, Yoshihiro Tsujimoto, Kazunari Yamaura. High-pressure synthesis of half-doped perovskites $MnV_{0.5}Nb_{0.5}O_3$ and $MnV_{0.5}Ta_{0.5}O_3$ with unusual A-site small Mn atoms. Submitted to *High Press Res.* (Published online: 21 Nov **2023**).

2. Presentation

1. **<u>Xun Kang</u>** and Kazunari Yamaura, “High-Pressure Synthesis and Ferrimagnetism of Perovskites $MnV_{0.5}M_{0.5}O_3$ (M=Nb,Ta)”; The 5th International Union of Materials Research Societies International Conference of Young Researchers on Advanced Materials (IUMRS-ICYRAM 2022), Aug, 3-6, 2022, Fukuoka, Japan.

2. **<u>Xun Kang</u>** and Kazunari Yamaura, “High-Pressure Synthesis and Ferrimagnetism of Perovskites $MnV_{0.5}M_{0.5}O_3$ (M=Nb,Ta)”; The 32nd Annual Meeting of MRS-J, Dec, 5-7, 2022, Yokohama, Japan.

3. **<u>Xun Kang</u>** and Kazunari Yamaura., Dec., 7-10, 2021; High-Pressure Synthesis and Ferrimagnetism of Perovskites $MnV_{0.5}M_{0.5}O_3$ (M=Nb,Ta); 1p-45; The International Conference on Mixed-Anion Compounds.

Acknowledgement

On this occasion of my graduation, I would like to express my gratitude to many people who have helped me to complete my PhD during the past three years. First of all, I gratefully appreciate my supervisor Prof. Kazunari Yamaura from the bottom of my heart for giving me such a precious opportunity to study and live in Japan. Apart from his patient and gentle guidance in assisting me in solving research problems, writing scientific papers and being an independent thinker, his rigorous attitude towards science, diligent study spirit as well as optimism in facing difficulties have all had a significant positive impact on my future journey and have made my time studying in Japan the most valuable memory and treasure of my life.

Besides, I would particularly like to thank Prof. Alexei A. Belik. for his patient guidance and corrections in the refinements of crystal structures and instructions in the use of various instruments and equipment. I sincerely thank Prof. Yoshihiro Tsujimoto for your great help in completing the measurement of the Mössbauer spectrum and valuable comments on the revision of my scientific papers. Also, I want to thank Prof. Yoshitaka Matsushita for your advice and help in the DSC measurements. I would like to give my gratitude to Dr. Yuichi Shirako, Dr. Ran Liu, Dr. Hong Yan and Dr. Hiroaki Hayashi, because they taught me how to use lab-facilities and handle data. Thanks Dr. Jie Chen give me her helpful discussions and suggestions. I would like to thanks Mr. Yu Meng, Mr. Shaoxuan Li, Mr. Xuan Liang for their daily supports and help. Last but not the least, I thank my friends and families for their endless moral support. It is your accompaniment that gives me the motivation to overcome difficulties.

I would like to express my gratitude to all of you again, I am who I am today because of you.